Geology, mineralogy, geochronology, and genesis of the Vangtat gold belt, southeastern Laos

Patthana Bounliyong

6518104

Graduate School of International Resource Sciences

Akita University

ACKNOWLEDGMENT

First of all, I would like to express a big thank my academic supervisors, Professor Yasushi Watanabe, and Professor Antonio Arribas for always supporting, and advising me during my Ph.D. research at Akita University, they always brought me constructive suggestions, excellent comments, and helpful discussions through this project, which is very helpful to success this doctoral dissertation. Associate Professor Takuya Echigo was also thanked for his kindly assist in the laboratory works supporting this Ph.D. research. Professor Testumaru Itaya was also thanked for his critical discussion on this thesis Chapter and technical assistance during the K-Ar analysis at Okayama Univerisity of Science, Japan.

Numerous people are also thanked for their technical assistance during the experiments, including Dr. Koshi Yaki (Okayama Univerisity of Science; K-Ar radiometric dating), Associate Professor Ryohei Takahashi, Dr. Hinako Sato, Dr. Pearlyn Manalo (Akita University; sulfur isotope analysis). My colleagues, the members of "Mineral Resource and Tectonic Lab" were also thankful.

I would like to express my gratitude to Vangtat Mining Company for allowing me to conduct the fieldwork on their exploration areas and also provide valuable drill core samples for this research. Many thanks to Mr. Henry Wong and his staff for their valuable time to discuss and share the result of exploration in the Vangtat gold deposit.

The author was awarded the scholarship by the Japan International Cooperation Agency (JICA) within the Shiken-no KIZUNA program, and I am deeply grateful to Dr. Yoshitaka Hosoi for handling this fellowship.

ABSTRACT

The Indochina Terrane is a major tectonic unit of mainland Southeast Asia, is bound to the north by the South China Terrane and to the west by the Sibumasu Terrane, with the Truong Son fold belt, and the Loei and Sukhothai fold belts marking broad collision zones with the two continental terranes. Broadly coincident with these tectonic collisions, several internal domains were amalgamated to the Indochina Terrane during the Indosinian orogeny. Magmatism, metamorphism, deformation, and hydrothermal alteration along the domain boundaries surrounding and within the Indochina Terrane resulted in the formation of a variety of precious- and base-metal deposits, notably porphyry-related skarn, epithermal, sediment-hosted, and orogenic gold deposits. The collision orogenesis between the eastern extension of Indochina Terrane with the Kontum Massif resulted in the formation of the Poko suture zone and associated structures, including the Vangtat shear zone, which the subject of this research as the host of a recently discovered orogenic gold belt.

A newly discovered orogenic gold belt consists of the Thongkai-Ok, Vangtat, and Gieng Dat deposits, occurs within the Vangtat shear zone and is called as the Vangtat orogenic gold belt. This research aims to (1) clarify the nature and genesis of primary gold mineralization in the Vangtat gold belt, and (2) constrain the age of gold mineralization and to better understand the relationship between Southeast Asia tectonics and mineralization. Base on the study of host geology, geochronology, ore and gangue mineralogy, hydrothermal alteration, fluid inclusion, and sulfur isotope.

The Vangtat gold belt is hosted in the early- to mid-Palaeozoic regional metamorphic belt, located in the western part of the Poko suture zone, western margin of the Kontum Massif. The Vangtat gold deposit is one of several actively mined deposits and represented the main economic orebody of the Vangtat gold belt. Two main rock units are found in the deposit scale: the lower unit is made up of metagabbro and the upper unit is composed of metasedimentary lithologies, including pelitic schist, slate, metasandstone and quartzite. The lithological units around the Vangtat deposit, as well as other hard-rock (primary) gold deposits in the district, are covered by a thick (~ up to 50 m) blanket of weathering and supergene oxidation, which led to local gold remobilization and concentration of secondary gold in surficial detrital sediments. This alluvial gold is recovered by artisanal miners through the district and marks the first recorded gold mining in the region.

Pelitic schist is the main mineralized host rock of the Vangtat deposit, which is made up of foliated muscovite-chlorite with finely interlayer quartz and plagioclase. Pelitic also contained a minor amount (<1 vol%) of carbonaceous or graphitic materials, which frequently interleaved in the foliated chlorite-muscovite. Within progressive metamorphism, the layers of graphite were segregated and associated with foliation planes of pelitic schist, and became deformed, including folding and development of microshears, indicates that graphite transformation during the regional metamorphism. Raman spectrometry and its parameters were estimated the temperature of graphite transformation and provided a temperature range of 350-410 ^{o}C. This temperature range is consistent with the major components of the pelitic schist, suggesting that graphite within the pelitic schist was metamorphosed or transformed under the greenschist facies metamorphic grade.

The development of shear structures within the Vangtat shear zone intersected pelitic schist marked the favorable site for gold deposition in the Vangtat gold belt, in which the development of shear structure would create an open space and permeability for hydrothermal fluid transports ore mineral constituents upon entering an ore trap. Vein marked the center of the hydrothermal activity and represented the fluid pathway, hydrothermal alteration and fluid-rock interaction likely occurred perpendicular to the veins (fluid conduits). Innermost alteration is marked by the graphite-carbonate alteration envelope and laterally extended to the adjacent wall rocks. Moreover. the hydrothermal evolution transected two different types of wall rock lithologies within the contrasting components (e.g. metagabbro in the lower portion and pelitic schist in the upper portion) displayed a variety of alteration assemblages.

High-grade gold mineralization (> 3g/t Au on average; reaching values >100 g/t Au in selected hand specimens and drill core intercepts) occurs only in the quartz-sulfide-graphite-carbonate-white mica-chlorite veins. Lower-grade gold mineralization (avg. < 3g/t Au) occurs in a graphite-carbonate-quartz-sulfide hydrothermal alteration zone that forms an envelope around the veins and grades into a sub-economic to barren altered pelitic schist. Gold is closely associated with sulfide, identically gold concentration decreases together with sulfide content from the quartz-sulfide vein at the center towards the marginally altered host rocks.

Pyrite is the main host for gold mineralization in the Vangtat deposit. Most of the auriferous pyrite is homogeneous in texture (i.e. rare of zoning texture is observed), coarse-grained up to ~1 cm, consistent in composition, and less of other elements in solid solution. Other sulfides, such as chalcopyrite, arsenopyrite, sphalerite, galena, bismuthinite, and pyrrhotite occur as minor and trace amounts incorporated with pyrite,

most likely occur as inclusion in pyrite. These typical characteristics of auriferous pyrite possibly suggest that pyrite has formed during the hydrothermal processes, which allows the crystallization of pyrite slowly growth and most of the trace elements are partitioned into the separated phases rather than incorporated in solid solution in pyrite.

The co-existing and textural relationship of pyrite and arsenopyrite in the mineralized vein suggest an equilibrium condition among them, which applies to estimate the trapping temperature of ore formation in the Vangtat deposit. The range of As content in arsenopyrite plotted in the pyrite-arsenopyrite phase of the Fe-As-S system diagram estimated the temperature range of 335 to 385 ºC.

Gold mainly occurs as particle grains inclusions in sulfide, predominantly pyrite, appearing to have been incorporated during the crystallization of sulfides. Free-gold is rarely observed in the mineralization zone. Gold to silver ratio ranges from 5:1 to 25:1, with an average of 10:1.

Fluid inclusions trapped in quartz crystals from mineralized veins represented the nature of hydrothermal fluid responsible for gold mineralization in the Vangtat deposit, Vangtat gold belt, indicating that ore-forming fluid has the homogenization temperature range of 190 to 325 ºC (240 to 250 ºC is observed for the majority of fluid inclusions) and salinity range of 0.7 to 10.0 wt% NaCl equivalent (4 to 6 wt% NaCl equivalent is observed for the majority of fluid inclusions). The gas compositions are CO_2, CH_4, N_2, and H_2S. The composition of the ore-forming fluid is considered to have been generated via metamorphic dehydration and devolatilization. The presence of these gas compositions in the ore-forming fluid may indicate the reaction of fluid-wall rocks played an important role in gold precipitation.

Depth of ore formation is translated using the pressure range of the ore formation, which was estimated by the correlation temperature between (1) homogenization temperature (240 to 250 °C) deduced for microthermometric data, and (2) trapping temperature (336-384 °C) obtained from arsenopyrite geothermometry. Providing the pressure range of 330 to 400 Mpa and translated to the depth range of 10 to 12 km (based on a typical lithostatic pressure gradient of 100 MPa=3 km).

Gold is carried as the sulfide complex along with the ore fluid. The precipitation of gold is related to both (1) The destabilization of sulfide complex by sulfidation reaction, which involves the interaction of Fe-bearing mineral (e.g. chlorite) in the host rock and S-bearing fluid, and (2) Changing the physical-chemical of the ore-forming fluid, which relates to the reductive reaction with the carbonaceous material or graphite dominant in the host rock and alteration envelope that facilitated gold extraction.

The sulfur isotope composition of auriferous pyrite at the Vangtat deposit ranges from +1.3 and +10.7 ‰, a narrow range is confined from +4 to +6 ‰ for the most population data and corresponding to the high-grade gold assay. These sulfur isotope compositions are not related to the sedimentary sulfur through the geological time, together with a narrow range of sulfur isotope composition may indicate the single source of sulfur. Hence, the input of sulfur sourced from the metasedimentary host rocks can not explain in the sulfur isotope data. However, these sulfur isotope compositions are compatible with the sulfur isotope composition range of the most igneous rocks, and it could potentially be the source of sulfur and ore components.

The presence of hydrothermal white mica-bearing auriferous vein from the Thongkai-Ok deposit was subjected for K-Ar dating in order to constrain the age of gold mineralization in the Vangtat gold belt. The results provided a wide range of ages

from 348 to 206 Ma. Within the interpretation of excess argon derived from contaminated quartz as an impurity of samples defined the youngest age (206 Ma) of a quartz-free fraction was the closest age of gold mineralization in the Vangtat gold belt. A 206 Ma age of gold mineralization in the Vangtat gold belt, southeast Laos is consistent with regional geological and geochronological data and indicates a post-collisional, post-peak metamorphism hydrothermal gold event that is potentially younger than much of the orogenic gold mineralization in nearby Vietnam.

In conclusion, the nature and genesis of gold mineralization in the newly discovered Vangtat gold belt have many similarities to the orogenic gold deposits globally.

CONTENTS

APPENDIX

Appendix I: Microthermometric data

Appendix II: Measurement condition for fluid inclusion study

Appendix III: Conventional technique for sulfur isotope analysis

FIGURES

Chapter 1 Page

Chapter 2

Chapter 3

Chapter 4

Chapter 5

TABLES

CHAPTER 1 INTRODUCTION

1.1. INTRODUCTION

This doctoral dissertation documents the primary gold mineralization characteristics of the Vangtat gold belt, a newly discovered gold district in southeastern Laos. The research was funded by the Japan International Cooperation Agency (JICA) under the Human Resources Development in the Mining Sector (KIZUNA) program and was also supported by the Vangtat Mining Company during field investigations and data collection, including allowing the author access to drill core samples. This research was conducted at Akita University from 2017 to 2021 and supervised by Professor Yasushi Watanabe, Professor Antonito Arribas, and Associate Professor Takuya Echigo.

1.2. GEOGRAPHY AND ACCESS

The Vangtat gold belt is located in the remote highland area (~1000 m above sea level) of southeastern Laos, close to the border with central Vietnam (Figure 1.1), situated in the town of Vangtat, Sanxay district, Attapeu province; approximately ~10 km west of the border with Vietnam and 100 km east of Attapeu, the capital of Attapeu province (Figure 1.2). The area is characterized by highly undulating topography or mountain ranges and is mainly dominated by primary rain forest and some patches of secondary forest along the ridges.

Figure 1.1. Location of the Vangtat area within the mainland SE Asia

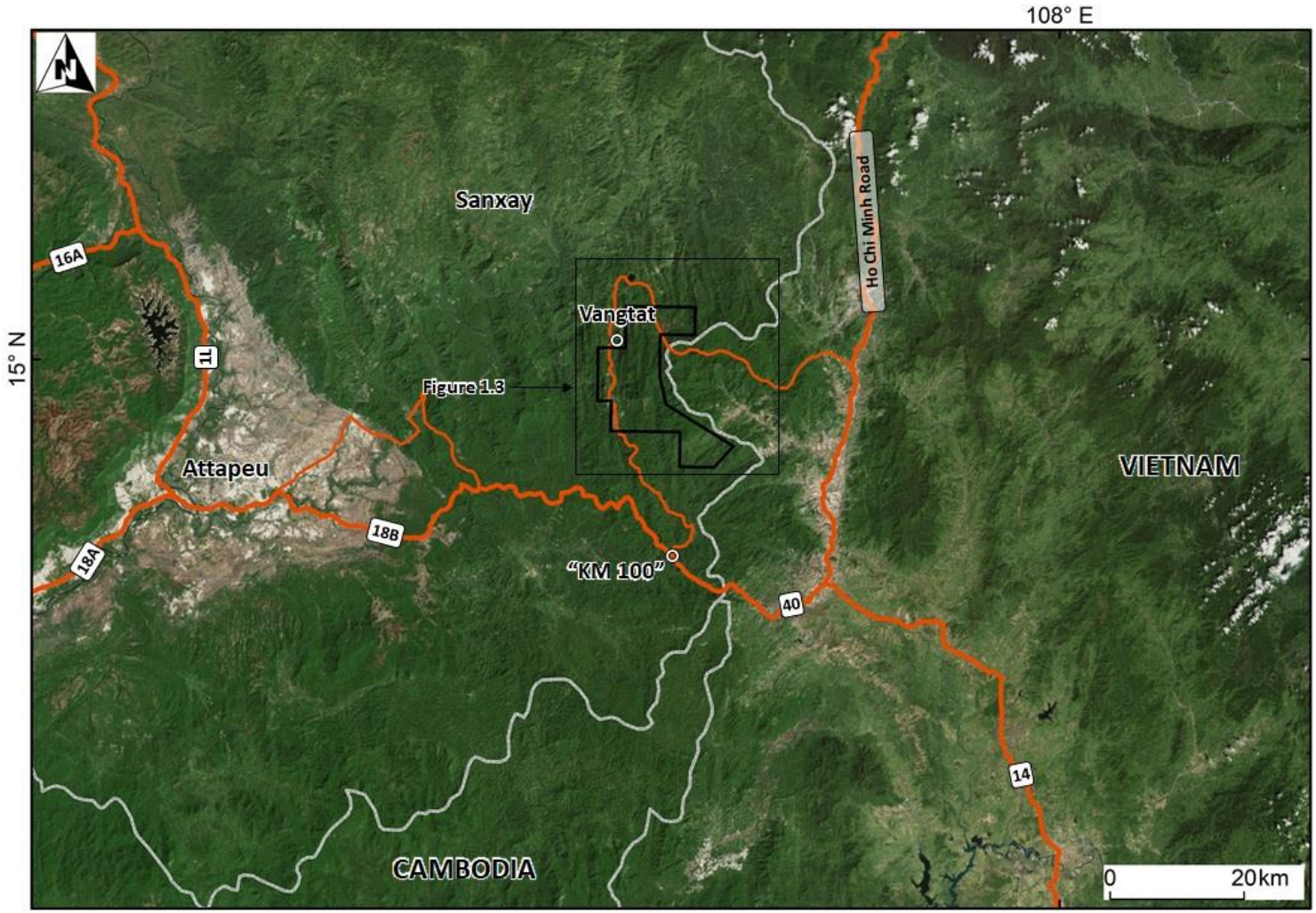

Figure 1.2. Location of the Vangtat area in southeastern Laos. (Google Earthe Image)

Access to Vangtat town can be made by car from the provincial capital of Attapeu, requiring a 3-hour drive east along sealed road number 18B, then turning north at “kilometer 100” and following a 2.5-hour drive north to Vangtat town on a gravel road (Figure 1.2). Driving would be difficult during the rainy season from June to October, when roads are subject to muddy and slippery conditions.

The deposit area and mining camp are situated in the central part of the Vangtat town. The town currently has a population of about 800; local people are mainly engaged in agriculture, typically working on rice farming at limited flat fields occupying the valleys. Slash and burn agriculture methods are commonly used in the district and mostly support rice. In addition, the local inhabitants are familiar with seeking and/or panning gold nuggets along streams and creeks.

The long border between eastern Laos and Vietnam is part of the Ho Chi Minh Trail and was used as a major supply route between North and South Vietnam during the Vietnam War from 1964 to 1975. Consequently, during this period heavy aerial bombardments by US forces primarily targeted the flow of North Vietnamese forces and equipment into southern Vietnam, scarring the landscape along this supply route. Unexploded ordinance from this campaign still contaminates areas within the Vangtat gold district.

1.3. EXPLORATION AND MINING HISTORY

The presence of alluvial gold in the Vangtat region was known by local inhabitants for over a century. Recent artisanal mining in the area commenced in the early 2000s with miners engaged in alluvial and hard rock gold mining, most commonly focused in the

vicinity of the Vangtat deposit (Figure 1.3). The use of heavy equipment and chemical processing (e.g. mercury, cyanide) to extract gold brought the area to the attention of the Laos Ministry of National Defense.

Initial regional geological mapping and mineral exploration in southeastern Laos within the Vangtat district was conducted between 2006 and 2008 by geologists from Geological Survey of Japan (GSJ) and the Department of Geology, Laos (DGEO), under an international cooperation project between JICA (Japan), and DGEO (Laos). A regional 1:200,000 scale geological map of B. Dakyoy (D-48-XII) was produced at that time and alluvial resources of up to a few grams per ton of gold in stream sediment samples as well as several occurrences of gold bearing quartz-sulfide veins, were recognized (Vilayhack *et al*., 2008; Figure 1.3). Soon after, the Vangtat area was recognized as having a high potential for gold mineralization at a regional scale. Intensive alluvial and hard rock gold exploration in the Vangtat area was started in 2007 by the Viet-Laos Mining Company in cooperation with the Laos Ministry of National Defense. The cooperation project granted an exploration license of an area of 219 km^2 (Figure 1.3) and resulted in detailed geological, geochemical, geophysics, and drilling programs. The exploration project at that time focused on surficial supergene gold mineralization.

In 2012, the project owner received a license for the mining operation and gold production in the higher-grade orebodies within an area of 3 km^2 (Figure 1.3). During this time (the early 2010s) several additional small-scale mining centers sprung up in the region, including the Thongkai-Ok and Xekong prospects north of the Vangtat deposit (Figure 1.3).

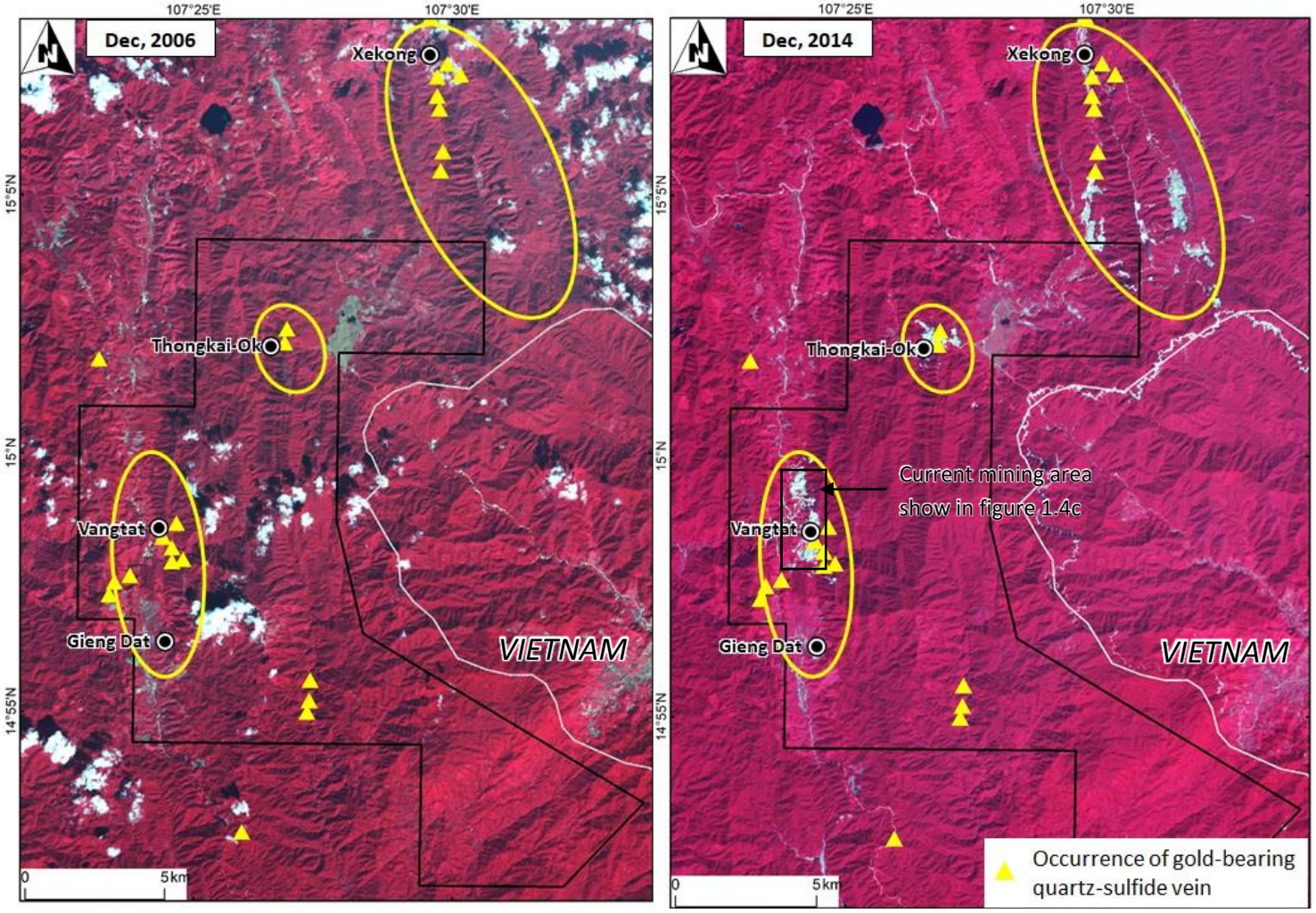

Figure 1.3. ASTER (R3: G2: B1) color composite images differentiated the excavated surface area, with respect to the alluvial gold mining activities by December 2006 (left) and December 2014 (right).

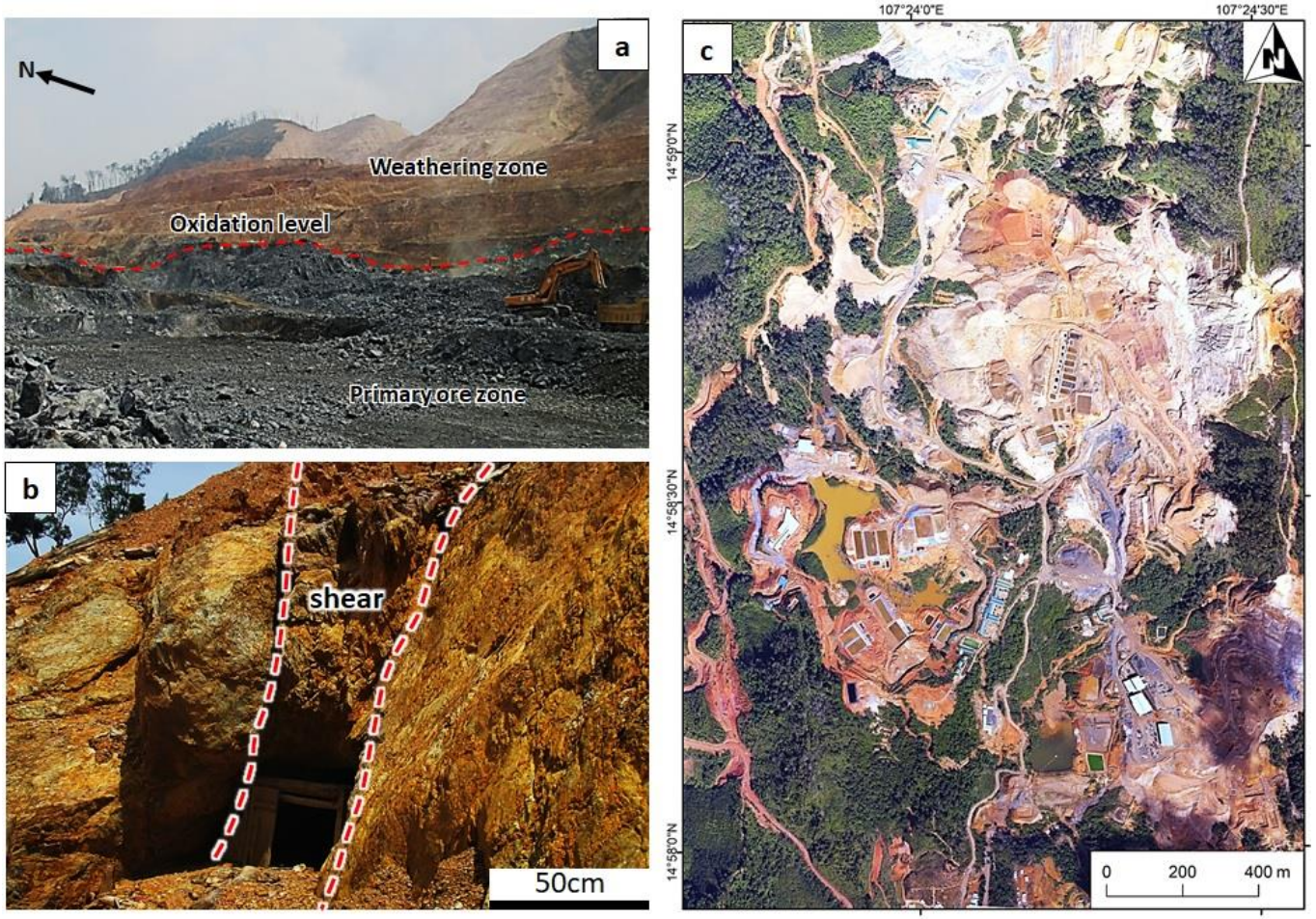

Figure 1.4. a) Ground view of the current Vangtat mine showing initial mining was focused on the weathering (oxidation) zone. Primary sulfide ore lies immediately below the oxidation level; b) Short underground drives typical of the initial mining; c). Aerial view of the current Vangtat mine in 2018.

The comparison of two ASTER images of the Vangtat district between December 2006 and December 2014 (Figure 1.3) recognized that by December 2014 a large surface area had been excavated compared to the earlier alluvial gold mining activities. By the time it was clear the Vangtat area represents a new gold belt in this region with clear regional geological and structural controls.

Initial hard rock mining within the Vangtat deposit occurred as shallow pits and short underground drives within the near-surface oxidation zone, typically down to less than 50 m (Figure 1.4a,b). The operation was focused on the extraction of oxidized ore for crushing and gold extraction in nearby processing plants. The main type of ore contained coarse-grained gold produced from microparticulate gold encapsulated in sulfide minerals during weathering of primary ore and supergene oxidation reactions. This relatively coarse free gold was extracted from the crushed ore, partly via gravity settling and partly via mercury amalgamation as well as heap leaching. No data are available for ore-grade, reserve tonnage, or gold production from the supergene gold.

In 2016, open-pit mining activities were extended down to the top of the unoxidized zone. Mining ceased temporarily when the base of the supergene enrichment zone was reached because there was little or no coarse-grained gold and nearly all the gold was encapsulated in sulfide minerals (i.e. pyrite) in the unoxidized zone. Indications were observed of primary gold bearing veins in which gold was incorporated in pyrite. Following exploration and drilling activities for primary gold mineralization, soon a series of auriferous sulfide-bearing quartz veins and vein zones were discovered. In addition, other prospects (e.g. Gieng Dat) located south of the Vangtat deposit were discovered (Figure 1.3) and the extension of the primary ore zone into the northern and western of the Vangtat deposit was indicated. At this time, the Vangtat mining

company (current name of Viet-Laos Company) is building a gold processing plant for recovering sulfide ore via flotation followed by the roasting of the sulfide concentrate.

1.4. PREVIOUS STUDIES

The Vangtat region of southeastern Laos falls within the western margin of the Kontum Massif (Lepvrier *et al*., 2004; Osanai *et al.*, 2008). To understand the background geology of the Vangtat district in this remote region of Laos only a few published geological articles exist, including the information provided by the regional mapping project conducted by the Geological Survey of Japan and the Department of Geology, Laos (Vilayhack *et al.*, 2008).

These published articles/maps mainly focused on the regional volcanic-plutonic rock units and the tectonic setting at a regional scale. Sanematsu *et al.* (2009; 2011) studied the enrichment of rare earth elements, geochemistry, and Ar-Ar geochronology of granitoids in southeastern Laos, concluding that various intrusions and orogenic events occurred in the western margin of Kontum Massif. Recently Gardner *et al*. (2017); Wang *et al*. (2020) have also dated volcanic-plutonic rocks in southeastern Laos, using zircon U-Pb dating, and analyzed whole-rock chemistry of these volcanic-plutonic rocks.

1.5. RESEARCH OBJECTIVES

The Vangtat area is rich in both alluvial and hard rock (primary) gold mineralization. Due to the remote location and its recent discovery, the area has not been the focus of

geological studies. This research aims to correct this situation by: (1) Clarifying the nature and genesis of primary gold mineralization, and (2) Constraining the timing of gold mineralization and its relation to the regional tectonic evolution and other gold deposits in neighboring Vietnam. To this end, detailed studies were conducted on host lithologies, geochronology, ore and gangue mineralogy, hydrothermal alteration, fluid inclusions, and sulfur isotopes. An additional aim of this research is to produce exploration guidelines for the discovery and development of additional gold resources in the region.

1.6. RESEARCH METHODS

In this research, two principal methods were applied including field investigation and laboratory work.

1.6.1 Field investigation

The field investigation was conducted two times by the author and supervisor during 2018-2019. The first four weeks of fieldwork were conducted in May 2018, aiming to understand the broad regional and deposit-scale geological settings and associated gold mineralization. Activities involved collecting key ore and host rock samples. Subsequently, another four weeks of fieldwork were conducted in April 2019, focussing on collecting additional samples for mineralogy and K-Ar analysis. The field investigations included diamond drill cores logging, geological and structural mapping in the Vangtat deposits and other prospects at the Vangtat gold belt.

1.6.2 Laboratory work

The laboratory work composed of (1) Petrographic observation and scanning electron microprobe (SEM) with energy-dispersive spectroscopy (EDS) applied to identify ore and gangue minerals and host rocks, (2) X-ray diffraction (XRD) applied for mineral identification of bulk mineral samples and samples of mineral white mica separates, (3) Electron microprobe analysis (EPMA) with wavelength dispersive spectroscopy analysis for sulfide minerals identification (i.e. pyrite and arsenopyrite), and gold, (4) Laser Raman Spectroscopy analysis for graphite transformation, (5) Fluid inclusion petrographic identification, microthermometric analyses, and measurement of fluid composition, (6) Conventional sulfur isotope analyses, and (7) K-Ar radiometric dating age of hydrothermal white mica. These analytical works were conducted in the laboratories of Akita University. The radiometric dating (K-Ar) analyses of separated white mica samples were conducted at Okayama University of Science.

1.7. THESIS STRUCTURE

In addition to this introductory chapter, the thesis has been divided into the following chapters:

Chapter 2 includes (1) an overview of the tectonic setting of the Indochina Terrane within mainland SE Asia, with emphasis on the collision zone in the eastern extension of Indochina Terrane within the Kontum Massif, (2) a description of the regional geology in southeastern Laos and district-scale of the Vangtat gold belt, and (3)

identification of the geological features that control gold mineralization in the Vangtat deposit.

Chapter 3 describes the detailed mineralization characteristics of the Vangtat gold deposit, including sections on hydrothermal alteration, ore and gangue mineralogy, and paragenetic relations of gold mineralization.

Chapter 4 presents the results of ore mineral chemistry, including pyrite, arsenopyrite, and gold, and describes the nature and genesis of the Vangtat gold deposit based on fluid inclusion and sulfur isotope studies.

Chapter 5 presents the results of K-Ar geochronology of gangue mineral, white mica-bearing mineralized quartz-sulfide vein, to constrain the timing of gold mineralization in the Vangtat gold belt and its relation to the regional tectonic evolution.

Chapter 6 summarizes the collected data of the Vangtat gold deposits, and proposes a genetic model for the Vangtat deposit, Vangtat gold belt, southeastern Laos.

CHAPTER 2 GEOLOGY

2.1. INTRODUCTION

The Vangtat gold belt is part of the tectonically complex mainland southeast (SE) Asia, and it is directly associated with the collision between the Indochina Terrane and the Kontum Massif. Mainland SE Asia is composed of a collage of continental blocks, including the Indochina, South China, and Sibumasu Terranes (Figure 2.1), which derived from Gondwanaland at different periods in the Phanerozoic (Metcalfe, 1999). These tectonic fragments are assembled by the closure of multiple Tethyans (i.e. Paleo-, Meso- and Neo-Tethyan) and back-arc oceanic basins, now represented by suture zones (Metcalfe, 2011).

The Indochina Terrane (also called Indosinia) is a major tectonic unit that forms the eastern region of mainland SE Asia (i.e. encompassing Laos, Vietnam, Cambodia, central and eastern Thailand). It is bound to the north by the South China Terrane (also known as Cathaysia) and to the west by the Sibumasu Terrane (also called as Shan Thai), with the Truong Son, Loei, and Sukhothai fold belts marking the various suture zones (Figure 2.1; Metcalfe, 1996; Lepvrier *et al*., 2004; Hutchison, 2014). Broadly coincident with these tectonic collisions, several internal domains were amalgamated to the Indochina Terrane during the late-Permian to early-Triassic with right-lateral shear movement (Lepvrier *et al*., 2008; Osanai *et al*., 2008).

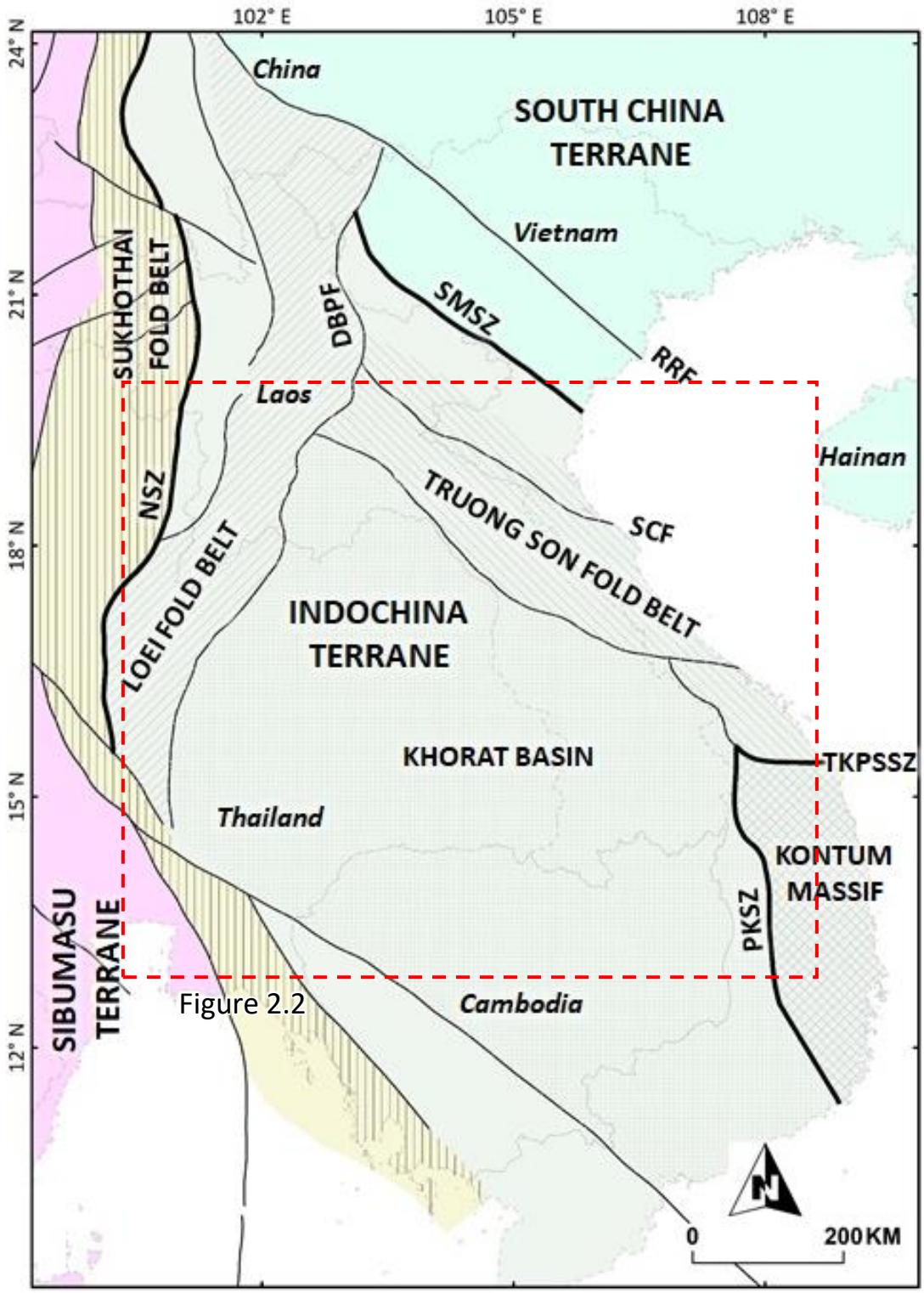

Figure 2.1. Main lithotectonic terranes and domains of mainland southeast Asia (Modified from Nakano *et al.*, 2007; Lepvrier *et al.*, 2008). Abbreviation: DBPF: Dien Bien Phu Fault; NSZ: Nan Suture Zone; PKSZ: Poko Suture Zone; RRF: Red River Fault; SCF: Song Ca Fault; TKPSSZ: Tam Ky-Phuoc Son Suture Zone

Continent-continent and island arc-continent collision zones involve the Indochina, South China, and Sibumasu Terranes, and they host several precious- and base-metals mineralized belts. These mineralized belts are associated with tectonism, magmatism, and metamorphism along domain boundaries within the Indochina terrane (Figure 2.1, 2.2).

2.2. TECTONIC FRAMEWORK OF THE INDOCHINA TERRANE

The collision of the northern and northeastern margins of the Indochina Terrane and subduction beneath the South China Terrane defines the northwest-trending Song Ma suture zone (Figure 2.1; Lepvrier *et al.,* 2004). Geochronological studies of magmatic and metamorphic rocks confined the timing of the amalgamation to the Permian-Triassic (ca. 270-230 Ma; Lepvrier *et al.*, 2004; Osanai *et al.,* 2008; Owada *et al.*, 2016). The collision between the Indochina and South China Terranes resulted in the formation of internal domains with associated metamorphism and magmatism, including the Tam Ky-Phuoc Son and Poko suture zones, and the magmatic arc of the Truong Son fold belt (Figure 2.1; Lepvrier *et al.,* 2004; 2008).

The Kontum Massif represents a core complex of the Indochina Terrane (Hutchison, 1989), and it is enclosed by the Tam Ky-Phuoc Son and Poko suture zones along the northern and western margins, respectively (Figure 2.1). The Tam Ky-Phuoc Son and Poko suture zones separate high grade metamorphic rocks (granulite facies) of the Kontum Massif from the lower grade metamorphic rocks and sedimentary sequences of the Truong Son fold belt to the north and the Khorat Basin (within the Indochina Terrane) to the west (Figure 2.1; Tran *et al.,* 2014).

The western flank of the Indochina terrane is marked by the Loei fold belt, which extends from northwestern Laos through northeastern Thailand to Cambodia (Figure 2.1). The Loei fold belt is bound to the west by the Sukhothai fold belt along the Nan suture zone (Figure 2.1; Bunopas, 1981; Zaw *et al.*, 2014). The two magmatic arcs, Loei and Sukhothai fold belts, formed as a result of the collision between the Indochina Terrane in the east and the Sibumasu Terrane in the west, during the late-Triassic to early-Jurassic (Bunopas, 1981; Charusiri *et al.*, 2002). The Khorat Basin formed subsequent to the collision orogenesis within the Indochina Terrane (Figure 2.1), characterized by the sequences of Mesozoic (middle-Triassic to late-Cretaceous) continental sedimentary rocks (red bed), overlain the late-Palaeozoic shallow-marine and littoral-fluvial sedimentary rocks, depositing on oceanic basin basement rocks of the Indochina Terrane (Minezaki *et al.*, 2019), and the metamorphic complexes of the Kontum Massif (Faure *et al*., 2018).

2.3. METAL DEPOSITS OF THE INDOCHINA TERRANE

Several precious- and base-metal deposit, notably porphyry-related skarn, epithermal, sediment-hosted, and orogenic gold deposits occur within and along the domains surrounding the Indochina Terrane, including the Truong Son and Loei fold belts and the Tam Ky-Phuoc Son and Poko suture zones (Figure 2.2; Zaw *et al*., 2014; Kirwin and Royle, 2019). Porphyry-related skarn and epithermal deposits are associated with early-Permian to middle-Triassic magmatic intrusions of the Truong Son and Loei fold belts (Zaw *et al*., 2014). The orogenic gold deposits are commonly hosted in the

regional metamorphic belt within the Ky-Phuoc Son and Poko suture zones, however, the age of gold mineralization is poorly constrained.

2.3.1 Truong Son fold belt

The Truong Son fold belt is mainly composed of magmatic rocks. According to previous geochronological data, these magmatic complexes can be grouped into two episodes: (1) an early-episode (300-270 Ma; U-Pb zircon: Cromie, 2010, unpublished data; Liu *et al.*, 2012), which occurred as a result of oceanic subduction involving the Indochina and South China Terranes, and (2) a later-episode (250-200 Ma; U-Pb zircon: Liu *et al.*, 2012; $^{40}Ar/^{39}Ar$ muscovite and biotite: Sanemastu *et al*., 2011) which is interpreted to be the result of collision-related metamorphism and post-collision magmatism. The hypothesized gap (ca. 270-250 Ma) between the two episodes is considered to represent the peak of the collision between the two Terranes (Osanai *et al*., 2008; Zaw *et al.*, 2010).

The volcanic-plutonic rocks of the Truong Son fold belt host significant precious- and base-metal deposits (Figure 2.2), such as (1) Sepon Cu-Au-(Mo) porphyry district which is associated with early-Permian rhyodacite porphyry and includes Cu-Mo porphyry mineralization, Cu-Au porphyry-related skarn, and distal sediment-hosted disseminated Au deposits (Smith *et al*., 2005; Cannell and Smith, 2008; Cromie, 2010, unpublished data), (2) Cu-Au porphyry-related skarn of the Phukham deposit and Au-Ag epithermal mineralization at Ban Huay Xai deposit, which is associated with early-Permian andesitic rocks (Manaka *et al*., 2009; Zaw et al., 2010), and (3) Sn-bearing the Triassic granitoids in the Phon Tiou deposit (Sanematsu *et al*., 2011).

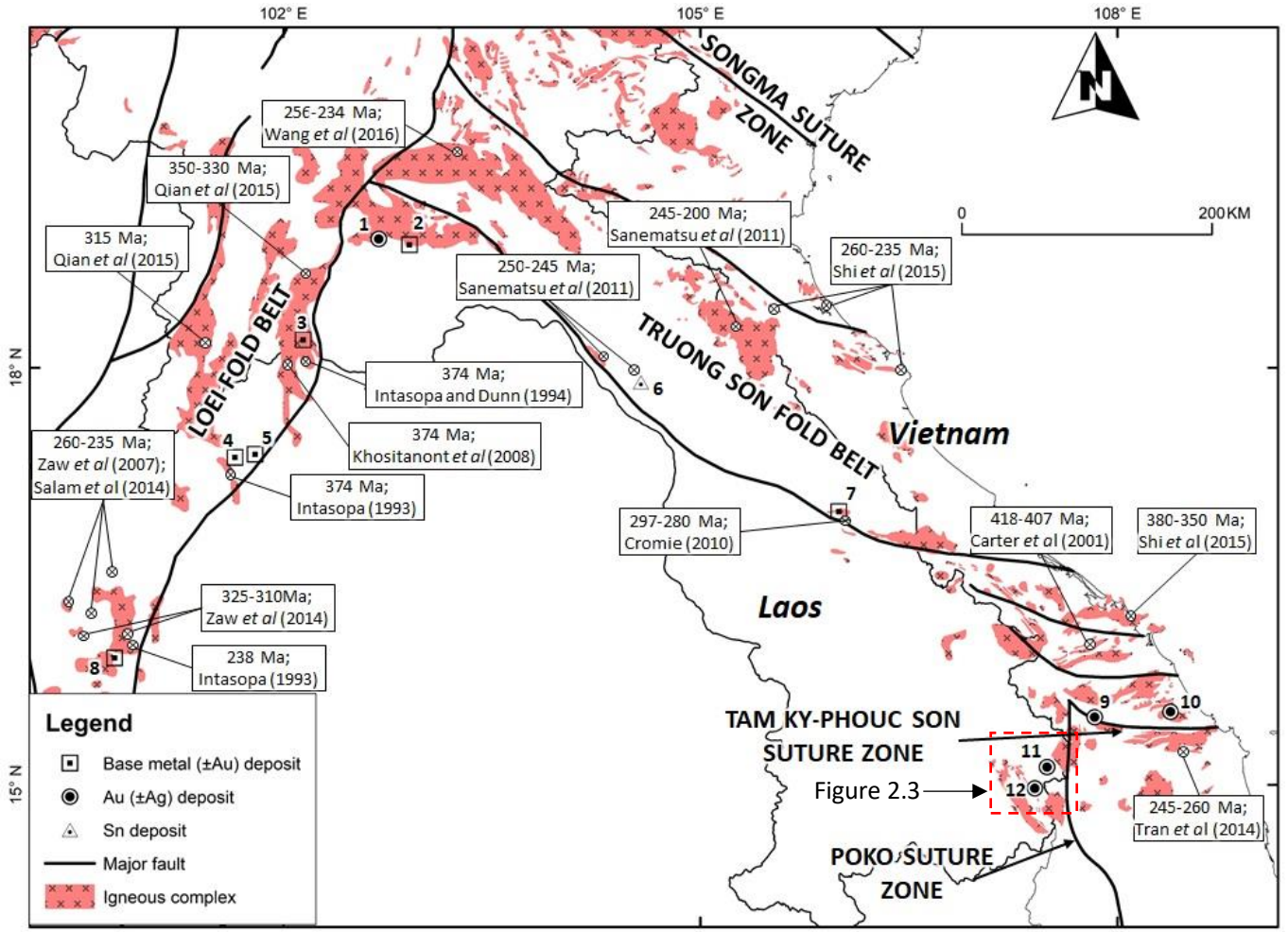

Figure 2.2. Igneous complexes along the domain boundaries of the Indochina Terrane, and associated metallogenic belts. 1: Ban Huay Xai, 2: Phukham, 3: Phulon, 4: Phuthep, 5: Phu Thap Fa, 6: Phon Tiou, 7: Sepon, 8: Chatree, 9: Phuoc Son, 10: Bong Mieu, 11: Xekong, 12: Vangtat

2.3.2 Loei fold belt

Multiple generations of volcanic-plutonic rocks are present in the Loei fold belt as the result of the eastward subduction of the Paleo-Tethys oceanic crust beneath the western Indochina Terrane during the Indosinian orogeny (Bunopas, 1981). These volcanic-plutonic rocks intruded Palaeozoic (Silurian to Permian) marine sedimentary sequences (Salam *et al.,* 2014) and host several significant economic metals deposits. Zaw *et al.* (2014) summarized the metallogenesis of the Loei fold belt, which consists of Cu ± Au ± Fe porphyry-related skarn in the Phulon, Phuthep, and PhuThap Fa deposits, and the Chatree epithermal Au-Ag deposit (Figure 2.2).

2.3.3 Tam Ky-Phuoc Son suture zone

The Tam Ky-Phuoc Son suture zone is made up of magmatic and metamorphic complexes. The magmatic complexes include numerous plutons, pegmatite dykes and sills of variable composition, ranging from mafic to felsic (Nguyen Van Trang, 1986). The age of these intrusive rocks ranges from Silurian to Triassic (Carter *et al*., 2001; Nagy *et al*., 2001; Lepvrier *et al*., 2004); the older rocks (Silurian to Devonian) have undergone several ductile deformation stages and high-grade recrystallization events (Carter *et al*., 2001; Nagy *et al*., 2001), while the younger episode (Permian to Triassic) appears to intrude and/or crosscut early regional deformational fabrics and has undergone only minor brittle deformation (Lepvrier *et al.,* 2004; Tran *et al.,* 2014).

Several gold deposits and prospects, including the well-known Phuoc Son and Bong Mieu gold deposits (Figure 2.2) commonly hosted in the metamorphic complexes and

associated with structural settings within the Tam Ky-Phuoc Son suture zone (Quynh *et al.*, 2004; Manaka *et al*., 2010; Tran *et al*., 2014). Tran *et al*. (2014) proposed that gold mineralization at the Bong Mieu deposit in the Tam Ky-Phuoc Son suture zone in central Vietnam occurred originally during an initial ductile shear event at ca. 430 Ma and, subsequently, gold was remobilized to form auriferous quartz veins with sulfides during a brittle-ductile deformation event at ca. 240 Ma (Middle Triassic) based on a Re-Os molybdenite age. Hydrothermal biotite for the Phuoc Son gold deposit was dated by Manaka (2014) at 212 and 204 Ma (Late Triassic).

2.3.4 Poko suture zone

The Poko fault (Figure 2.3) controls the sheared paleo-suture zone of late-Permian to early-Triassic age known as the Poko suture zone (Lepvrier *et al.*, 2004; 2008). The Poko suture zone merges with the Tam Ky-Phuoc Son suture zone in the Kham Duc area and extends into southern Vietnam (Figure 2.1; Lepvrier *et al*., 2004). The north-trending Poko suture zone broadly marked the geological boundary between the western Kontum Massif and the Khorat Basin within the eastern extension of Indochina Terrane, mainly composed of intrusive rocks and regional metamorphic sequences, which were overlain by the Mesozoic (middle-Triassic to late-Cretaceous) continental sedimentary sequences of the Khorat Basin (Smith and Stoke, 1997; Vilayhack *et al*., 2008; Faure *et al*., 2018).

The regional structure of the Poko suture zone can be traced over several tens of kilometers into the western part of Kontum Massif (Lepvrier *et al.*, 2004). Subsidiary structures associated with the regional Poko suture zone hosted numerous gold-bearing

quartz vein deposits, which in many cases form major gold deposits (Figure 2.2, 2.3). Among these is the Vangtat gold deposit and several gold deposits and prospects in the same district within the Vangtat shear zone, which lies approximately 30 km to the west of the Poko suture zone (Figure 2.3). The Phuoc Son deposits occur in the northwest flank of the Poko suture zone where it intersects the E-W trending Tam Ky-Phuoc Son suture zone. Intrusive igneous rocks further to the west (~50 km) of the Poko suture zone host several Cu-(Au) and Pb-Zn deposits and prospects (Figure 2.3), with porphyry copper and skarn deposit affinity (e.g. Sanematsu *et al.*, 2011).

2.4. DISTRICT GEOLOGY

The Kontum Massif is mainly composed of early- to mid-Palaeozoic (Cambrian to Devonian) metamorphic complexes, including pelitic gneiss and granulite (Kannack complex), amphibolite-facies metamorphic rocks (Ngoc Linh complex), and pelitic, psammitic, mafic, and calc-silicate schist and gneiss (Kham Duc complex) (United Nations, 1990; Osanai *et al.*, 2008). The metamorphism in the Kontum Massif is divided into early (~270 Ma) prograde and late (ca. 260-230Ma) retrograde events (Osanai *et al.*, 2008), broadly contemporaneous (ca. 260-250 Ma) with the mafic intrusive rocks (metagabbro and charnockite) in the Kontum Massif (Owada *et al.*, 2016).

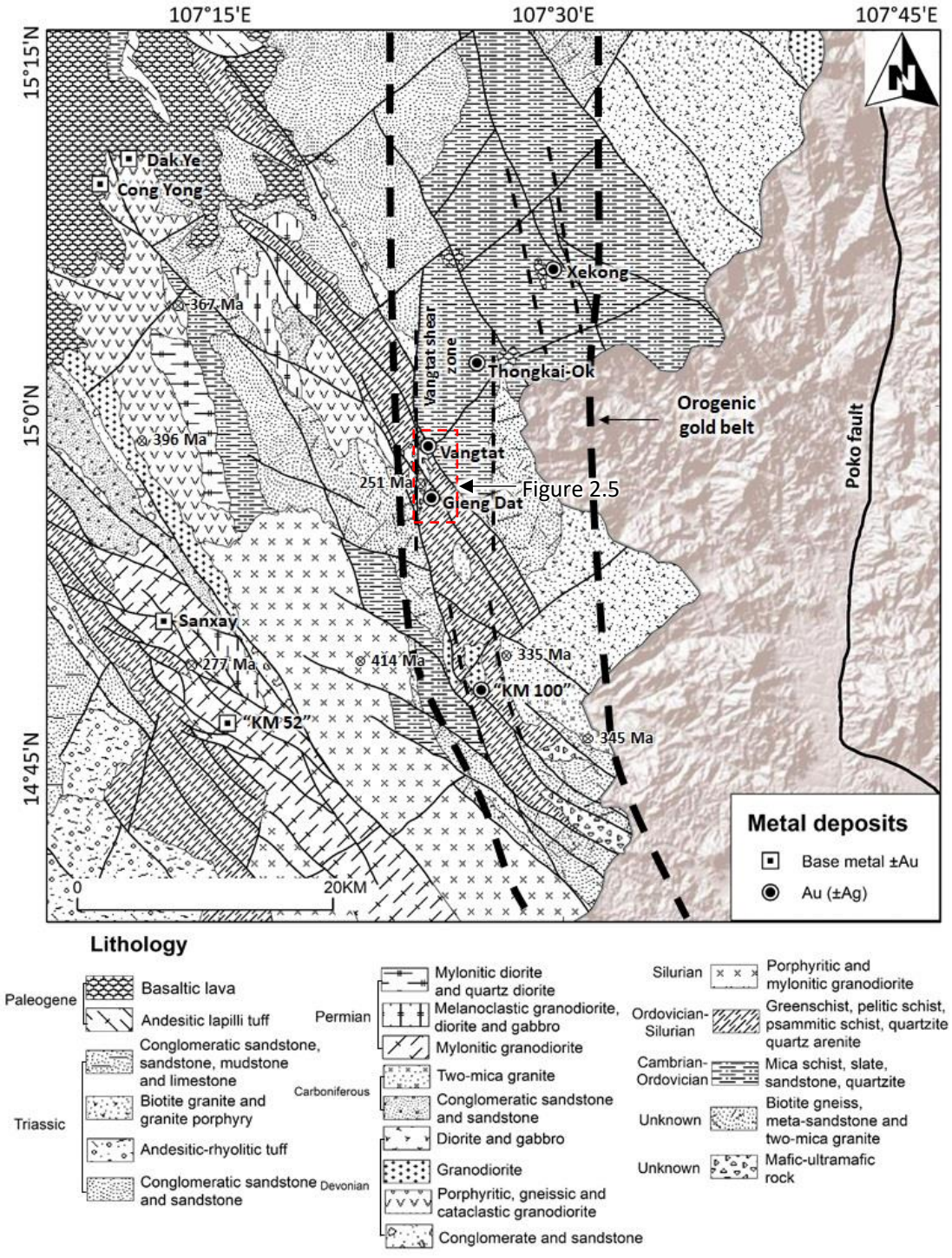

Figure 2.3: Simplified regional geological map of southeastern Laos showing the distribution of metals deposits (modified from Vilayhack *et al*. (2008), and the data of age dating of granitoids are adapted from Sanematsu *et al.* (2011)).

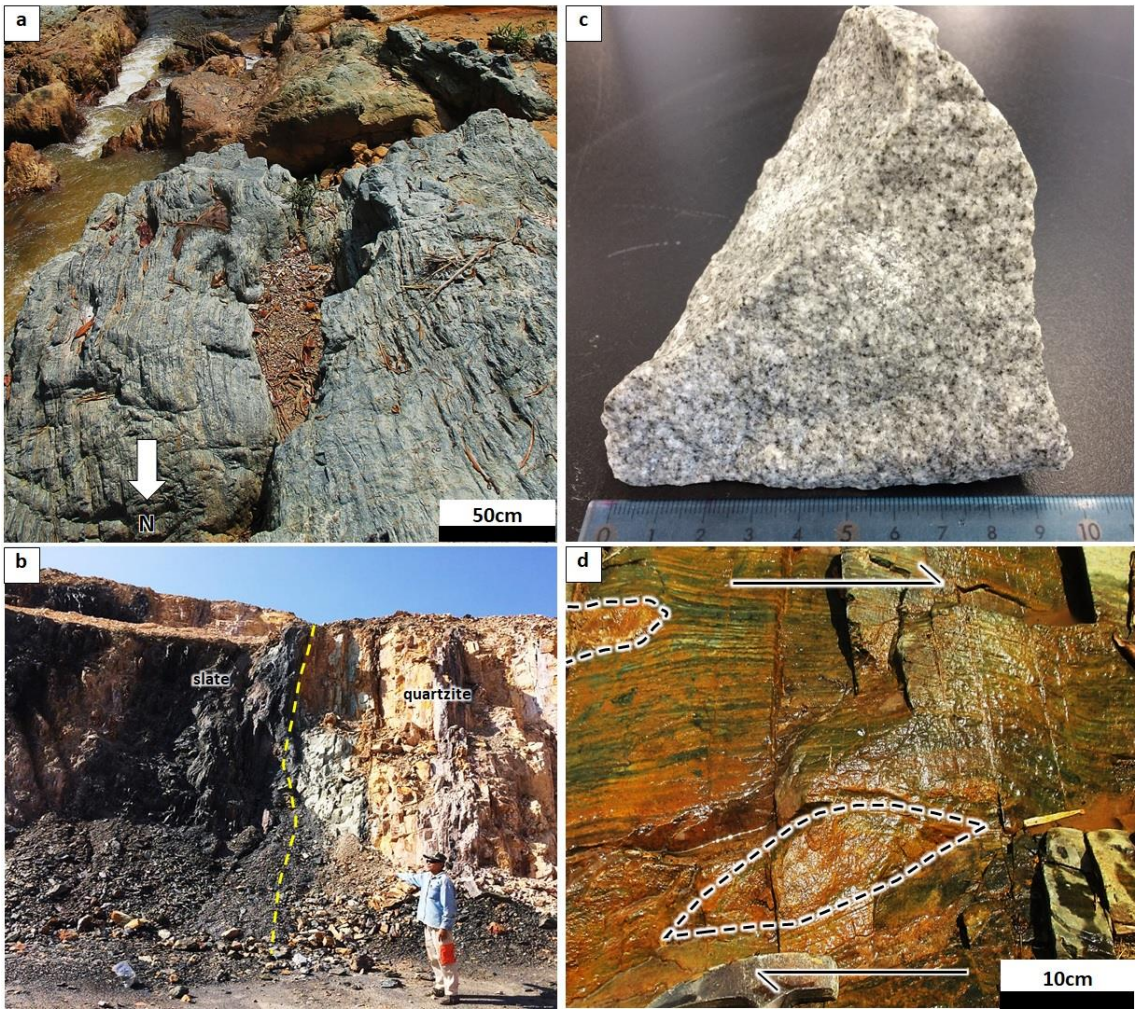

Figure 2.4: Outcrop lithology of the Vangtat shear zone. a). The N-S schistosity of pelitic schist; b). The occurrence of slate, and quartzite characterized by steeply dipping schistosity; c). Two-mica granite; and d) Asymmetrically deformed boudinage of greenschist in the Vangtat shear zone.

The western margin of Kontum Massif marks the Vangtat shear zone (Figure 2.3), one of the subsidiary structures associated and paralleled to the Poko suture zone. The Vangtat shear zone is the main host of a newly discovered gold belt, which consists of several gold deposits and prospects, and extends for greater than 20 km along strike, broadly marking the border between southeastern Laos and central Vietnam (Figure 2.3). The Vangtat shear zone is mainly composed of early- to mid-Palaeozoic metamorphic rocks: (1) Cambrian-Ordovician mica schist, slate, sandstone, and quartzite, and (2) Ordovician-Silurian greenschist, pelitic schist, psammitic schist, quartzite, and quartz arenite (Figure 2.3; Vilayhack *et al*., 2008). These metamorphic sequences are similar to the low-grade metamorphic Kham Duc complex, and they were metamorphosed during the Indosinian tectonic event (270-230 Ma; Lepvrier *et al.*, 2004; Osanai *et al.*, 2008). The metamorphic rocks are strongly sheared, with a north-northwest and north-striking schistosity (Figure 2.4a), and commonly contain asymmetrically deformed boudinage indicative of a right-lateral, strike-slip shearing (Figure 2.4d).

The regional metamorphic sequences of the Vangtat shear zone were intruded and sandwiched by a series of mylonitic, gneissic, and undeformed intrusive rocks (Figure 2.3; Vilayhack *et al*., 2008). Recent geochronological studies of these intrusive rocks revealed a wide range of ages from Ordovician to Triassic (ca. 415-250 Ma, Ar-Ar dating of muscovite and biotite by Sanematsu *et al.* (2011); and 485-465 Ma, U-Pb dating of zircon by Gardner *et al.*, 2017, and Wang *et al.*, 2020). The whole-rock chemistry of these intrusive rocks suggests a subduction-related island arc environment with an adakitic signature (Sanematsu *et al*., 2011; Gardner *et al*., 2017). Most intrusive rocks occur along the margin of the Vangtat shear zone, and a local

granite is found in the southernmost region of the Vangtat shear zone (Figure 2.3, 2.4c). Metamorphosed and unmetamorphosed mafic-ultramafic rocks also occur within the sequences of regional metamorphic rocks in the Vangtat shear zone (Figure 2.3), the age of these rock units is not well constrained. The youngest major geologic unit in the region consists of Paleogene-Neogene basaltic lava flows (Figure 2.3; Vilayhack *et al*., 2008; Faure *et al*., 2018).

Numerous gold deposits and prospects occur in a north-south lineament along the Vangtat shear zone. From north to south these are represented by the Xekong, Thongkai-Ok, Vangtat, and Gieng Dat gold deposits (Figure 2.3). Amongst them, Vangtat is the major economic gold deposit and it is currently being mined.

2.5. GEOLOGICAL SETTING OF THE VANGTAT DEPOSIT

The Vangtat deposit represents the major deposit in the Vangtat gold belt, hence the identified geological setting, wall rock lithologies, and associated mineralization of the Vangtat gold deposit would help understand the mineralization style in the Vangtat gold belt. The lithological units around the Vangtat deposit as well as other hard-rock (primary) gold deposits within the Vangtat gold belt are covered by a thick (~up to 50 m) weathering/oxidation blanket which led to local gold remobilization and concentration of secondary gold in surficial detrital sediments. In order to clarify the geological setting, wall rock lithologies, and primary gold mineralization this study focused on logging of drill core sample and within the Vangtat deposit and mapping in the open-pits.

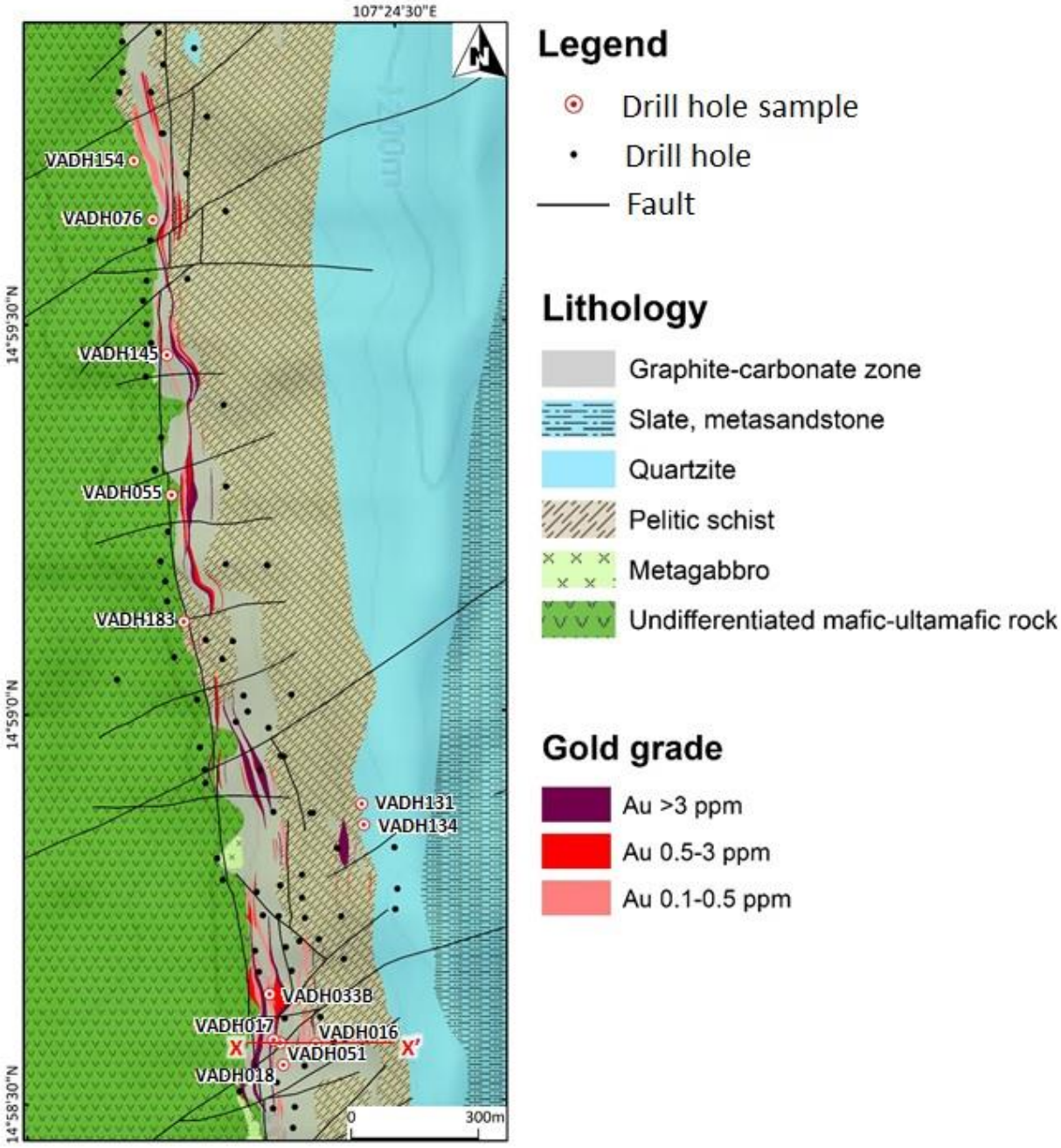

Figure 2.5: Geological map of the Vangtat deposit showing host lithologic units and gold mineralization. X-X' is a cross section line for Figure 2.6

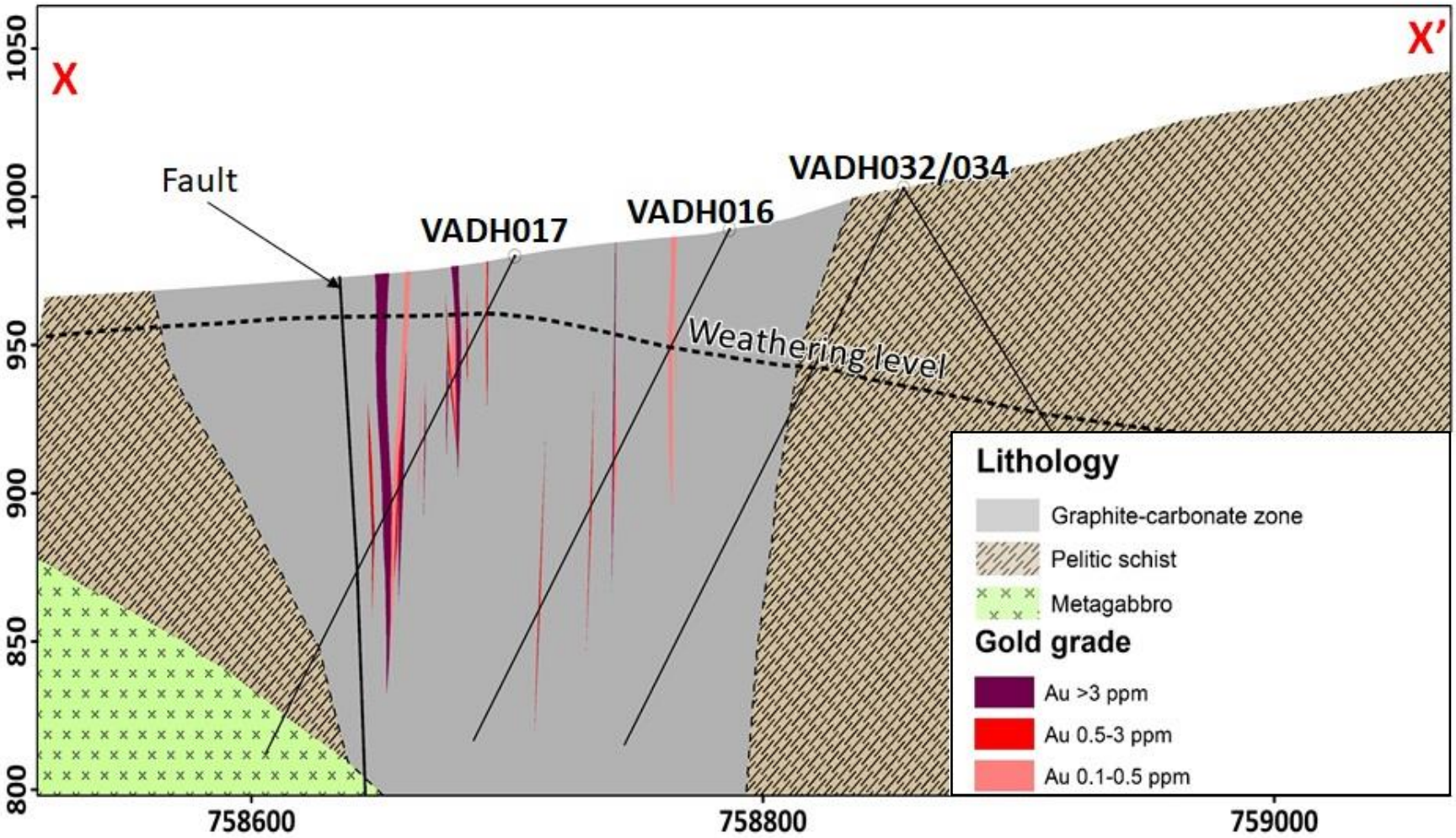

Figure 2.6: A schematic cross-section through the Vangtat ore body

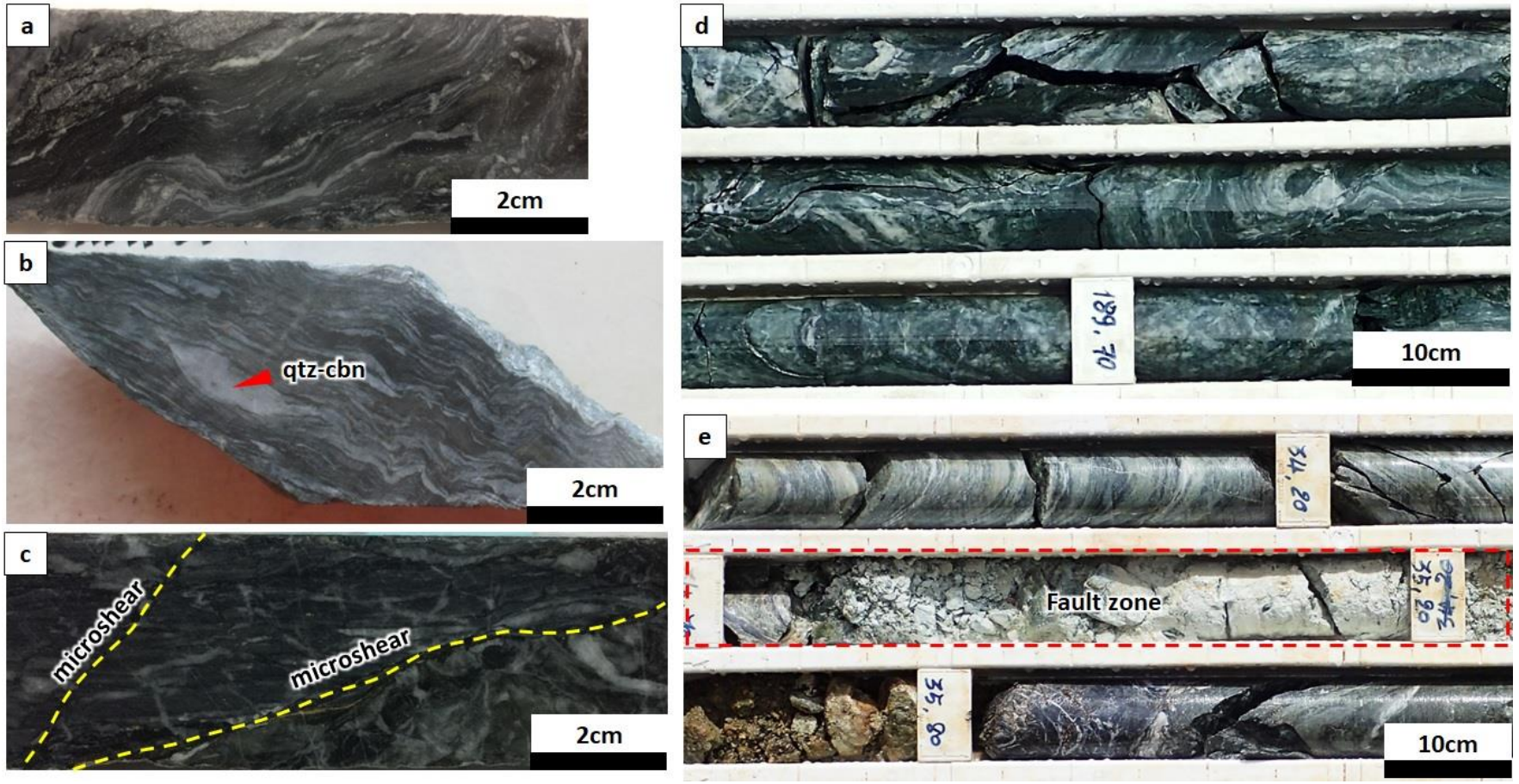

Figure 2.7: Drill core sample photographs showing the ductile deformation of the regional metamorphic host rock (i.e. pelitic schist) (a, b); and was overprinted by brittle deformation (c-e). Abbreviation: qtz-cbn: quartz-carbonate

Two main country rocks are found in the deposit: the lower unit is made up of metagabbro, and the upper unit is composed of pelitic schist, slate, metasandstone, and quartzite (Figure 2.5, 2.6). Within the Vangtat shear zone, the metamorphic sequences are strongly affected by deformation including folding, mineral recrystallization, reorientation, and mylonite formation (Figure 2.7a,b). Ductile deformation features appear progressively overprinted by more brittle compressive deformation, including faulting, fracturing, microshears, and formation of cataclasites (Figure 2.7c-e).

2.5.1 Metagabbro

In the southern part of the Vangtat deposit, metagabbro is found below a depth of 190 m in drill hole VADH017 (Figure 2.6). The age of this mafic-ultramafic unit is unknown and it is labeled as undifferentiated in the regional-scale map (Figure 2.3). In the sample from the drill core, the metagabbro is characterized by green color with a coarse-grained, equigranular texture (Figure 2.8a). The metagabbro has been regionally metamorphosed and is mainly composed of amphibole (e.g. actinolite, tremolite, hornblende), epidote, and plagioclase, with minor K-feldspar and trace titanite (Figure 2.8). Under the microscope, actinolite and tremolite typically show prismatic and fibrous texture. Massive epidote is presented together with plagioclase and K-feldspar. Chlorite and calcite are also observed and these two minerals are indicative of the presence of hydrothermal activity (Figure 2.8b,c).

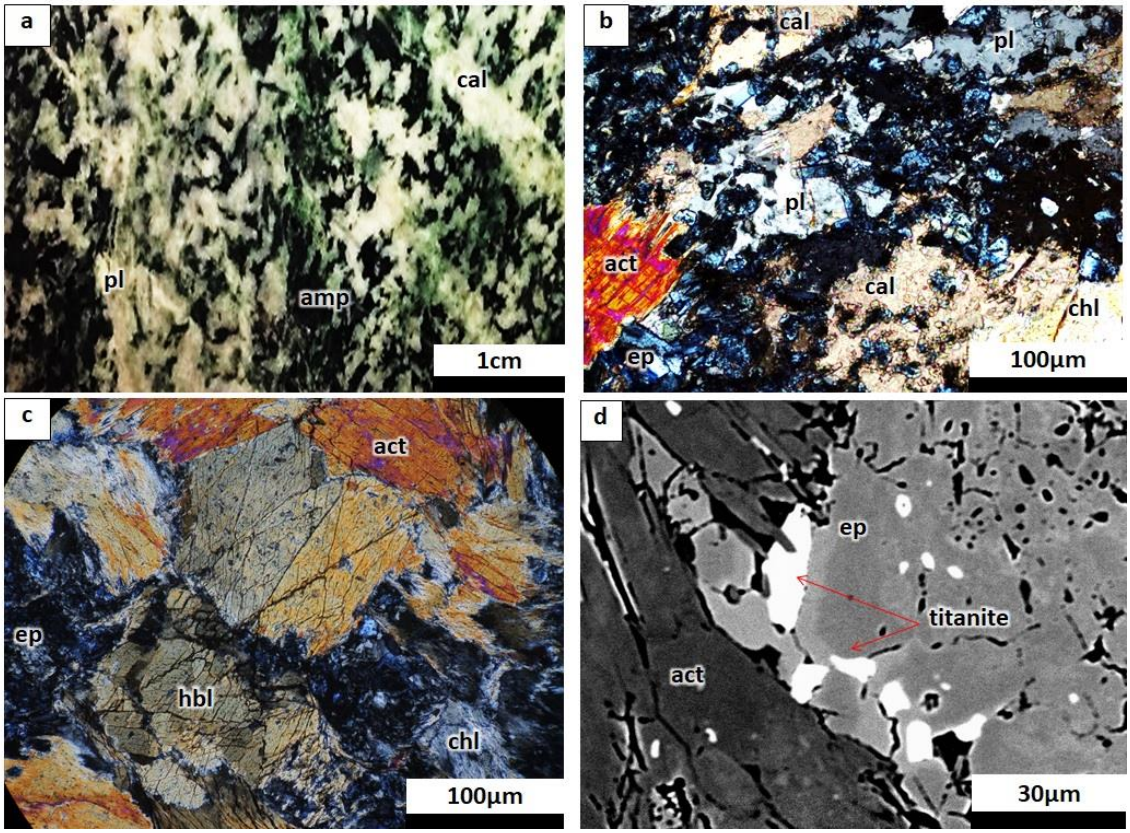

Figure 2.8: (a) Drill core photo of metagabbro within partially altered showing a coarse-grained and equigranular texture; (b and c) Photomicrographs and (d) Backscatter image showing the mineral assemblage of metagabbro. Abbreviations: act: actinolite, amp: amphibole, cal: calcite, chl: chlorite, ep: epidote, hbl: hornblende, pl: plagioclase

2.5.2 Pelitic schist

Pelitic schist occurs as large outcrops throughout the deposit and this lithologic unit marks the core of the Vangtat shear zone as well as the central part of the deposit. Pelitic schist is the principal host to the mineralized bodies, both vertically and horizontally (Figure. 2.5, 2.6). This pelitic schist unit is made up of foliated muscovite and chlorite with finely interlayer quartz and plagioclase (Figure. 2.9a,b). It has a distinct schistose texture as a result of the intense deformation, foliation (Figure 2.9a) and metamorphism of a sedimentary protolith. Calcite, dolomite, epidote, and K-feldspar, as well as trace amounts of opaque minerals (i.e. pyrite, magnetite, hematite), are the main mineral constituents of the pelitic schist (Figure. 2.9d,e).

Quartz, quartz-carbonate and pyrite porphyroblasts and mylonite are commonly observed in the pelitic schist (Fig. 2.9c,d). These textures are formed by the lineation and foliation of muscovite and chlorite enclosing quartz, carbonate, and pyrite boudins, and are associated with pressure shadows, suggesting the shear deformation occurred during metamorphism. Fine-grained (<200 μm) individual euhedral pyrite crystals are observed along the foliated metamorphic chlorite and muscovite (Figure 2.10c,d), indicating that pyrite was deformed and recrystallized during regional metamorphism.

The pelitic schist also contained a minor amount (< 1 vol%) of carbonaceous (graphitic) material, which is frequently found as a dark material interleaved in the foliated texture of chlorite-muscovite (Figure 2.10a,b). The amount of graphite increases toward the strongly sheared (deformation) zones.

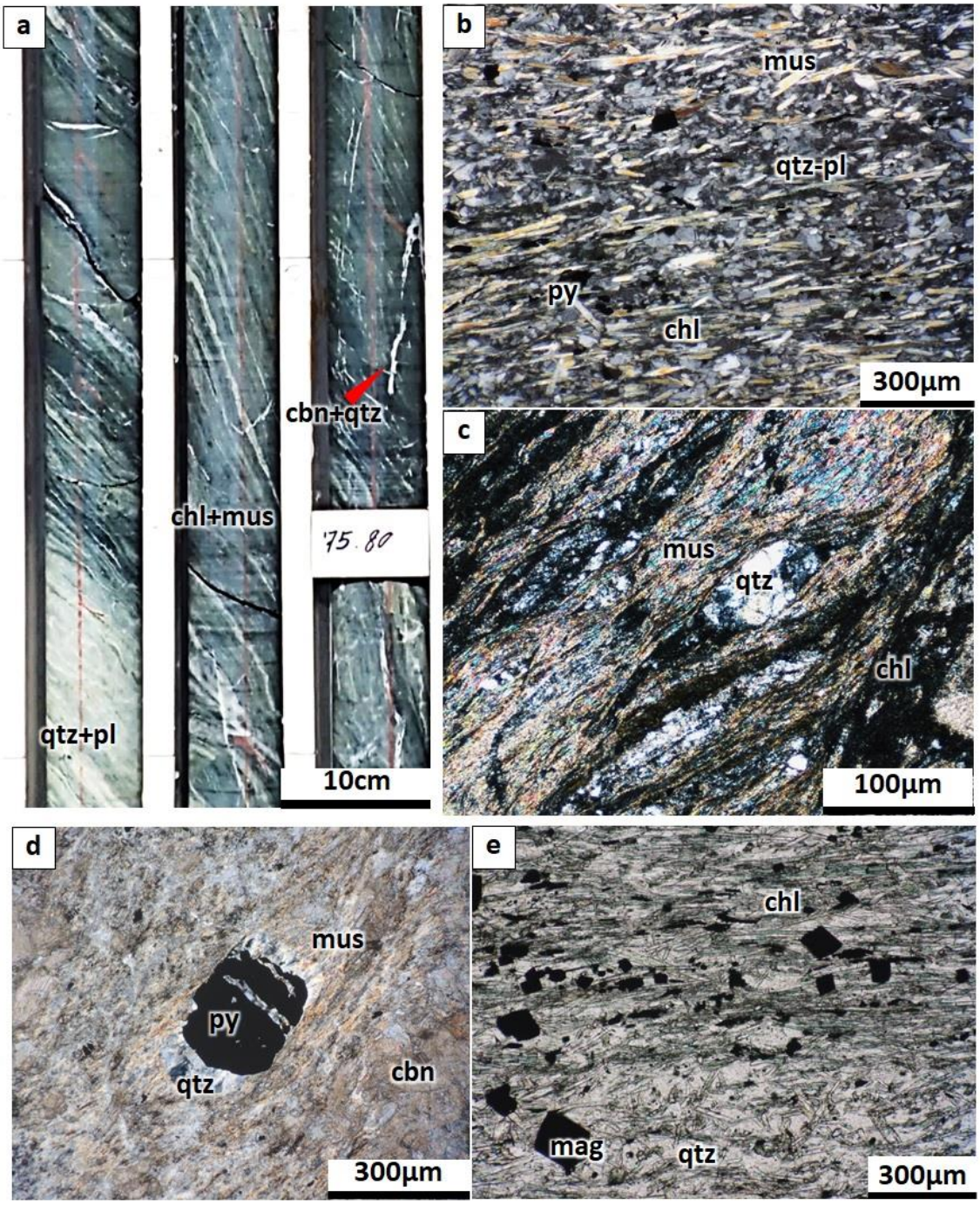

Figure 2.9: (a) Drill core sample showing the typical texture of pelitic schist; (b) The elongation and orientation of muscovite and chlorite within the interlayer of quartz-plagioclase and pyrite dissemination; (c) Quartz porphyroblast being surrounded by fibrous muscovite and chlorite; (d) Pyrite porphyroblast showing the pressure shadow and surrounded by lineation of muscovite; and (e) Photomicrograph showing the magnetite disseminated in the pelitic schist. Abbreviation: cal: calcite, cbn: carbonate, chl: chlorite, gr: graphite, mag: magnetite, pl: plagioclase, py: pyrite, qtz: quartz

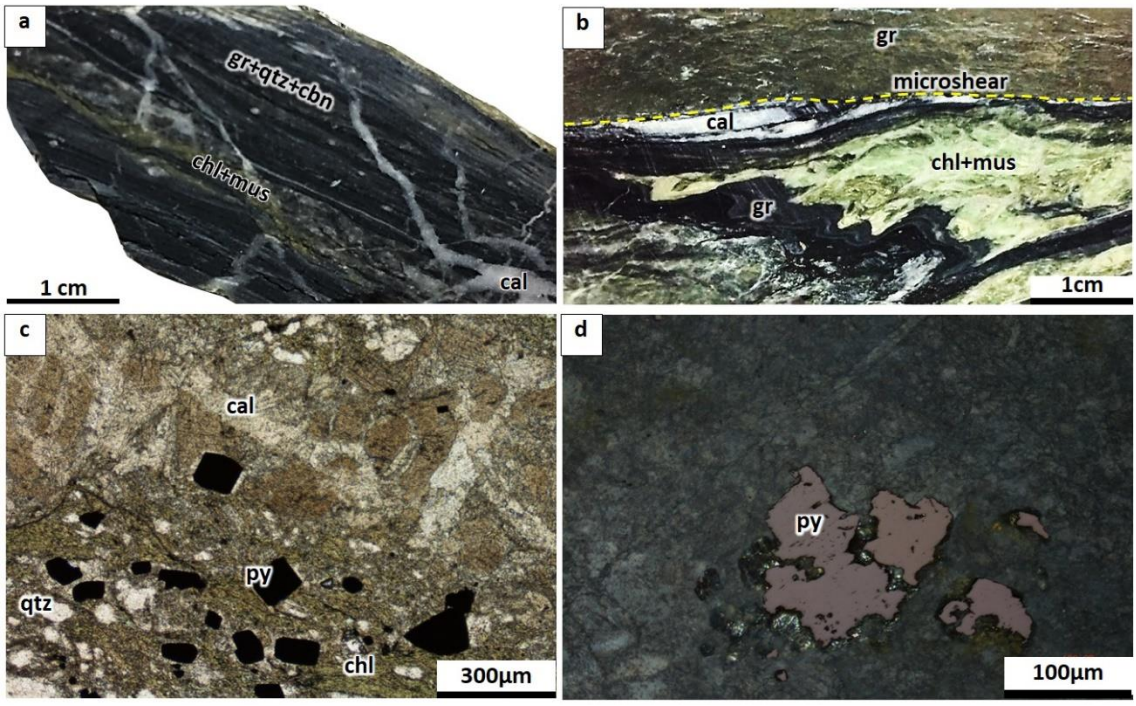

Figure 2.10: (a and b) Drill core photos showing the graphite composed in the foliation texture of chlorite and muscovite; (c) The euhedral shape of pyrites growth across the precursor metamorphic foliation; and (d) Aggregated pyrite in the host pelitic schist. Abbreviation: cal: calcite, chl: chlorite, gr: graphite, py: pyrite, qtz: quartz.

2.5.2.1 Graphitic content in pelitic schist

As mentioned above, the graphitic or carbonaceous material is widespread in the pelitic schist, commonly interleaved with metamorphic chlorite-muscovite, suggesting that the graphitic material originated as detrital fragments that are dispersed through protolith sediments. The layers of graphite were segregated in the pelitic schist pile, associated with the metamorphic chlorite-muscovite foliation, and became deformed, including the folding and development of microshears (Figure 2.10a,b). X-ray diffraction identification displayed a sharp peak of graphite that occurred at 3.39Å, reflecting the d_{002} graphite plane spacing, which suggests apparently well-crystallized graphite. Considering the abundance of graphite in the pelitic schist within the progressively metamorphosed, recrystallization, reorientation potentially indicates graphite transformation during regional metamorphism.

2.5.2.2 Graphite transformation

Carbonaceous or graphitic material is a common component of metasedimentary rocks, which occurs in the matrix of the mineral particles, deriving from the evolution of organic matter originally present in the host sedimentary rocks (Beyssac *et al.*, 2002). During regional metamorphism, the graphitic or carbonaceous material transforms into graphite (Large *et al.*, 1994; Wada *et al.*, 1994; Beysac *et al.*, 2002). The degree of the graphitization has been widely used as an indicator of metamorphic grade as its composition depends mainly on temperature, pressure, and type of carbon precursor, and involves a transformation from disordered carbonaceous material at low

temperature to fully crystallized graphite at high temperature (Jehlicka and Beny, 1992; Wopenka and Pasteris, 1993).

Furthermore, the correlation of graphitization with metamorphic grade would characterize the reaction kinetics as a function of time and temperature, because the graphitization is believed to be irreversible; that is, graphitization provides a useful indicator of maximum metamorphic grade (Wada *et al.*, 1994). Therefore, estimating the degree of graphite transformation in the Vangtat host rock using, for example, Raman spectroscopy would allow estimating the temperature of metamorphic grade.

2.5.2.3 Raman spectra of graphite

Raman spectroscopy analyses are an essential method to characterize the degree of organization of carbonaceous material. Raman spectra and its parameters were used as a quantitative geothermometer for the graphite transformation, comparable to the temperature of metamorphic grade (Beyssac *et al.*, 2002). The Raman spectra of carbonaceous material and/or graphite is composed of the first-order (1100-1800cm^{-1}) and second-order (2500-3350 cm^{-1}) regions (Tuinstra and Koeing, 1970; Nemanich and Solin, 1979). The first-order region composes of disordered graphite or defect "D" band and fully ordered graphite "G" band, parameters of these band peaks were applied to calculate the temperature of graphite transformation.

Raman spectra of three graphite-bearing pelitic schist samples from the Vangtat deposit showed the discriminated bands in the first-order region, consisting of D1-band appearing at 1329-1347 cm^{-1}, G-band appearing at 1570-1596 cm^{-1}, and D2-band appearing at 1598-1618 cm^{-1} (Table 2.1). Poorly ordered carbon is also observed as

D3-band and D4-band appearing at 1514-151 cm^{-1} and 1271-1312 cm^{-1}, respectively (Figure 2.11b). Increasing graphite crystallinity is indicated by the increased ordering of the graphite structure as quantified by X-ray diffraction and Raman spectroscopy. Selected Raman spectra of graphite samples from the Vangtat deposit (Figure 2.11b) displayed the higher intensity of the disordered D1 band compared to the fully ordered graphite G band, which indicates the imperfect crystallization of graphite.

The band peaks of the Raman spectra were decomposed into several bands and estimated the parameters of each band peak, such as band position, band intensity, band area, and bandwidth using the software "Peak Fit 4.2" (Figure 2.11a). Beyssac *et al*. (2002) established a geothermometry equation (Eq. 1), based on area ratio: R2=D1/(G+D1+D2), applying for the regional metamorphic rocks:

$$T(°C) = -445\ (R2) + 641 \qquad \text{(Eq. 1)}$$

This equation is relevant in the temperature range from 330 to 650 °C and estimated errors are ±50 °C (Beyssac *et al.*, 2002).

2.5.2.4 Estimated temperature of graphite transformation

The data of Raman spectroscopical analyses and the resulting estimated temperatures are summarized in Table 2.1. Although several analytical points were conducted within three different graphite samples, the data show consistent results, suggesting that these are reliable data that can be used to estimate the temperature of graphite transformation. Using the equation of Beyssac *et al*. (2002) (Eq. 1), the estimated

temperature of graphite transformation for the host rocks of the Vangtat gold deposit range from 347 to 407 °C. This temperature range is consistent with the major mineral assemblage of the pelitic schist, which consists of chlorite, muscovite, quartz and plagioclase, suggesting that graphite-bearing pelitic schist had transformed under the greenschist facies metamorphic grade.

2.5.3 Slate, metasandstone, and quartzite

Slate, metasandstone, and quartzite are located on the western side of the Vangtat shear zone (Figure 2.5) and overlie the pelitic schist. Slate is composed of fine-grained particles including carbonaceous material, with well-developed cleavage and foliation, and is occasionally cut by barren pyrite-bearing quartz veins (Figure 2.12a). Metasandstone is mainly composed of recrystallized quartz grains in a matrix of fine-grained quartz and sericite (Figure 2.12b), with trace amounts of disseminated pyrite. Quartzite is massive in texture and dominated by recrystallized quartz grains with a minor amount of iron-oxide occurring along with the grain boundaries of quartz (Figure 2.12c,d).

Fine-grained pyrite (up to 200 μm size) is randomly assembled in the foliation planes of slate and associated with carbonaceous material (organic matter) (Figure 2.13a,b); it also appears disseminated in the matrix of metasandstone (Figure 2.13c,d). This generation of pyrite is commonly anhedral in shape, rounded to subrounded, often with a text reminiscent of pyrite famboids, suggesting that it has formed as a diagenetic product within the sedimentary rocks, possibly related to bacteria sulfate reduction (e.g. Berner, 1970).

Table 2.1: Results of Raman Spectroscopy analysis for graphite in the Vangtat deposit

Sample		VADH016-120.6	VADH051-102.8	VADH051-134.3
Peak center	G	1570 - 1597	1574 - 1581	1574 - 1597
	D1	1313 - 1348	1288 - 1340	1334 - 1345
	D2	1599 - 1617	1283 - 1609	1598 - 1619
Peak area	G	15134 - 142600	48142 - 86450	50175 - 140590
	D1	28537 - 176250	73678 - 129620	86590 - 293670
	D2	1250 - 20757	4446 - 10845	1150 - 23430
FWHM	G	35.28 - 67.39	55.36 - 64.69	46.22 - 65.25
	D1	40.95 - 59.69	56.95 - 62.97	53.21 - 66.29
	D2	10.29 - 34.09	26.34 - 62.18	16.39 - 54.05
R1		1.12 - 2.16	1.40 - 1.77	1.40 - 2.11
R2		0.53 - 0.66	0.54 - 0.61	0.53 - 0.65
T (°C)		347 - 407	367 - 405	351 - 405

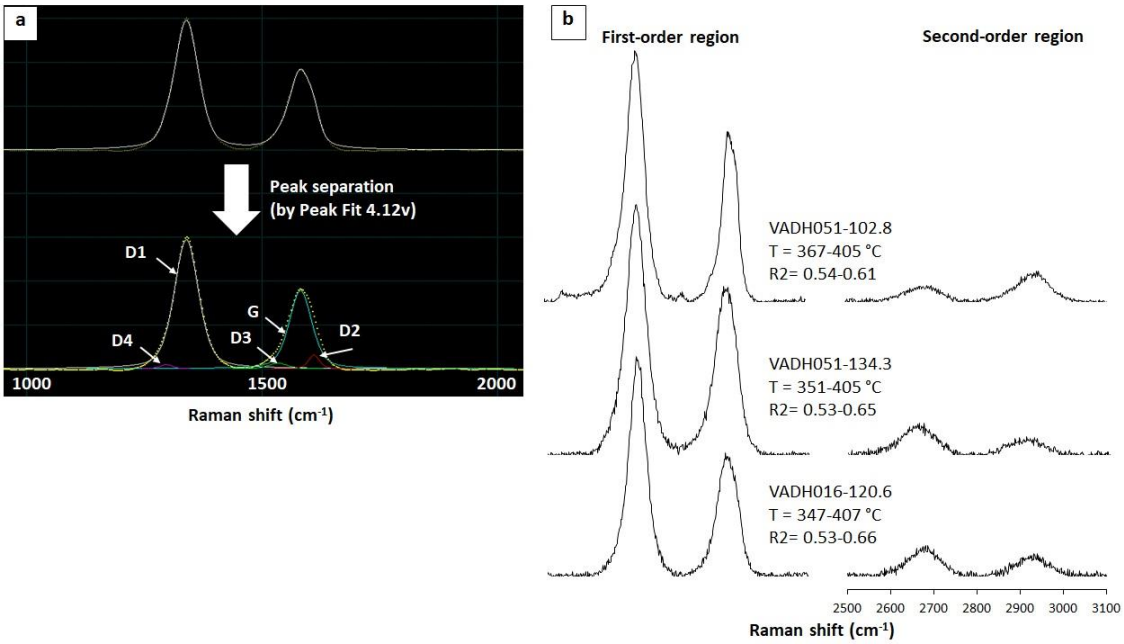

Figure 2.11: (a) Schematic illustration showing an example of peak separation from measured Raman spectra; and (b) Representative of Raman spectra obtained from 3 samples with metamorphic temperature. R2 values for each spectra are also indicated.

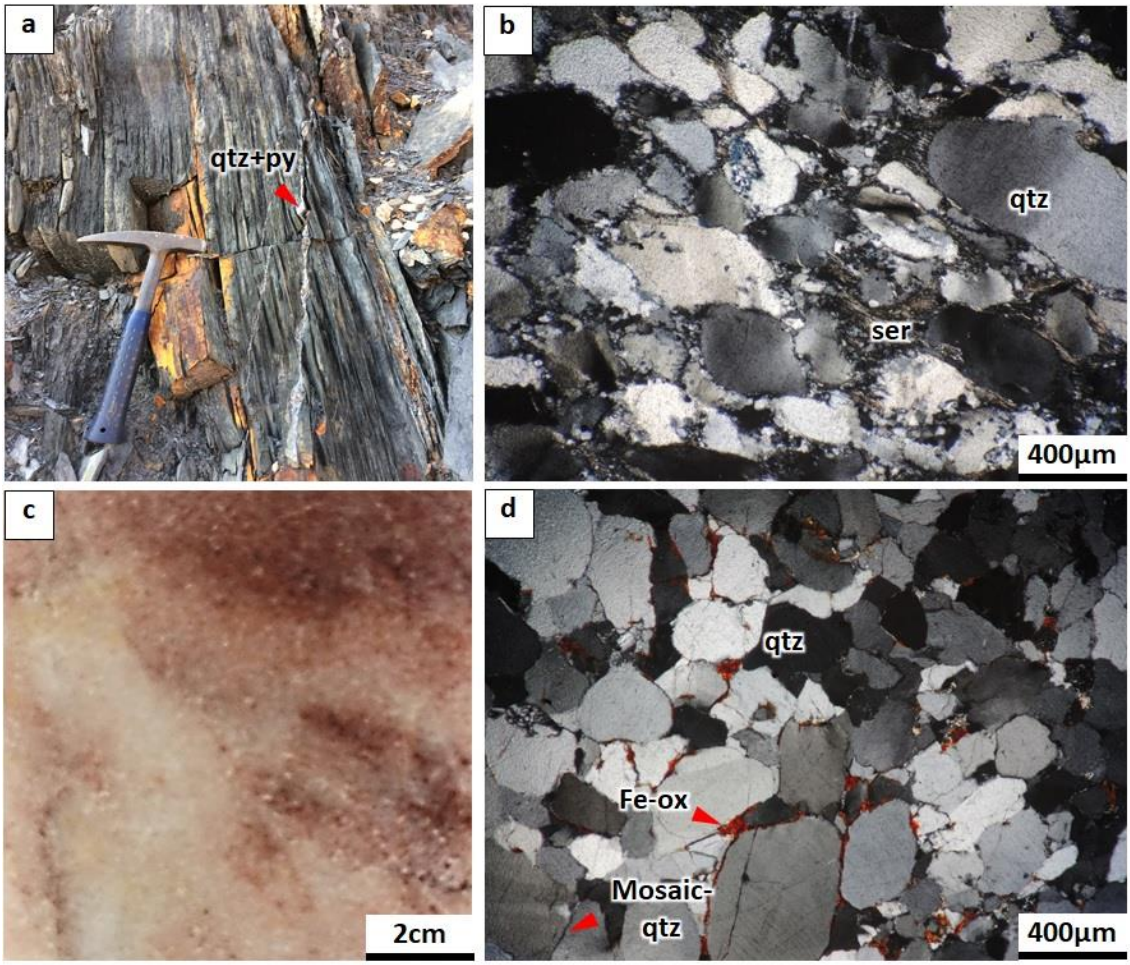

Figure 2.12: (a) Outcrop of slate showing well-developed foliation and occasionally cut by barren pyrite-bearing quartz vein; (b) Photomicrograph of the typical texture of metasandstone showing the recrystallized of quartz grains in the matrix of fine-grained quartz and sericite; (c) Hand specimen photo of quartzite; (d) Photomicrograph of the typical texture of quartzite showing the granular texture of quartz grains, and mosaic boundary, and iron oxide along the grain boundaries of quartz. Abbreviation: Fe-ox: iron oxide, py: pyrite, qtz: quartz, ser: sericite.

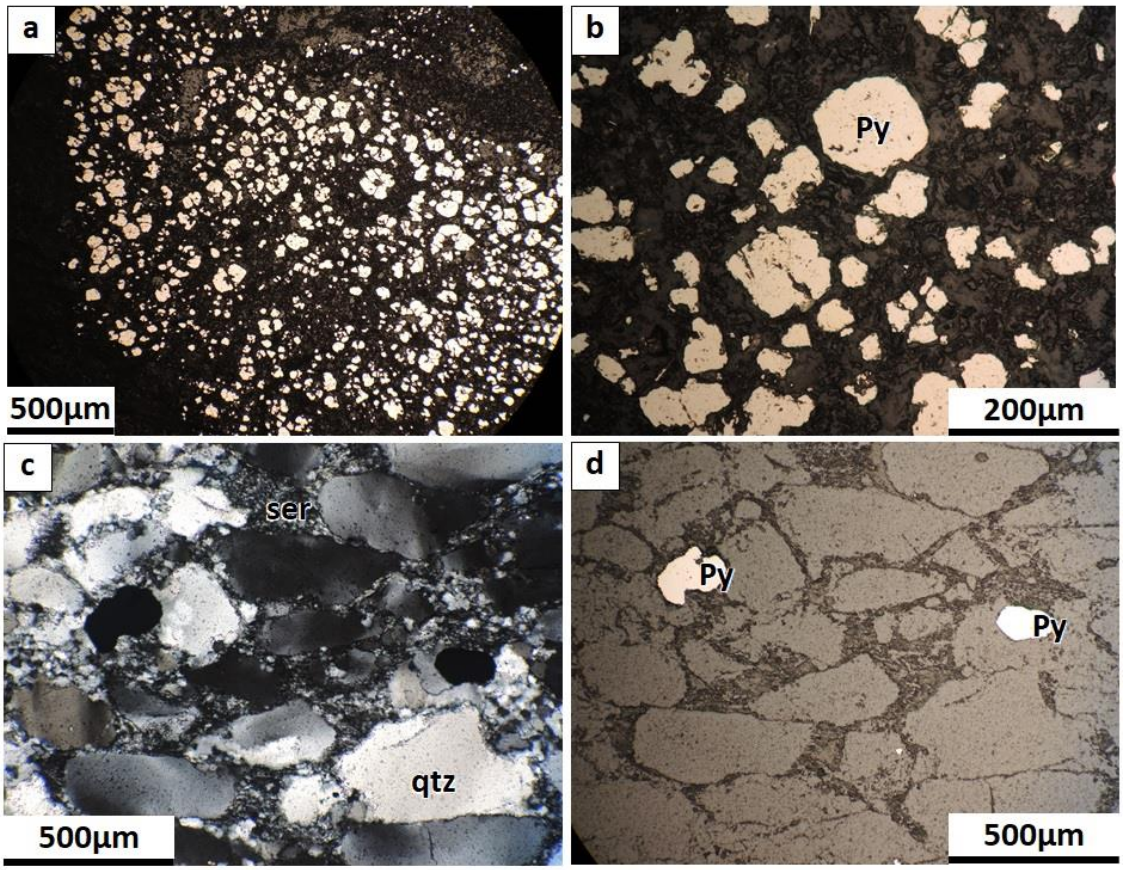

Figure 2.13: (a and b) Photomicrographs showing the subrounded to rounded of pyrite grains associated with organic matter in the foliation planes of slate; Photomicrograph of cross-polarized (c) and reflected light (d) showing the disseminated of diagenetic pyrite in the metasandstone. Abbreviation: py: pyrite, qtz: quartz, ser: sericite.

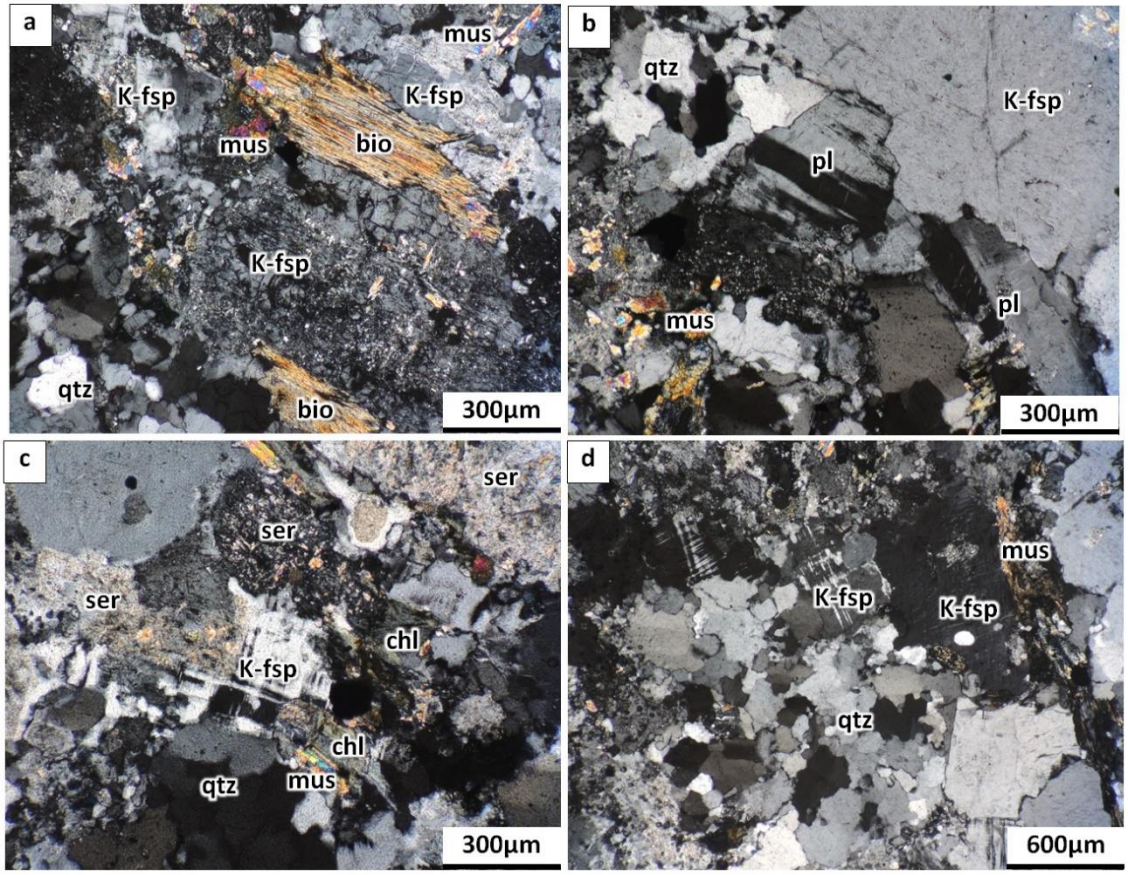

Figure 2.14: (a and b) Photomicrographs showing the major mineral compositions of two-mica granite; and (c and d) Photomicrographs showing the alteration feature of two-mica granite, consisting albite altered to K-feldspar, and K-felspar altered to sericite and chlorite. Abbreviation: bio: biotite, chl: chlorite, mus: muscovite, K-fsp: K-feldspar, pl: plagioclase, qtz: quartz, ser: sericite.

2.5.4 Intrusive rocks

Igneous intrusive rocks are not present at the deposit scale, only a small intrusion of granite was found in the southern part of the Vangtat shear zone, approximately 10 km south of the Vangtat deposit (Figure 2.3). This was identified during the regional scale mapping as a two-mica granite (Vilayhack *et al*., 2008). Microscopic observation identified the main compositions of this granite are quartz, plagioclase, K-feldspar, biotite, and muscovite (Figure 2.14a,b). Replacement textures and hydrothermal alteration features are commonly observed in the granite samples, involving (1) plagioclase altered to K-feldspar, and (2) K-feldspar and biotite altered to sericite and chlorite (Figure 2.14c,d).

2.5.5 Orebodies

The Vangtat orebodies mainly occur in the heavily sheared zone, most commonly hosted within pelitic schist. They rarely occur within slate or metasandstone. The dominant hosts of gold mineralization are quartz veins, in which gold is associated with sulfides, predominantly pyrite. A minor amount of gold-bearing pyrite is found in the graphite-carbonate rich zone which forms an envelope around the veins and grades into the less-altered pelitic schist (Figure 2.5, 2.6).

Veins and the alteration halo are commonly deformed and folded on account of sheared deformation and schistosity of host pelitic schist (Figure 2.5). Sheared structures and associated mineralization zone extended N-S striking parallel to the major Vangtat shear zone and regional metamorphic belt, subsequently, the zone was

cut by E-W and NE-SW faults (Figure 2.5) due possibly to the continuously of sheared deformation and/or regional metamorphism, resulting in discontinuously mineralized quartz veins.

2.6. DISCUSSION

2.6.1 Regional controls on localization of the Vangtat gold district

Mainland SE Asia is composed of several Gondwana-derived terranes including the Indochina, South China, and Sibumasu Terranes, which are assembled and amalgamated by subduction and collision orogenesis during late Palaeozoic-Mesozoic time (Bunopas, 1981; Charusiri *et al*., 2002; Metcalfe, 1999, 2011; Hutchison, 2014). The Indochina Terrane is a major tectonic unit and is made up of several tectonic domains, which are dominantly characterized by magmatic and metamorphic rocks, and associated with significant metallogenic belts in the region. The eastern extension of Indochina Terrane collided with the western margin of Kontum Massif, broadly marked by the Poko suture zone, and resulting in large-scale regional metamorphism and magmatism within an orogenic belt (Lepvrier *et al*., 2004, 2008).

The Poko suture zone and associated subsidiary structure, Vangtat shear zone marked the main host of a newly discovered Vangtat gold belt. The Poko suture zone represents a major crustal structure (Lepvrier *et al*., 2004; Nakano *et al*., 2007), although the ore deposits themselves are not directly hosted by this structure; rather by subsidiary structures, such as the Vangtat shear zone. This model is consistent with other orogenic gold deposits in the metamorphic belt around the world (Groves *et al*., 1998; Kerrich *et al*., 2000; Goldfarb *et al*., 2001; Groves *et al*., 2003).

2.6.2. Host lithology

Pelitic schist is the main host to the mineralized corridor present within the heavily sheared zone of the Vangtat deposit. Pelitic schist is made up of foliated muscovite-chlorite with finely interlayered quartz and plagioclase. This major metamorphic mineral assemblage is consistent with the temperature estimated by Raman spectroscopical analyses of graphite (350-410 ºC) and is indicative of greenschist facies metamorphic conditions. This regional metamorphic unit is compatible with the low-grade metamorphism of the Kham Duc complex in the Kontum Massif, which was metamorphosed during the Indosinian tectonic event (270-230 Ma; Osanai *et al*., 2008).

Greenschist facies metamorphism is present in a majority of orogenic gold deposits globally (Kerrich *et al*., 2000; Goldfarb *et al*., 2005). Although the details of the gold-greenschist-grade association remain uncertain, Goldfarb *et al*. (2005) proposed this association to the result of: (1) A large fluid volume which is created during the amphibolite and/or greenschist transition and is released into the greenschist zone, (2) A structurally favorable zone lies just above this transition, and (3) Fluid focusing and phase separation are most likely to occur as fluids ascend into the greenschist facies pressure-temperature regime. This model for orogenic gold deposit in greenschist facies metamorphic terranes is compatible with the characteristics of the Vangtat gold deposit.

2.7. SUMMARY

- The Poko suture zone marked the collision orogenesis in the western margin of Kontum Massif. The Vangtat shear zone is one of the subsidiary structures associated with the Poko suture zone and represented the main host for a newly discovered Vangtat gold belt.
- Gold mineralization in the Vangtat deposits is hosted in the regional metamorphic belt, greenschist facies, and is controlled by parallel N-S trending shear structure within the Vangtat shear zone. The orebodies are composed of high-grade gold bearing quartz-sulfide vein and graphite-carbonate alteration envelope containing lower-grade gold.
- The hosted geological features of the Vangtat gold deposits, such as regional tectonic regime, mineralized host rock, and structural setting are similar to typical orogenic gold deposits globally. Since alluvial gold is widely distributed in the region, it is inferred that there is great potential for discoveries of the new orogenic gold deposits in the Vangtat shear zone, the southeastern region of Laos.

CHAPTER 3 MINERALOGY AND PARAGENESIS

3.1. INTRODUCTION

This chapter documents the mineralization characteristics of the Vangtat deposit, emphasizing the nature of gold mineralization style, including vein emplacement, hydrothermal alteration, ore mineralogy, and paragenetic relationships of gold mineralization events. The description is principally investigated based on textural and spatial relationships (e.g. cross-cutting, overprinting, replacement, and overlapping zonation). The texture of hand specimen samples and drill core samples were observed and carefully recorded and interpreted. Microscopic observations and scanning electron microscope (SEM) analyses were also applied to identify ore and hydrothermal gangue minerals.

3.2. MINERALIZATION AND PARAGENESIS

The Vangtat gold mineralization is closely associated with shearing structures, which affected a pelitic schist host unit and created permeable zones for hydrothermal activity and associated gold deposition. Therefore, the formation of a shear zone and hydrothermal activity are key processes associated with gold deposition in the Vangtat deposit. Quartz veins mark the core of the shear zone and represent the center of the hydrothermal fluid conduits. Hydrothermal fluid ascended within this permeable zone, within part contemporaneous shearing, hydrothermal alteration and vein formation.

Hydrothermal alteration and/or replacement extended laterally perpendicular to the quartz veins. Vertical zonation reflects the different types of wall rock host lithologies from the lower portion to the upper portion.

The presence of sulfide, which is predominantly pyrite, indicates the mineralized rocks in the Vangtat deposit. Pyrite is widely distributed throughout the shear zone, a trace amount of disseminated pyrite is found in unmineralized pelitic schist unit away from the shear zone. The quantity of pyrite increases towards the center of hydrothermal activity (i.e. the quartz veins) and reflects increased precipitation of hydrothermal pyrite. Within the progressive and/or dominant hydrothermal alteration, graphite-carbonate-quartz-pyrite became more a pervasive alteration of the host pelitic schist unit, broadly marking the alteration halo that surrounds the gold-bearing veins. Quartz veining with abundant pyrite corresponds to high grade gold mineralization and it occurs within an envelope of graphite-carbonate-quartz alteration.

The paragenetic sequence of gold mineralization in the Vangtat deposit is: (1) A shear structure formed within the host pelitic schist and marks the favorable site for the deposition, (2) a graphite-carbonate-quartz alteration envelope forms in the early stages of mineralization, and (3) Quartz-pyrite veins represent the main gold mineralization stage.

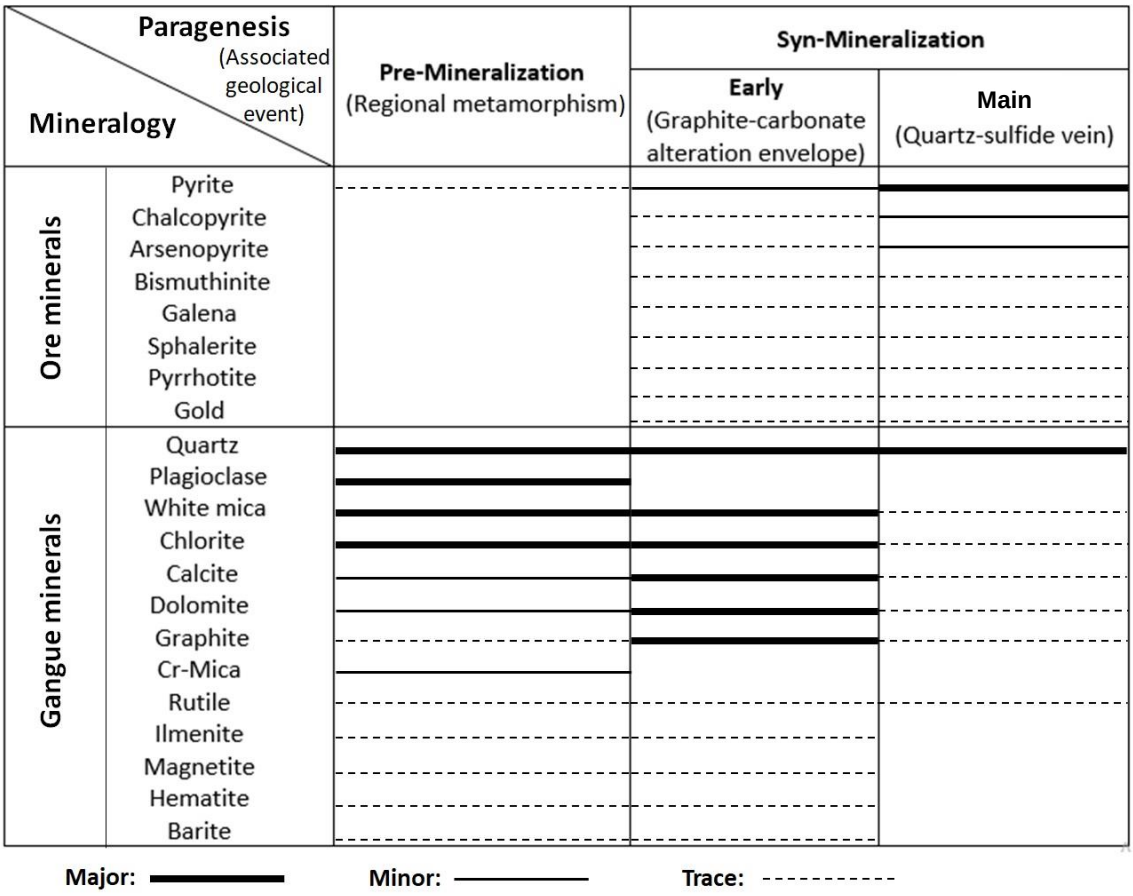

Figure 3.1: Mineralization and paragenesis of the Vangtat gold deposit

3.3. HYDROTHERMAL ALTERATION

Hydrothermal alteration of the wall rock at Vangtat was mainly associated with the shear zone and extended laterally for tens to hundreds of meters beyond the ore-grade rock. The alteration assemblages reflect the different types of wall rock lithology, metagabbro in the lower portion and pelitic schist in the upper portion. The most prominent feature of the hydrothermal alteration which accompanies gold mineralization is marked by the graphite-carbonate zone which occurs as an alteration halo surrounding the quartz-pyrite veins.

3.3.1 Hydrothermally altered metagabbro

Actinolite, tremolite, epidote, and plagioclase are the major components of the metagabbro (Chapter 2.5.1), the presence or absence of this mineral assemblage reflects the alteration of the metagabbro. The description of hydrothermally altered metagabbro is investigated in the deeper part of the drill hole VADH017 that intersected the formation of metagabbro and overprinted hydrothermal alteration (Figure 2.6; Chapter 2).

Partially altered metagabbro is found in the bottom of drill hole VADH017 (from 190 m downward) and is characterized by randomly oriented aggregates of chlorite and calcite replacing actinolite in its crystal margins (Figure 3.2a). Moving upward (up to 150 m depth), close to the core of the shear zone, which is marked by pelitic schist and mineralized vein, the metagabbro is completely altered. The mineral assemblages change to chlorite, calcite, dolomite, quartz, talc, and muscovite (Figure

3.2b). These alteration mineral products in the metagabbro have been locally mobile within the rocks during alteration, resulting in the modification of original rock texture (Figure 3.2b). No gold or sulfide is observed in the hydrothermally altered metagabbro.

3.3.2 Hydrothermally altered pelitic schist

The pelitic schist occupies the center of the shear zone and is commonly hydrothermally altered. The alteration minerals in the pelitic schist are for the most part the same major silicate minerals present in the metamorphosed rock (i.e. quartz, plagioclase, muscovite, and chlorite). When hydrothermally altered, the pelitic schist shows minor but noticeable amounts of pyrite, titanite, rutile, ilmenite, hematite, magnetite, and barite. Consequently, the hydrothermal alteration feature of pelitic schist is very subtle and difficult to distinguish in hand specimens and outcrops, and generally cryptic at the microscopic scale.

The evidence of hydrothermally altered pelitic schist consists of: (1) Muscovite replaced in the margin and micro fissure crystals of plagioclase (i.e. albite; Figure 3.3a), this muscovite formation is randomly oriented and not foliated, which differentiates it from metamorphic muscovite which is the major mineral in pelitic schist, and (2) The presence of chromium-mica (fuchsite), which developed along the lineation texture of muscovite (Figure 3.3b). Moreover, the increase in the amount of pyrite in the pelitic schist (Figure 3.3c,d) also marks the most intensely altered part of the rock. However, pyrite is also an accessory mineral in unaltered host pelitic schist, and the differentiation between diagenetic and/or metamorphic pyrite and hydrothermal pyrite is subtle in the margin of the alteration zone.

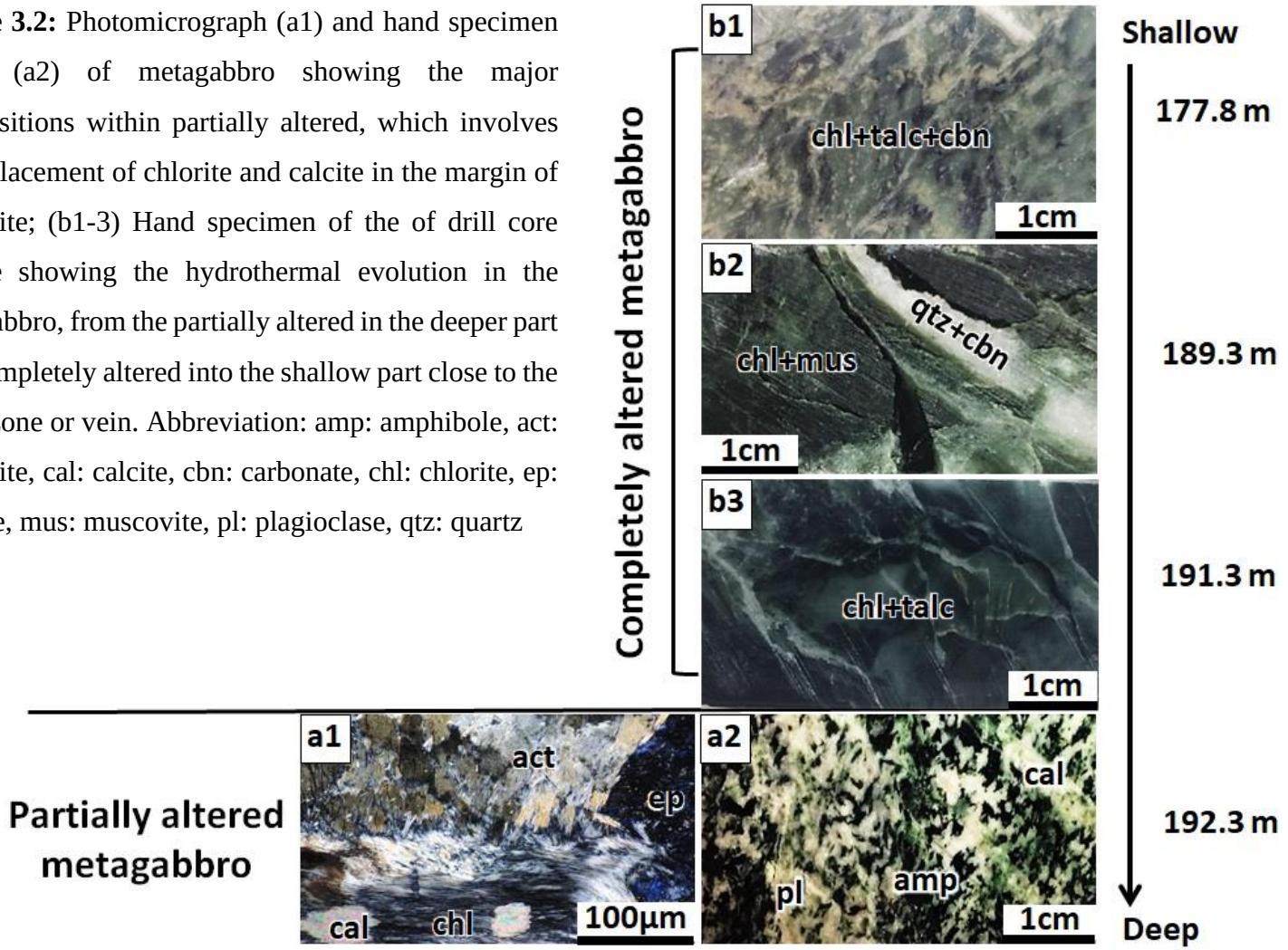

Figure 3.2: Photomicrograph (a1) and hand specimen photo (a2) of metagabbro showing the major compositions within partially altered, which involves the replacement of chlorite and calcite in the margin of actinolite; (b1-3) Hand specimen of the of drill core sample showing the hydrothermal evolution in the metagabbro, from the partially altered in the deeper part and completely altered into the shallow part close to the shear zone or vein. Abbreviation: amp: amphibole, act: actinolite, cal: calcite, cbn: carbonate, chl: chlorite, ep: epidote, mus: muscovite, pl: plagioclase, qtz: quartz

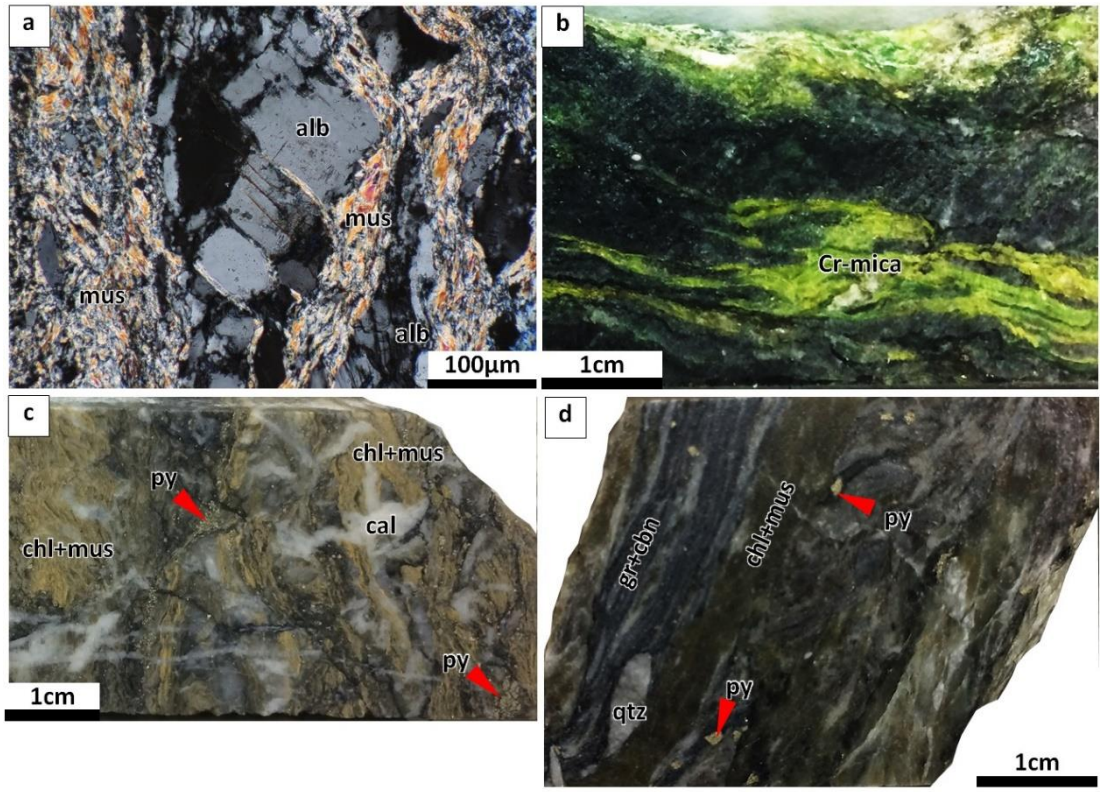

Figure 3.3: (a) Photomicrograph showing muscovite replaced in the margin and micro fissure crystal of albite (b) Hand specimen photo showing the precipitation of Cr-mica in the lineation of muscovite in the pelitic schist; and (c and d) Hand specimen photos showing the dissemination of pyrite in the pelitic schist. Abbreviation: alb: albite, cal: calcite, cbn: carbonate, chl: chlorite, mus: muscovite, py: pyrite, qtz: quartz

3.3.3 Graphite-carbonate alteration envelope

Graphite, calcite, dolomite, quartz, and pyrite are the major components in the ore zone, a minor amount of arsenopyrite and chalcopyrite are also found accompanying pyrite. This mineral assemblage locally overprints the foliated chlorite-muscovite metamorphic assemblage of the pelitic schist (Figure 3.4e) and marks a prominent feature of the hydrothermal alteration envelope that surrounds the quartz veins (Figure 3.4a). The presence of pyrite in the graphite-carbonate alteration envelope accompanies low-grade (avg. <1 g/t) gold ore. The dominance of graphite in the zone possibly involves the transformation of graphite during regional metamorphism (Chapter 2.5.2), plus additional hydrothermal graphite that occurs in cross-cutting structures, predominantly microshears (Figure 3.4c,d). These two graphite formations are possibly linked, as the hydrothermal graphite was derived from the primary carbonaceous material by hydrothermal remobilization of carbon. Porphyroblastic pyrite and quartz-carbonate fragments and/or porphyroblasts are commonly observed in the graphite-carbonate alteration envelope, which elongated and aggregated subparallel to the pelitic schist foliation (Figure 3.4b).

3.3.4 Vein emplacement

Discrete veins and/or silicified rock likely superimposed graphite-carbonate alteration envelope (Figure 3.4a, 3.5a). Individual veins have a thickness of 10 cm and up to 3 m. Veins commonly form an ore zone that extends for over 3 km in length and ~200 m in width (Figure 2.6; Chapter 2). Veins are mainly composed of quartz and pyrite,

with minor amounts of graphite, calcite, dolomite, white mica, chlorite, chalcopyrite, and arsenopyrite. Pyrite in the veins may reach up to 60 vol% and endowed with high-grade gold, with average grades >3 g/t Au and >90 g/t Au in selected hand specimen and drill core intercepts; Figure 3.4a). Vein zones include several fractures that are filled by quartz, calcite and graphite (Figure 3.5c). Fragments of quartz vein are brecciated and cemented with pyrite in the silicified zone, and boudinaged within the shear zone (Figure 3.5 d-f).

3.4. ORE MINERALOGY

Pyrite is the most common sulfide mineral in the Vangtat deposit. It commonly forms in association with gold mineralization. The presence and abundance of pyrite is an important indicator of the most gold mineralized rock in the Vangtat deposit. As a general rule, pyrite content decreases together with gold concentration, from the quartz-sulfide vein zone at the center of the Vangtat shear zone toward the altered host rocks in the margins. Chalcopyrite and arsenopyrite are likely precipitated together with pyrite and have a more restricted distribution than pyrite. They are typically found in the most intensely altered part of the shear zone, particularly the quartz veins. Other sulfide minerals present as accessory minerals are sphalerite, galena, bismuthinite, and pyrrhotite, most often as inclusion in pyrite.

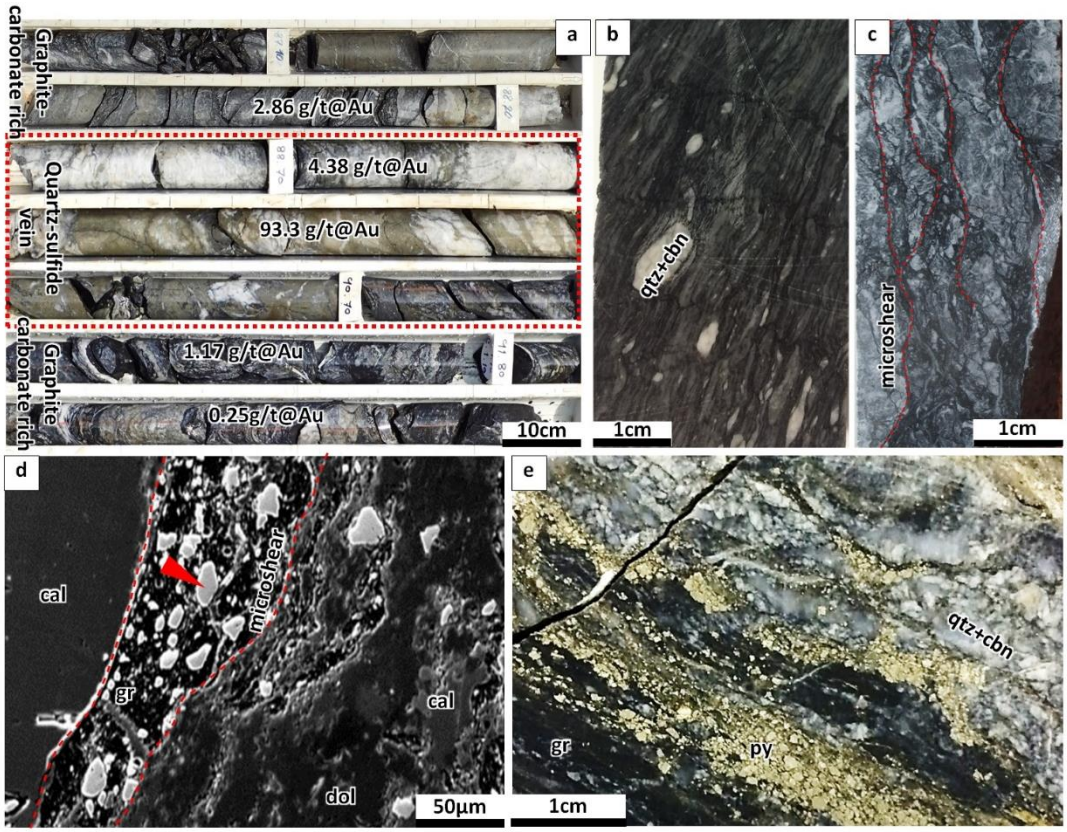

Figure 3.4: (a) Drill core photo showing the typical occurrence of graphite-carbonate rich zone surrounded quartz-sulfide vein; (b) Hand specimen photo showing the dominant of graphite (dark color) in the foliation texture of pelitic schist; (c) Dashed red lines represent the microshear which dominated by graphite (dark color and fine-grained pyrite), within the closed up of backscatter image of SEM (d); (e) Graphite-quartz-carbonate-pyrite assemblage dominated in the pelitic schist. Abbreviation: cal: calcite, cbn: carbonate, chl: chlorite, dol: dolomite, gr: graphite, mus: muscovite, py: pyrite, qtz: quartz

3.4.1 Pyrite

Pyrite is commonly observed in the Vangtat deposit, including altered pelitic schist, graphite-carbonate alteration envelope, and veins. Pyrite in the vein and alteration envelope is composed of various grain sizes, most likely coarse-grained, from 300 μm up to a few centimeters. The finer pyrite (<500 μm) commonly has a euhedral shape, while the coarser crystals are anhedral to subhedral (Figure 3.6a,b,e). Disseminated pyrite in the altered pelitic schist is relatively finer-grained, generally ranges from a few tens microns up to a few hundreds of microns, and typically has a euhedral shape. The pyrite dissemination in the host pelitic schist is occasionally associated with pressure shadow within the metamorphic foliation.

The detailed microscopic observation indicated that pyrites are uniformly crystallized within a homogeneous texture, rarely observed the zoning texture, only a few grains of pyrite in the vein displayed an overgrowth texture with a core and rim parts are porous and compact, respectively (Figure 3.6f). The crystallization and textural of pyrite relatively contained other sulfide inclusions as well as gold particle grains.

3.4.2 Chalcopyrite

Chalcopyrite is found in the most intense alteration and mineralization zones, particularly in the quartz-sulfide veins. Chalcopyrite is not observed in the host pelitic schist. Chalcopyrite is likely formed together with pyrite, most commonly occurs along the crystal boundaries and/or fractured crystals of pyrite, and cemented and/or

brecciated with pyrite fragments (Figure 3.6d-f, 3.7d), as well as inclusions in pyrite (Figure 3.7e,g). Chalcopyrite has an anhedral to subhedral shape and is rarely observed in hand specimen; it is generally found under the microscope, with the grain size ranging between tens of microns and up to a few hundreds of microns.

3.4.3 Arsenopyrite

Arsenopyrite is intimately related to pyrite (Figure 3.7a,b) and the abundance of arsenopyrite consistently corresponds to the presence of pyrite, most commonly in the quartz-sulfide vein. Arsenopyrite mainly appears as inclusions in pyrite (Figure 3.6c, 3.7f) and is commonly observed under the microscope, rarely recognized in the hand specimen samples. The crystals of arsenopyrite compose a wide range of sizes from tens of microns up to a few hundreds of microns and anhedral to euhedral shape.

3.4.4 Other sulfides

Other sulfide minerals such as sphalerite, galena, bismuthinite, and pyrrhotite are present as small particle grains with an average grain size of ~30 μm of anhedral shape, most likely occurred as inclusion in pyrite and could be found under the microscope only. Amongst these, sphalerite is more dominant, especially in the western orebody (Figure 3.7b,c). The presence of sphalerite is closely associated with pyrite and also with chalcopyrite (Figure 3.7b,d), including blebs of chalcopyrite concentrated around the periphery of sphalerite and randomly disseminated in the sphalerite crystal (Figure 3.7c), which indicates as exsolution texture.

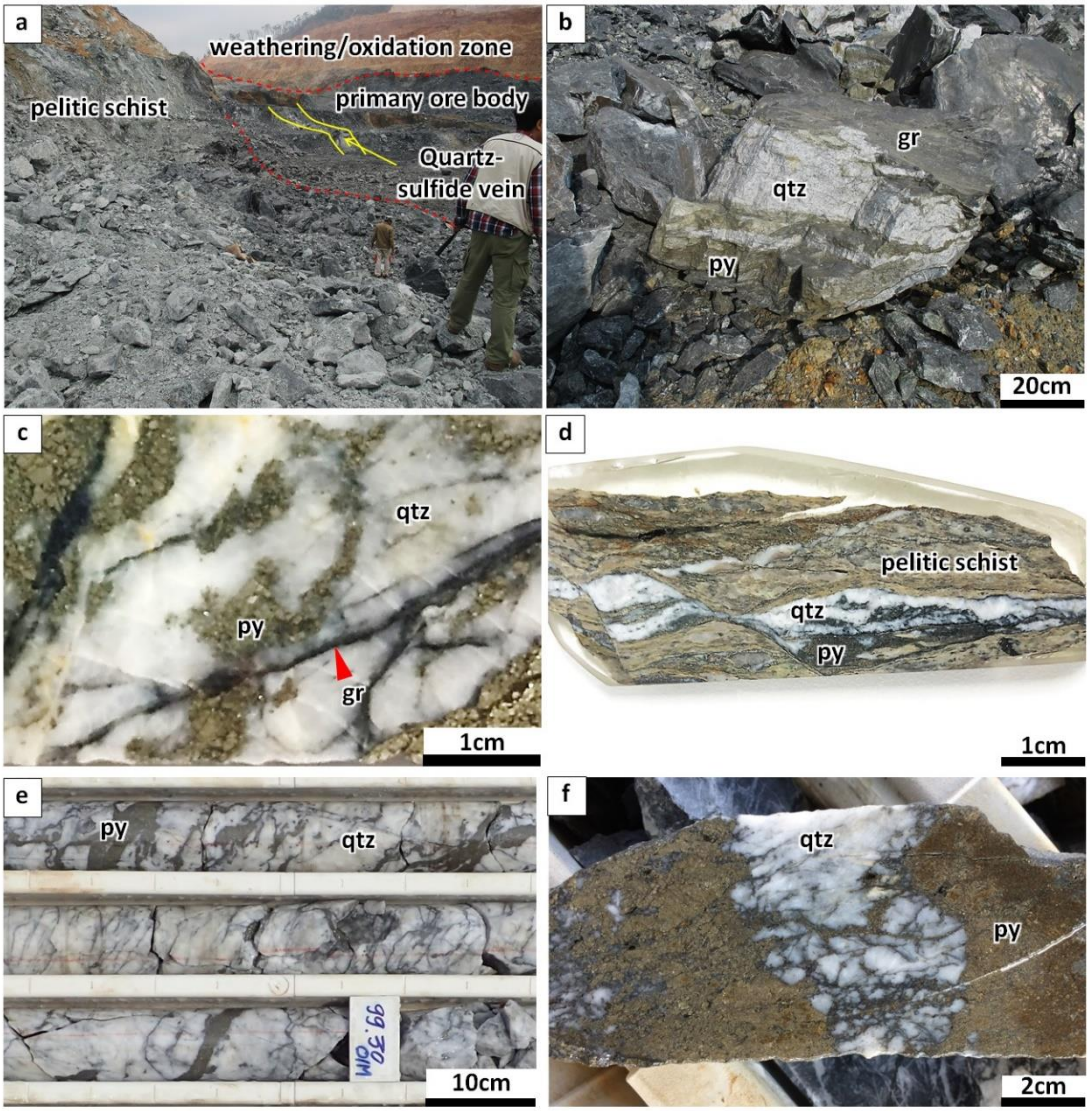

Figure 3.5: (a) The ground view of open-pit mine showing the primary ore zone with the graphite dominant (dark color) and was overlapped by vein zone, which is mainly composed of quartz and pyrite that showed in the close-up photo (b); (c) Hand specimen photo showing the quartz-sulfide vein was filled by graphite; (d) Hand specimen photo showing the boudinage of quartz-sulfide vein precipitated in the heavily sheared pelitic schist; and (e and f) Hand specimen photos showing the fragments of quartz in the vein are cemented and brecciated with pyrite. Abbreviation: gr: graphite, py: pyrite, qtz: quartz

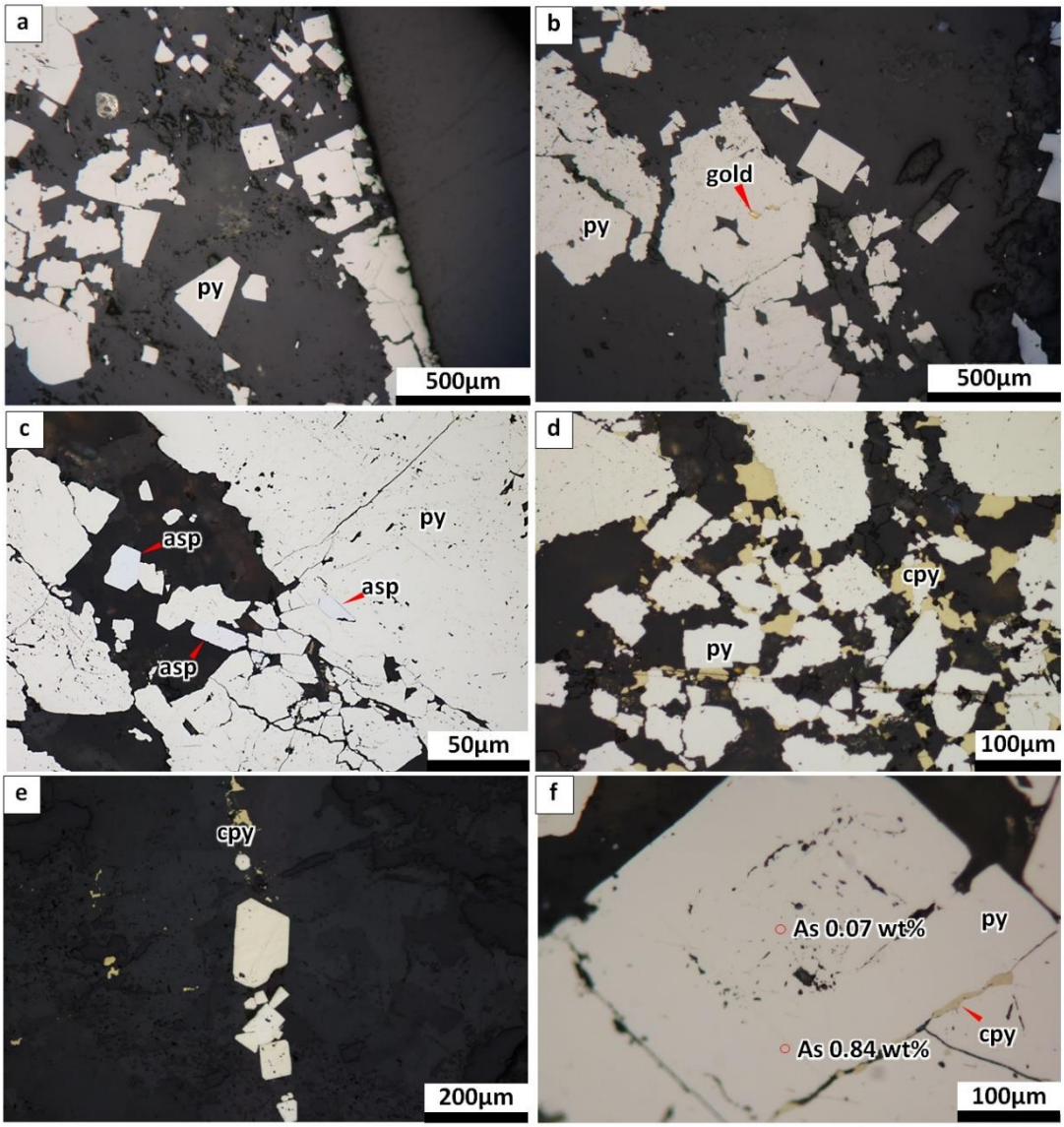

Figure 3.6: Photomicrographs showing the typical occurrence of pyrite, consisting of various grain size from anhedral to euhedral crystal. The finer-grained (< 500 µm) showed an euhedral shape, while the coarser-graineds are anhedral to subhedral (a, b and e), these pyrite accompanying with arsenopyrite (c) and chalcopyrite (d); and (f) The intergrowth texture of pyrite in the vein. Abbreviation: asp: arsenopyrite; cpy: chalcopyrite; py: pyrite.

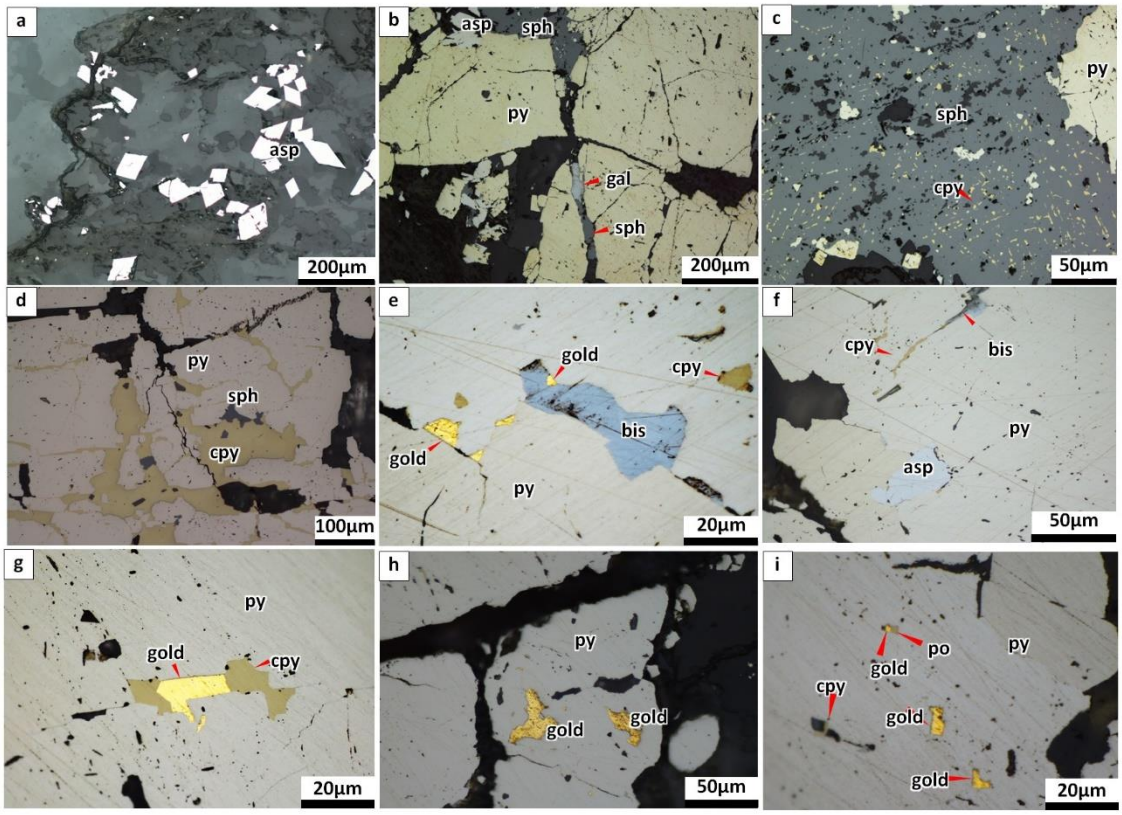

Figure 3.7: Photomicrographs showing the typical occurrence of sulfide minerals and associated with gold. (a) Arsenopyrite crystals distributed in the quartz-sulfide vein; (b) The occurrence of arsenopyrite incorporated with pyrite as well as sphalerite and galena occur along the crystal boundaries of pyrite; (c) More dominant of sphalerite in the western Vangtat deposit occurs with pyrite, and the exsolution texture of sphalerite; (d) Chalcopyrite and sphalerite occur incorporated with pyrite; (e) Gold occurs along the crystal boundaries of pyrite and as inclusion with bismuthinite and chalcopyrite; (f) Chalcopyrite, bismuthinite and arsenopyrite inclusion in pyrite; (g) Gold and chalcopyrite inclusion in pyrite; and (i) Gold, chalcopyrite, and pyrrhotite inclusion in pyrite. Abbreviation: asp: arsenopyrite; cpy: bis: bismuthinite, chalcopyrite; gal: galena; po: pyrrhotite; py: pyrite; sph: sphalerite.

3.4.5 Gold

Gold in the Vangtat deposit is typically observed as visible gold, which commonly occurs as particle grains together with sulfides, mainly pyrite. Free-gold is not observed in the mineralization zone. Free gold is present in the supergene horizon and was the source of surficial and alluvial mining that brought attention to the primary ore deposits.

The gold grade in the mineralized rock can be approximated based on the amount of pyrite within the graphite-carbonate alteration envelope to the quartz-sulfide vein (Figure 3.4a). This is interpreted that as gold enrichment occurring during the pyrite replacement reaction and crystallization through the mineralized rocks in the Vangtat deposit.

Gold particle grains are commonly observed under the microscope and difficult to recognize in hand specimen samples. Most gold particle grains occur as anhedral shape inclusions in sulfide, especially pyrite (Figure 3.7h,i), but also together with chalcopyrite and bismuthinite (Figure 3.7e,g), and is occasionally present in the fractures as a coating of sulfides and the matrix of fractures sulfide (Figure. 3.7e).

3.5. DISCUSSION

Gold deposition in the Vangtat deposit is related to the evolution of the deformation structure that runs through the Vangtat shear zone and is mainly hosted by the pelitic schist. The orebodies show a direct relationship to the combination of favorable shear structure and host rock lithology “ore trap”, which represents the site of ore deposition.

The development of and repetitive tectonic activity along the shear structure would create increased permeability for hydrothermal fluid to transport ore and alteration mineral constituents. The quartz veins mark the center of hydrothermal activity and represent the fluid pathways.

Hydrothermal alteration and fluid-rock interaction expanded laterally outwards of the main fluid conduits, the quartz veins. The innermost alteration is marked by a graphite-carbonate-quartz alteration envelope. This extends laterally to the adjacent wall rock consisting of pelitic schist and/or metagabbro. In addition, the mineralogy of alteration assemblages associated with the evolution of fluid transected two lithologies (e.g. metagabbro in the lower portion and pelitic schist in the upper portion) of contrasting composition have provided a verticle zonation and variety of alteration assemblages, reflecting equilibrium and disequilibrium of fluid-wall rocks interaction reaction.

3.5.1 Variation in alteration assemblages and mineral paragenesis

Hydrothermal alteration features and assemblages are described based on the rock units and the distance away from the veins; an approach that emphasizes fluid-wall rock interaction without an assumption on the fluid source.

Fluid-rock interaction within metagabbro in the lower portion is characterized by H_2O-CO_2 bearing fluid reacted with the mafic minerals (e.g. actinolite, tremolite) components of metagabbro (Eq. 2, 3). The presence of chlorite and carbonate as alteration products represent the hydrothermal evolution that occurred in the greenschist facies environment (Groves, 1993).

(Eq. 2)

$$6\ Ca_2Fe_5Si_8O_{22}(OH)_2 + 12\ CO_2 + 14\ H_2O = 5\ Fe_6Si_4O_{10}(OH)_8 + 12\ CaCO_3 + 28\ SiO_2$$

(Actinolite) (Fluid) (Chlorite) (Calcite) (Quartz)

(Eq. 3)

$$Ca_2(MgFe)_5Si_8O_{22}(OH)_2 + 4\ CO_2 = Mg_3Si_4O_{10}(OH)_2 + 2\ CaMgCO_3 + 4\ SiO_2$$

(Tremolite) (Fluid) (Talc) (Dolomite) (Quartz)

Hydrothermally altered pelitic schist broadly marked the site of gold deposition, where the vein zones overlapped. The alteration feature is not prominent or evident, since the hydrothermal alteration involved most of the same major silicates of the unaltered rock; in other words, the fluid was generally in equilibrium with the host pelitic schist (e.g. greenschist facies metamorphic rocks; Goldfrab *et al*., 2005). The most altered part of the pelitic schist is characterized by albite altered to muscovite (Eq. 4), reflecting cation exchange during the fluid-rock interaction, which indicates that fluid was weakly alkaline to near-neutral.

(Eq. 4)

$$3\ NaAlSi_3O_8 + K^+ + 2H^+ = KAl_3Si_3O_{10}(OH)_2 + 3Na^+ + 6\ SiO_2$$

(Albite) (Fluid) (Muscovite) (Quartz)

The development of a chromium-mica along the lineation texture of muscovite is a recognizable feature of altered pelitic schist; chromium being possibly derived from the mafic-ultramafic rocks in the lower portion during the metamorphic-hydrothermal evolution. Wang *et al.* (2020) identified that mafic igneous rocks in southeastern Laos, which form the lower portion of the Vangtat deposit have a high chromium content.

The abundance of graphite in the alteration envelope may suggest the mixing of two different fluids carbon dioxide + water and methane + water (e.g. Holloway, 1984; Craw, 2002), combined with the evidence from fluid inclusion study (Chapter 4), which indicated the presence of CO_2 and CH_4 in the ore-forming fluids. Furthermore, the dominance of graphite in the host rock and alteration envelope would create a favorable site for gold precipitation, reflecting the facilitation of gold extraction and wall rock sulfidation involve the reductive reaction of the carbon-bearing host rock (Poulsen *et al*., 1986; Cox *et al*., 1991; Ridley, 1993; Phillips and Powell, 2010).

3.5.2 Wall rock-sulfidation and gold precipitation

The deposition of gold in the Vangtat deposit is primarily related to the precipitation of sulfide, predominantly pyrite, in which gold principally occurred as particle grains inclusion in pyrite. Hydrothermal fluid responsible for gold mineralization in the Vangtat deposit deduced from fluid-wall rocks interaction reaction through the transected fluid path, indicated that fluid had a relatively high CO_2 content (Eq 2, 3), nearly-neutral to slightly alkaline condition (see Chapter 3.5.1), and fluid generally reduced in contact with graphite bearing host rock. Experimental studies by Sward (1973) and Hayashi and Ohtomo (1991) indicate that gold is most soluble as sulfide complexes in alkaline and reducing solutions. This observation combined with the occurrence of gold in the Vangtat deposit suggests that gold was carried as a sulfide complex in the ore-fluids.

The precipitation of gold is related to both (1) The destabilization of sulfide complex by sulfidation reaction, which involves the interaction of Fe-bearing mineral (e.g. chlorite) in the host rock and S-bearing fluid (Eq. 5; Pillips and Groves, 1984; Phillips and Powell, 2010), and (2) Physical-chemical gradients of the ore-forming fluid, which relates to the reductive reaction with the carbonaceous material or graphite dominant in the host rock (Poulsen *et al*., 1986; Cox *et al*., 1991).

$$Fe^{2+} + 2\ Au(HS)_2 + 2\ H_2 = FeS_2 + Au^0 + 2\ H_2O \qquad \text{(Eq. 5)}$$

(Fe-mineral) (Ore fluid) (Pyrite and gold deposition in rock)

This process assumes that sulfur is transported in the ore fluid along with gold in a soluble sulfide complex.

The vertical zonation of alteration mineral assemblages may involve a local temperature decrease, however, temperature decrease alone was not probably a determining factor for gold precipitation in the Vangtat deposit. Because the stability constant of gold-bearing sulfide complexes changes very little with temperature over 150-350 ºC range (Seward, 1973; Hayashi and Ohtomo, 1991), therefore the decrease of temperature alone is unlikely to be the main mechanism for the precipitation of gold from sulfide complexes.

3.6. SUMMARY

- The co-evolution of shear structure and hydrothermal activity intersected pelitic schist marked the favorable site for gold deposition in the Vangtat deposit.

- Gold is closely associated with sulfide, most commonly occurring as particle inclusions in sulfide, predominantly pyrite. Gold is carried as a sulfide complex along with the ore fluid, and gold precipitation was associated with wall rock sulfidation. The significant presence of graphite in the host rock would facilitate gold precipitation through a reduction reaction.
- The hydrothermal fluid responsible for gold mineralization is characterized by a high CO_2 content, near-neutral to slightly alkaline fluid composition as evidenced by the fluid interaction with mafic minerals in the lower portion and the presence of muscovite replaced albite in the altered host mineralized rock.

CHAPTER 4 MINERAL CHEMISTRY, FLUID INCLUSION, AND SULFUR ISOTOPE STUDIES

4.1. SULFIDE CHEMISTRY

Gold mineralization in the Vangtat deposit is intimately related to sulfide minerals, predominantly pyrite (Chapter 3.4.5). Significant auriferous sulfide is likely associated with hydrothermal activity throughout the history of the shear zone development, most commonly expressed on quartz veins. Therefore, the investigation of sulfide mineral chemistry would implicate the understanding of the ore depositional environment and also plays a significant role in mineral exploration and targeting the main ore zone.

4.1.1 Pyrite chemistry

Pyrite is one of the most common minerals in hydrothermal ore deposits and is stable under various physical-chemical fluid conditions. It is also a refractory mineral with respect to post-depositional metamorphism (Agangi *et al*., 2013; Deditius *et al*., 2014; Keith *et al*., 2014). Pyrite is a dominant sulfide mineral and marked the main host for gold mineralization in the Vangtat deposit. In many hydrothermal ore deposits where pyrite is the dominant sulfide phase, it can represent a major repository for many trace metals including Co, Ni, Cu, As, Se, Mo, Ag, Sb, Te, Pb, Bi, and Au (e.g. Large et al., 2009), therefore, it suitable for micro-analytical studies to reconstruct ore-forming

processes. The chemical composition of pyrite may also inform the understanding of ore genesis.

Preliminary analysis by electron microprobe identified the chemical composition of pyrite in the Vangtat deposit as similar to the stoichiometric composition, consisting of Fe and S contents range from 32.71 to 33.04 atom% and 66.62 to 67.46 atom%, respectively (Table 4.1). Arsenic content in pyrite is relatively low (up to 0.84 wt%), the different concentration of As in pyrite is observed in the overgrowth texture; the inner has 0.07 wt% As and outer part has 0.84 wt% As (Figure 3.6f; Chapter 3). Other minor and trace elements, including gold in solid solution in pyrite, are not detected in microprobe analysis.

4.1.2 Arsenopyrite chemistry and geothermometry

Arsenopyrite mainly presents in the vein, most likely incorporates with pyrite (Chapter 3.4.3). Electron microprobe analysis identified As content in arsenopyrite ranging from 30.73 to 31.55 atom% (33.00 atom% is the stoichiometric value), S and Fe contents range from 34.59 to 35.77 atom% and 33.50 to 33.95 atm%, respectively (Table 4.1). Arsenopyrite has the Fe/S ratio ranging from 0.94 to 0.98 and Fe/(S+As) ~ 0.51, indicating that arsenopyrite in the Vangtat deposit has relatively low As content. There is an obvious negative correlation between As and S and a slightly positive correlation between As and Fe (Figure 4.1).

Table 4.1: Representative major chemical composition of pyrite, arsenopyrite, and gold in the Vangtat deposit

Sample	Pyrite				Arsenopyrite						Gold			
	Atomic %				Atomic %						Atomic %			
	As	**Fe**	**S**	**Total**	**As**	**Fe**	**S**	**Total**	**Fe/S**	**Fe/(S+As)**	**Ag**	**Au**	**Total**	**Au/Ag**
VADH016-137.3														
1	0.00	32.54	67.46	100.00										
2	0.00	32.94	67.06	100.00										
3	0.00	32.85	67.15	100.00										
4	0.00	32.86	67.14	100.00										
5	0.00	33.04	66.96	100.00										
VADH051-125.2														
1	0.17	32.94	66.89	100.00										
2	0.16	32.95	66.89	100.00										
3	0.22	32.88	66.89	100.00										
4	0.11	32.91	66.89	99.92										
5	0.32	32.96	66.89	100.18										
VADH018-145.5														
1	0.30	32.76	66.94	100.00	31.14	33.71	35.14	100.00	0.96	0.51	8.6	91.4	100.0	11
2	0.13	32.85	67.02	100.00	31.30	33.91	34.79	100.00	0.97	0.51	8.7	91.3	100.0	10
3	0.27	32.98	66.75	100.00	31.05	33.91	35.04	100.00	0.97	0.51	8.9	91.1	100.0	10
4	0.24	32.84	66.92	100.00	31.17	33.79	35.04	100.00	0.96	0.51	6.3	93.7	100.0	15
5	0.00	32.90	67.10	100.00	30.74	33.81	35.46	100.00	0.95	0.51	4.9	95.1	100.0	20

Table 4.1: (Continue)

Sample	Pyrite				Arsenopyrite						Gold			
	Atomic %				Atomic %						Atomic %			
	As	**Fe**	**S**	**Total**	**As**	**Fe**	**S**	**Total**	**Fe/S**	**Fe/(S+As)**	**Ag**	**Au**	**Total**	**Au/Ag**
VADH017-90.7														
1	0.04	32.71	67.25	100.00	30.83	33.61	35.57	100.00	0.94	0.51	14.7	85.3	100.0	6
2	0.45	32.93	66.62	100.00	31.09	33.74	35.17	100.00	0.96	0.51	11.4	88.6	100.0	8
3	0.08	32.89	67.03	100.00	31.55	33.85	34.59	100.00	0.98	0.51	13.1	86.9	100.0	7
4	0.26	32.94	66.81	100.00	30.73	33.50	35.77	100.00	0.94	0.50	9.3	90.7	100.0	10
5	0.36	32.84	66.81	100.00	30.88	33.95	35.17	100.00	0.97	0.51	20.5	79.5	100.0	4
VADH017-98.0														
1	0.00	32.83	67.17	100.00							18.8	81.2	100.0	4
2	0.32	32.96	66.72	100.00							21.6	78.4	100.0	4
3	0.00	32.88	67.12	100.00							18.5	81.5	100.0	4
4	0.00	32.98	67.02	100.00							4.0	96.0	100.0	24
5	0.01	32.83	67.16	100.00							13.3	86.7	100.0	7

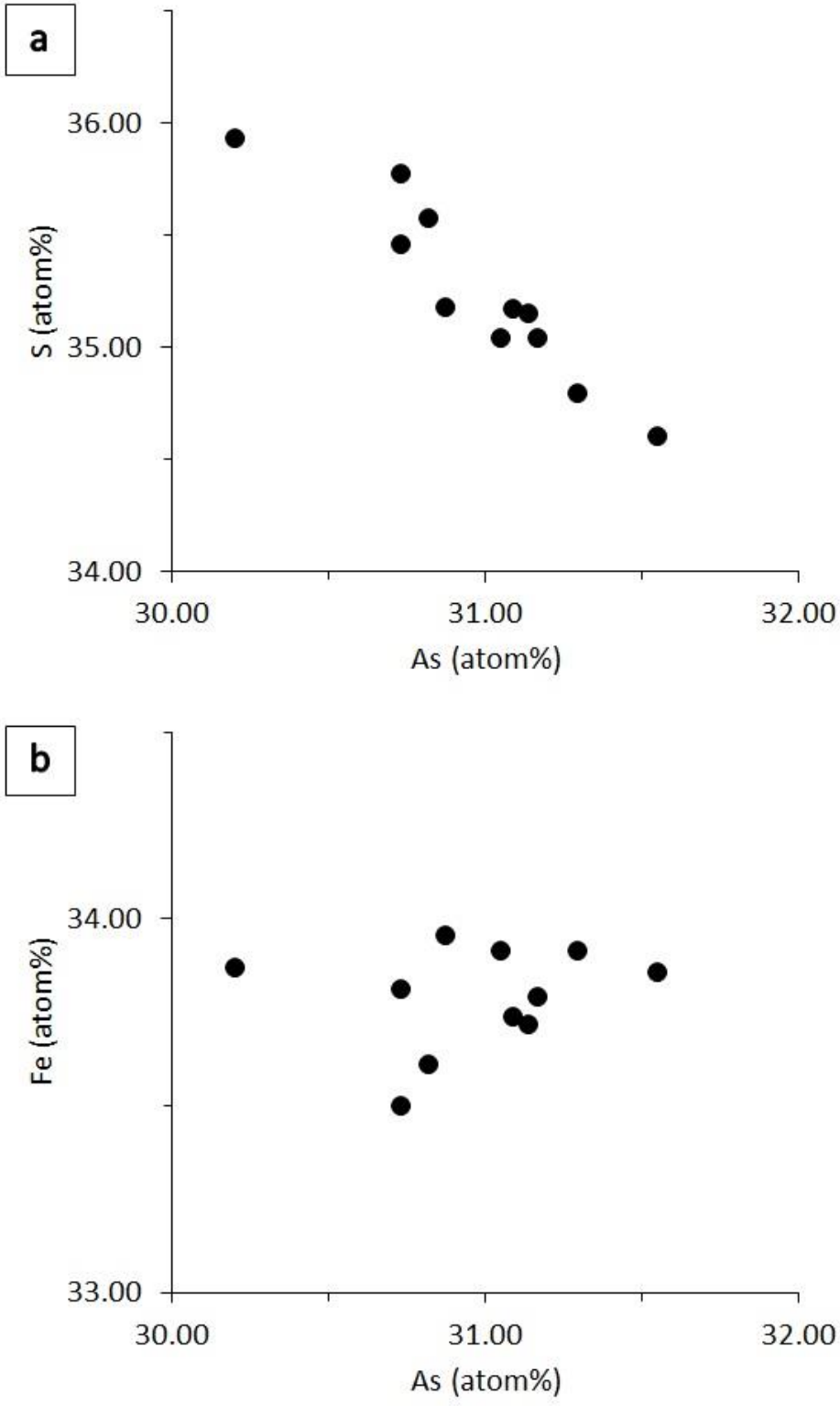

Figure 4.1: The correlation diagrams of As content in arsenopyrite concerning S content (a) and Fe content (b)

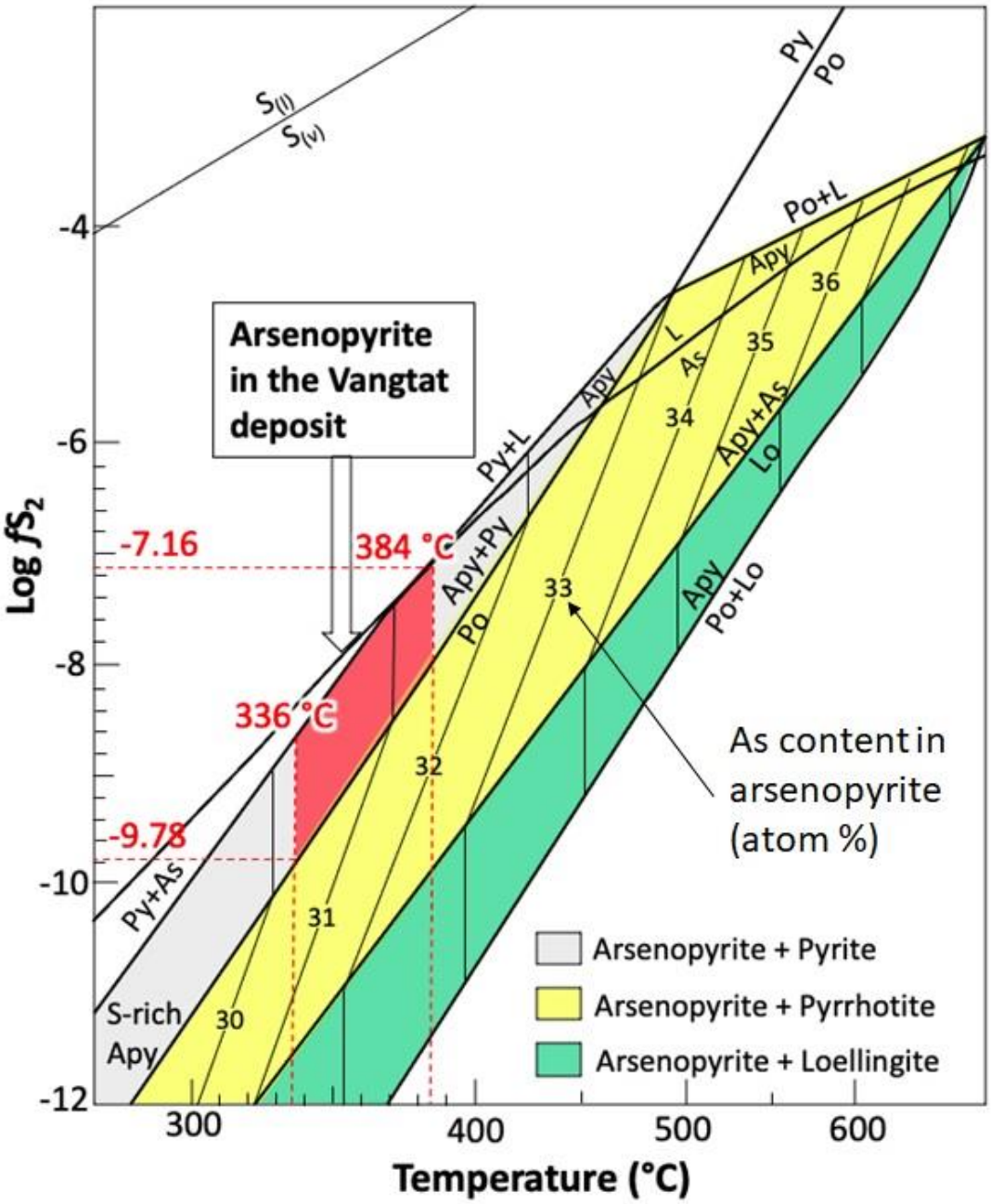

Figure 4.2: Temperature-logfS_2 diagram showed arsenopyrite stability field with atom% of As contents in the system Fe-As-S (Modified from Clark, 1960; Kretschmar and Scott, 1976; Sharp *et al.*, 1985)

Arsenopyrite is the most refractory of the common sulfides, together with its wide range in As/S ratio, makes it a potentially useful geochemical tool for interpreting its formation conditions (Kretschmar and Scott, 1976). The stability of arsenopyrite in the Fe-As-S system with equilibrium conditions coexisting between arsenopyrite and pyrite; arsenopyrite and pyrrhotite; arsenopyrite and pyrite+pyrrhotite is applicable as a geothermometer, known as arsenopyrite geothermometry (Clark, 1960; Kretschmar and Scott, 1976; Sharp *et al.*, 1985). The equilibrium phase relationship of the Fe-As-S system diagram was determined by Kretschmar and Scott (1976) and is commonly used to estimate the temperature and fS_2 of arsenopyrite and coexisting minerals.

Quartz-sulfide veins are the main orebody of the Vangtat gold deposit, in which gold is closely associated with the crystallization of sulfide, most commonly pyrite (Chapter 3.4.5). Textural relationship and coexistence of auriferous pyrite and arsenopyrite in the veins (Figure 3.6c; Chapter 3) suggest equilibrium conditions and validate the estimation of the approximate formation temperature of the Vangtat gold mineralization. The range of As content in arsenopyrite from the Vangtat deposit plotted in the pyrite-arsenopyrite phase of the Fe-As-S system diagram (Figure 4.2; Clark, 1960; Kretschmar and Scott, 1976; Sharp *et al.*, 1985) estimated the temperature range of 336-384 °C, and a sulfur fugacity range of -7.16 to -9.78.

4.1.3 Gold

As described in the previous Chapters, gold in the Vangtat deposit commonly occurred as particle grains inclusion in sulfide, predominantly pyrite. The gold grade is increased together with the amount of sulfide, from the graphite-carbonate alteration envelope to

the quartz-sulfide veins. The quartz-sulfide veins define the major economic orebody with average gold grade >3 g/t Au, reaching values >100 g/t in selected hand specimens and drill core intercepts. Semi-quantitative analysis on gold crystals inclusion in pyrite displayed a relatively high Au content ranging from 78.4 to 96.0 atom% with an average of 87.8 atom%. Gold to silver ratio ranges from 4:1 to 24:1, with an average of 10:1 (Table 4.1).

4.2 FLUID INCLUSIONS

Fluid inclusions are widely presented in the sample from various geologic environments, especially hydrothermal ore deposits (Roedder, 1984). Fluid inclusions trapped in ore and gangue minerals have provided essential evidence to the understanding formation of hydrothermal mineral deposits, such as temperature, pressure, and composition of the ore-forming fluid (Roedder, 1984; Shepherd *et al.*, 1985; Bodnar, 2007). Therefore, the study of fluid inclusions is a key factor to characterize the physical-chemical condition of ore formation and depositional mechanism (Roedder and Bodnar, 1997).

Fluid inclusion types: (1) Primary fluid inclusions, (2) Pseudo-secondary fluid inclusions, and (3) Secondary fluid inclusions, related to the timing of inclusions trapped in the host minerals. Based on the description of Bodnar (2003), the primary fluid inclusions are formed during, and as a direct result of, the growth of the surrounding host crystal. If a crystal fractures after it has been formed, some fluid may enter the fracture and become trapped as secondary fluid inclusions as the fracture heals. Thus, secondary inclusions are trapped after crystal growth is complete. If fracturing occurs during the growth of the crystal, pseudo-secondary fluid inclusion may be trapped during continued

crystal growth. The occurrence of pseudo-secondary inclusions is similar to secondary inclusions but later is followed by additional crystal growth. Accordingly, primary inclusions form when fluid is trapped on the active growing surface of the crystal and will record their initial physical-chemical condition.

This chapter presents the results of fluid inclusion studies on hydrothermal gangue mineral (i.e., quartz), including petrography observation, microthermometric data, and Laser Raman Spectroscopy analysis, in order to clarify the nature of the ore-forming process and deposition style.

4.2.1 Fluid inclusion samples

The Vangtat gold deposit occurs in the metamorphic belt, greenschist facies (Chapter 2), the major gold mineralization is associated with quartz veining, in which gold is commonly incorporated with sulfide, predominantly pyrite (Chapter 3). Therefore, defining the nature of hydrothermal fluid responsible for gold mineralization in the Vangtat deposit has focused on hydrothermal gangue mineral (i.e. quartz). Quartz samples were carefully and systematically collected from the mineralized veins, consisting of two hand specimen drill core samples (VADH017-98.00m and VADH018-134.6m; Figure 4.3a,b), and a 20190424-3 outcrop sample (Figure 4.3c). The appearance of quartz is cloudy and characterized by milky luster (Figure 4.3), commonly shows feather texture.

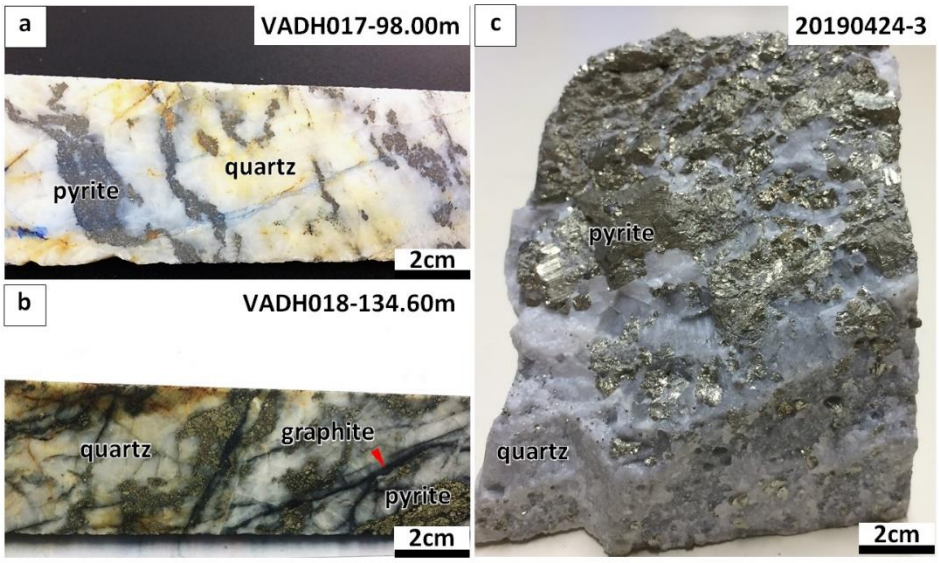

Figure 4.3: Hand specimen photos of quartz-bearing pyrite in the vein from the drill core samples (a and b), and from the outcrop in the open-pit mine (c), which were selected for fluid inclusion study

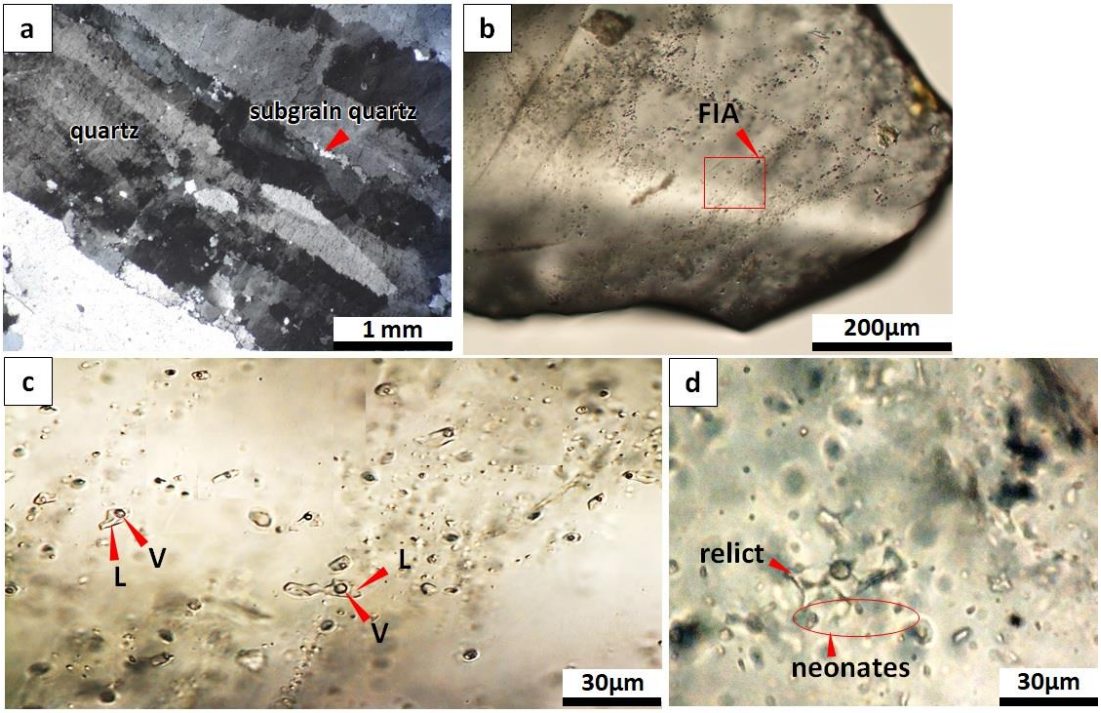

Figure 4.4: Microphotographs showing (a) Typical textures of quartz crystals in the veins; (b) Primary fluid inclusion assemblages (FIAs) along the lamella texture represented a growth zonation of quartz crystal; (c) Two-phases liquid-rich inclusions in quartz crystal; and (d) decrepitation of relict fluid inclusion and was surrounded by neonate inclusion planes

4.2.2 Fluid inclusion petrography

Various grain sizes and textures of quartz are observed under the microscope, including randomly distributed, fine-grained subhedral-anhedral crystals (Figure 4.4a). Locally, quartz is elongated with fine-grained crystallites along the large crystal boundaries (Figure 4.4a). Clear zoning within the quartz crystal is rarely observed, the growth zonation of quartz is locally indicated as lamella texture. Thus, fluid inclusion trapped in the lamella texture of quartz crystals (Figure 4.4b) and isolated groups of fluid inclusion are documented as primary fluid inclusions (e.g. Roedder, 1984). These fluid inclusions are relatively tiny in size, most commonly less than 10 μm, typically show a regular shape oval to oblate, and are randomly oriented individual inclusions, dominantly liquid-rich, two-phase liquid-vapor inclusions with similar volumetric proportions (Figure 4.4c).

Petrographic observations clarify whether the fluid inclusions record the original trapping conditions or have been modified after trapping. According to “Roedder’s rules” the fluid inclusions provide a record of the physical and chemical environment at the time of trapping assuming the: (1) the fluid inclusion traps a single, homogeneous phase, (2) the fluid inclusion volume remains constant after trapping (i.e. isochoric), and (3) nothing is lost from or added to the fluid inclusion after trapping.

Detailed petrographic observation recognized that most of the big (>20 μm) fluid inclusions are deformed and/or adapt to the irregular shapes that led to the collapsing cavity of the inclusions and leakage or partial decrepitation. The inclusions are composed of tiny newly formed (neonates) inclusions, surrounding irregular shape relicts of the precursor inclusions (Figure 4.4d), suggesting that quartz has been weakly deformed by ductile shearing after the vein formation and led to the modification of fluid inclusion inside the quartz crystals. The modification of fluid inclusion after trapping is very

common in hydrothermal vein systems in shear zones (Diamond and Tarantola, 2015). Nevertheless, small size (<20 μm) fluid inclusions remained unbroken and still preserved the original trapping condition (e.g. “Roedder’s rule”), and they were subject to microthermometric measurements.

4.2.3 Mircrothermometric data

Primary fluid inclusion assemblages were analyzed in order to constrain the temperature, pressure, and composition of the ore-forming fluid responsible for gold mineralization in the Vangtat deposit. Diamond (1990); Goldstein and Reynolds (1994); and Bodnar (2003) defined fluid inclusion assemblage (FIA) as a group of coeval inclusions that trapped at essentially the same: (1) time, (2) temperature, pressure, and composition, (3) number of phases and volume proportions when observed at room temperature, and (4) should display similar behavior during microthermometry.

As described in Chapter 4.3.2, most inclusions that are trapped in the quartz crystals of the Vangtat deposit are relatively small in size, thus the measurement of temperature (e.g. homogenization and melting temperatures) of fluid inclusions are complicated and in many cases of measurement are unsuccessful. Nevertheless, significant FIAs were successfully studied by microthermometry and the results are summarized in Table 4.2, and Figure 4.5. The primary FIAs that were analyzed homogenized to the liquid phase, where the vapor bubbles disappeared was recorded as homogenization temperature (T_h). Although the total homogenization temperature measured in FIAs ranges widely from 190-325°C, a narrow range of 240-250°C was observed for a majority of the fluid inclusion assemblages (Figure 4.5).

During the freezing stage (down to -90 ºC), the liquid phase of inclusions became ice, and the final melting temperature of ice is recorded for calculation salinity of fluid inclusion, based on the equation described by Bodnar (1993). The calculated salinity of FIAs range from 0.7-10.0 wt.% NaCl equivalent, and a narrow range of 4-6 wt.% NaCl equivalent is observed for a majority of fluid inclusions (Table 4.2 and Figure 4.5).

4.2.4 Fluid compositions

For many kinds of fluid inclusions, the coupling of microthermometry and Raman spectrometry is still the only feasible option to obtain compositions of single fluid inclusions (Burke, 2001). Therefore, the representative fluid inclusions were analyzed by Raman spectrometry, mainly for gaseous compositions. Resulting in the gas-phase is mainly composed of CO_2, with a minor amount of CH_4, N_2, and H_2S (Figure 4.6). Combining the results of microthermometry (Chapter 4.3.3) and Raman spectrometry indicated the essential components of hydrothermal fluid responsible for the gold mineralization in the Vangtat deposit are H_2O, NaCl, CO_2, CH_4, N_2, and H_2S, reflecting an aqueous-carbonic fluid system.

Table 4.2: Summarized the result of microthermometric data

Sample	N	T_h(°C)	Salinity (wt% NaCl equiv)
20190424-3	39	192 – 290	0.7 - 10.0
VADH018-134.6	4	213 – 273	0.9 - 5.3
VADH017-98.00	9	224 – 325	

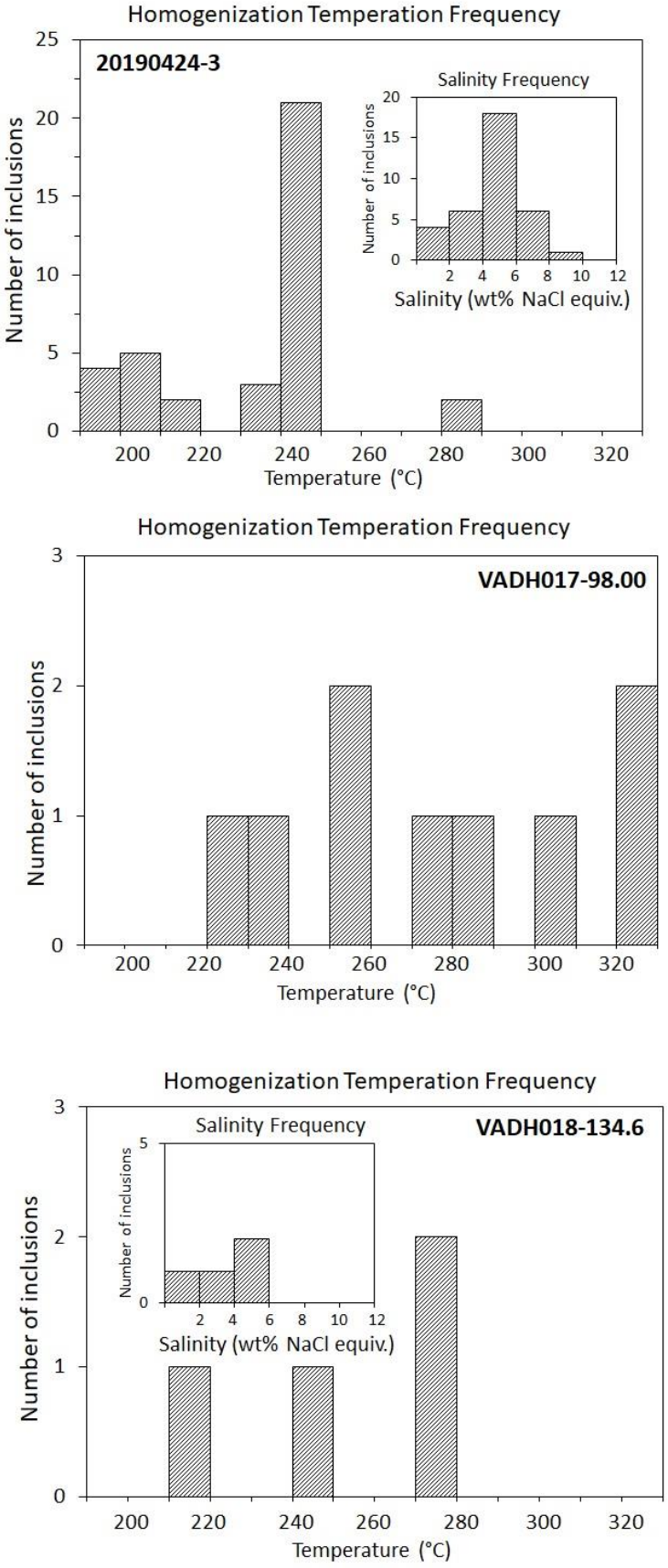

Figure 4.5: The histogram showing the results of microthermometric data from fluid inclusion study

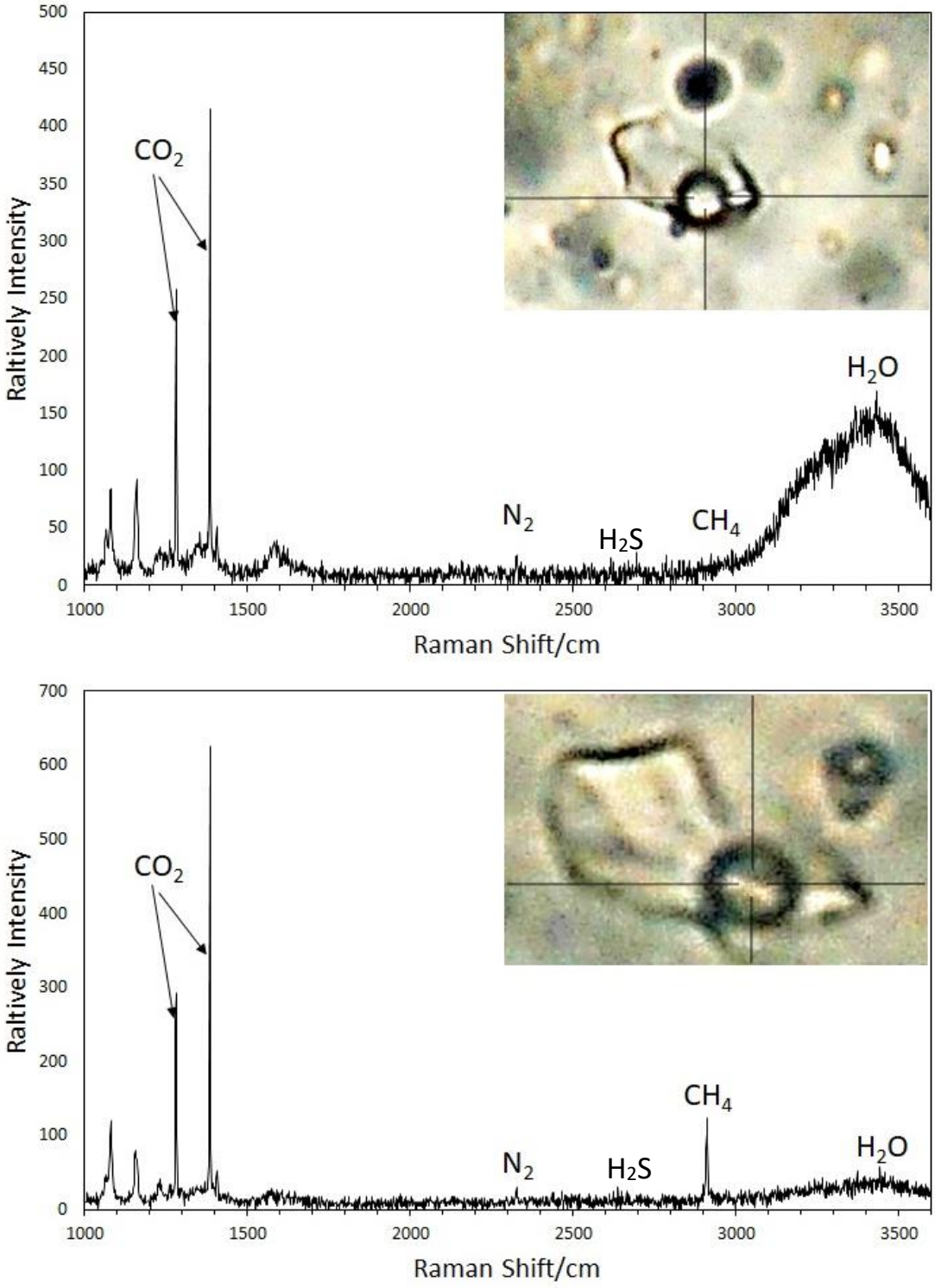

Figure 4.6: Representative of Raman spectrum analyzed gaseous composition of fluid inclusions

4.2.5 Pressure collection and depth range

Quartz-sulfide veins define the main gold mineralization in the Vangtat deposit (Chapter 3), thus the correlation between the temperature estimated from arsenopyrite geothermometry (Chapter 4.1.4) and the temperature estimated with the homogenization temperature (T_h) of the fluid inclusions could be used to estimate the pressure correction of the ore-forming fluid. This is based on the assumption that the obtained T_t of arsenopyrite geothermometry and T_h of an aqueous-carbonic fluid inclusion trapped in quartz occurred contemporaneously. Based on the correlation diagram of T_t and T_h (Figure 4.7; Diamond, 2003) the estimated pressure range of the Vangtat ore formation is 330 to 400 Mpa. This pressure range translates to the depth range of 10 to 12 km (based on a typical lithostatic pressure gradient of 100 MPa=3 km). The depth of ore formation in the Vangtat deposit is comparable to the depth of the orogenic gold systems generally (5-15 km; Goldfarb and Groves, 2015).

4.3. SULFUR ISOTOPE STUDY

Metal deposits are commonly associated with sulfide minerals, although in deposits where the ores are non-sulfide (e.g. gold), the ores are still incorporated with sulfide minerals (Ohtomo and Rye, 1979). Sulfur isotopes in sulfide could retain the original composition throughout most post-mineralization processes (Sangster, 1979), therefore, the sulfur isotope study may provide a key method to clarify aspects of the genesis of the ore deposits. This could provide key insight into: (1) possible sources of sulfur in ore-forming fluid, (2) precipitation mechanisms and chemical conditions of sulfur during ore formation, and (3) temperatures of mineralization environment (Ohtomo and Rye, 1979).

Four stable isotopes of sulfur denoted as ^{32}S, ^{33}S, ^{34}S, and ^{36}S, and their percentage abundances are approximately 95.02, 0.75, 4.21, and 0.02, respectively (MacNamara and Thode, 1950). The ratio between the two most abundant isotopes ($^{34}S/^{32}S$) is often used in the geochemistry of ore deposits (e.g. Rollinson, 1993). The isotopic composition is determined by the measurement of the $^{34/32}S$ ratio ($\delta^{34}S$) with results expressed as part per thousand or per mil (‰). Experimental defined the different values of $\delta^{34}S$ represented the different origin or environment of sulfur (e.g. Ohtomo and Rye, 1979).

Fifteen pyrite samples were collected from the main Vangtat mineralization in the Vangat gold mine, including samples of the altered pelitic schist, the graphite-carbonate alteration envelope, and gold-bearing quartz veins. The sulfur isotope ratios of these pyrite samples were measured using the conventional technique (See Appendix III for the detailed analytical method and sample preparation). The results of sulfur isotope analysis are presented in Table 4.3. Pyrite from quartz-sulfide veins and graphite-carbonated alteration envelope yield a $\delta^{34}S$ isotope composition ranging from +3.8 to +7.8‰, while most data from the high-grade gold (>3 g/t) samples plot between +4 and +6‰ (Figure 4.8). Two hydrothermal pyrites from altered pelitic schist show $\delta^{34}S$ values of +1.3 and +10.7‰ (Figure 4.8).

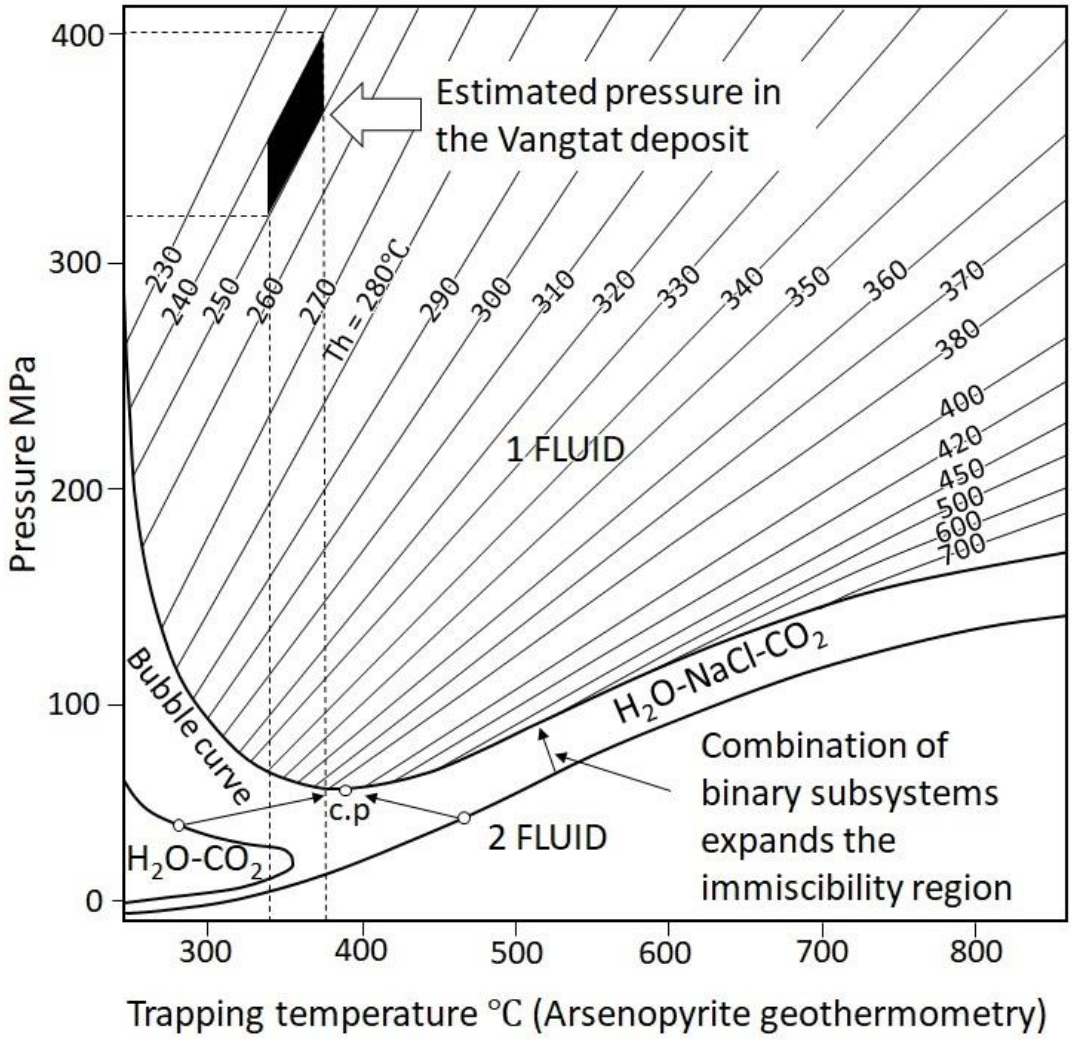

Figure 4.7: Quantitative P-T projection of phase relations in an H_2O-NaCl-CO_2 system (Modified after Diamond, 2003)

Table 4.3: Summarized the results of sulfur isotope composition

Sample Number	Mineral	D 34SV-CDT‰	Gold grade (g/t)	Zone occurrence
VADH016-172.20	Pyrite	10.7	-	Host rock
VADH018-160.00	Pyrite	1.3	-	Host rock
VADH018-141.00	Pyrite	5.0	11.55	Graphite-carbonate
VADH018-146.50	Pyrite	4.7	5.00	Graphite-carbonate
VADH051-75.50	Pyrite	7.1	0.22	Graphite-carbonate
VADH051-152.30	Pyrite	5.6	0.67	Graphite-carbonate
VADH017-90.70	Pyrite	4.6	93.30	Quartz vein
VADH017-98.00	Pyrite	4.8	30.30	Quartz vein
VADH018-134.6	Pyrite	5.1	10.55	Quartz vein
VADH018-145.50	Pyrite	4.7	24.00	Quartz vein
VADH033B-92.60	Pyrite	3.8	1.71	Quartz vein
VADH055-50.35	Pyrite	4.6	1.37	Graphite-carbonate
VADH076-57.10	Pyrite	5.3	5.74	Graphite-carbonate
VADH131-81.00	Pyrite	7.8	14.65	Graphite-carbonate
VADH154-100.00	Pyrite	5.5	4.52	Graphite-carbonate

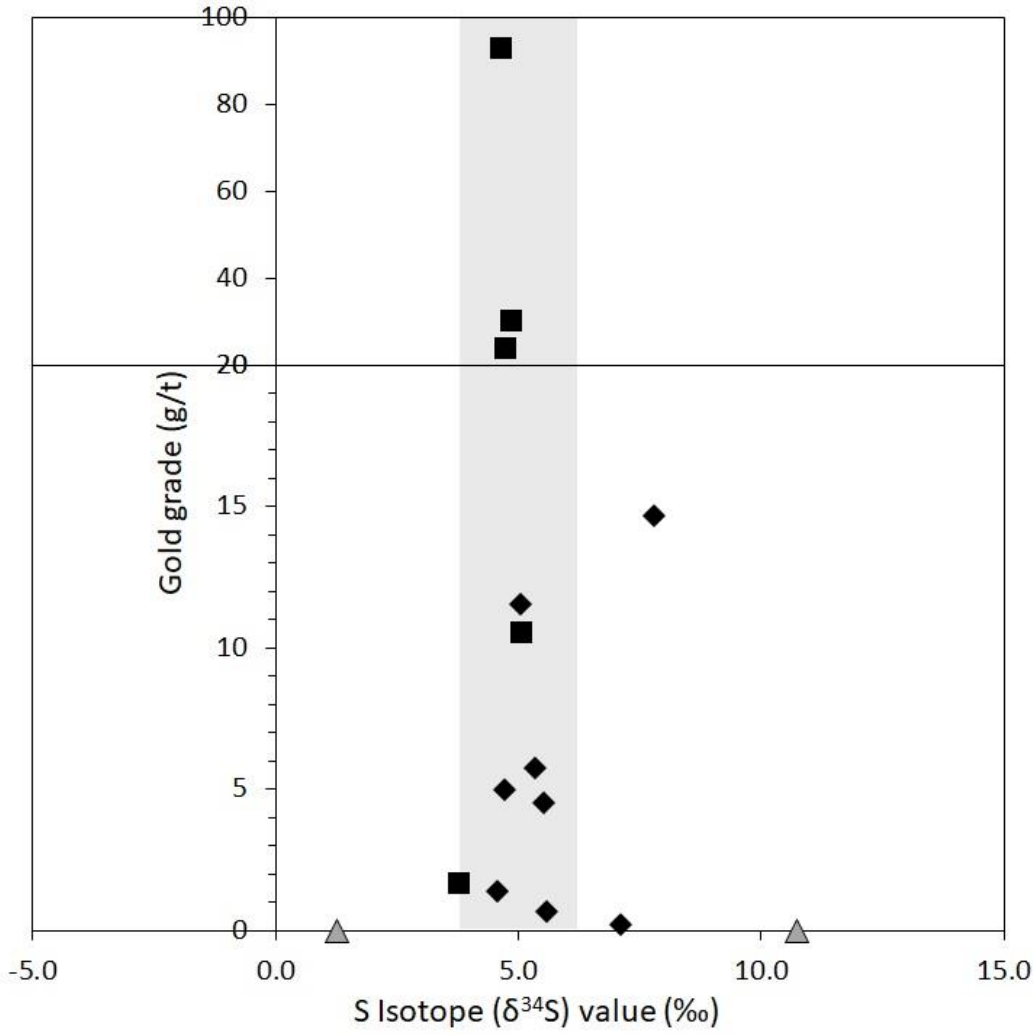

Figure 4.8: Diagram summarized sulfur isotope composition respecting the gold assay

4.4. DISCUSSION

Sulfide, predominantly pyrite, is the main host to gold in the Vangtat deposit. Most of the auriferous pyrite is homogeneous in texture (i.e. rare zoning texture is observed), coarse-grained and up to ~1 cm in diameter (Chapter 3). Chemically this pyrite is consistent in composition and contains low concentrations of other elements in solid solution. These typical characteristics of auriferous pyrite in the Vangtat deposit suggest that pyrite formed during the hydrothermal processes, which allows the crystallization of pyrite slowly growth and most of the trace elements are partitioned into the separated phases rather than incorporated in a solid solution in pyrite (Butler and Rickard, 2000).

The evolution of gold mineralization in the Vangtat deposit is similar to the model of sediment-hosted orogenic gold deposit, Goldfarb *et al*. (2005); Chang *et al*. (2008); and Large *et al*. (2011) proposed gold within pyrite was mobilized from the surrounding protolith and concentrated to ore grades by hydrothermal processes along permeable, with potentially some magmatic involved. The evidence observed of an overgrowth texture of pyrite with lower arsenic content in the porous core part of pyrite crystals compared to the crystal rim. Suggesting an aggregation and recrystallization of pyrite accompanied by a release of trace elements in pyrite led to remobilization and reconcentration during the hydrothermal processes (e.g. Large *et al*., 2009).

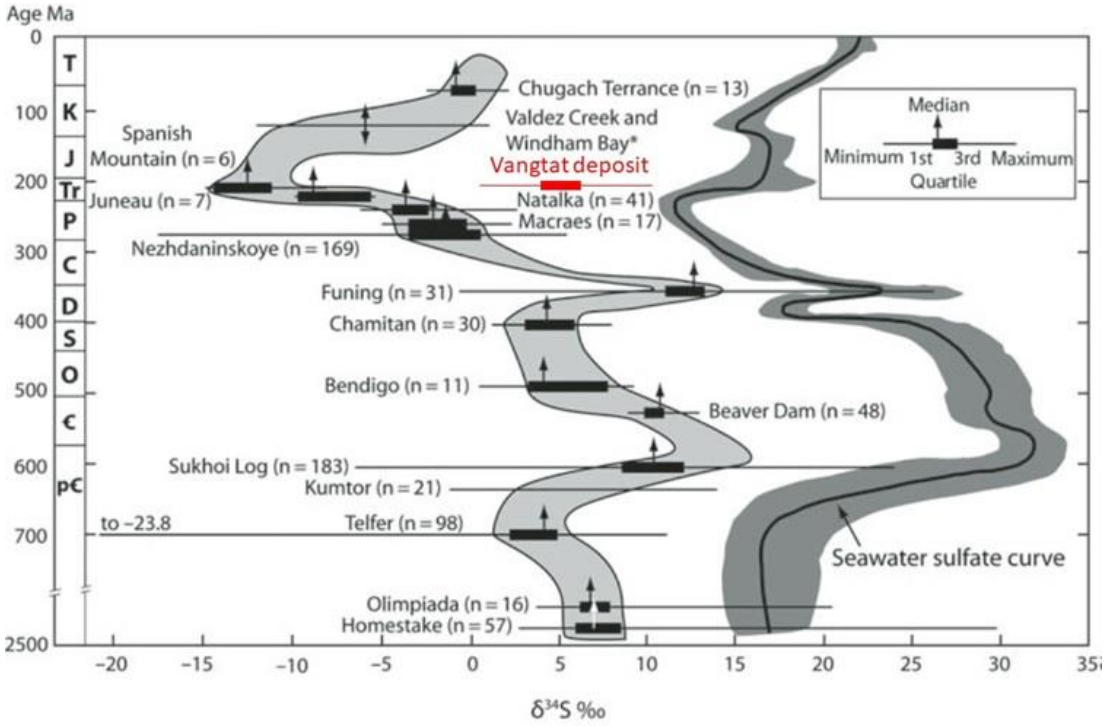

Figure 4.9: Variation of sulfur isotope composition in sedimentary-hosted orogenic gold deposit through geological time and seawater sulfate cuvre (Chang *et al.*, 2008). The figure shows the sulfur isotope compositions in the Vangtat deposit through the geological time are not related to the seawater sulfate curve.

4.4.1 Source of gold

The geologic characteristics of gold mineralization in the Vangtat deposit are similar to typical shear-zone hosted, orogenic gold deposits elsewhere. Gold is closely associated with sulfide minerals, predominantly pyrite, therefore the sulfur source may be critical in defining (1) the gold source region(s), (2) the source of hydrothermal fluid, and (3) the genesis of the deposit. The source of sulfur and ore-forming fluid in orogenic gold deposits has been debated for many decades. Various hypotheses have been proposed for the source of gold and sulfur, such as: (1) Magmas (Burrows and Spooner, 1985; Muntean *et al*., 2011) or igneous intrusions (Colvine, 1989), (2) Mantle at depth (Perring *et al*., 1987; Barley and Groves, 1990; Hronsky *et al*., 2012), and (3) Sedimentary rocks (Pitcairn *et al*., 2006; Large *et al*., 2007) or rocks within sedimentary basins (Chang *et al*., 2008). Most recent research proposes that metamorphic dehydration and devolatilization during metamorphism of hydrate mafic rocks at the amphibolite-greenschist facies boundary is the preferable source for fluids and gold of orogenic gold deposits (Phillips and Powell, 2010; Tomkins, 2013; Goldfarb and Groves, 2015).

Ore bodies of the Vangtat gold deposit lie far away from any significant granitic intrusions (Chapter 2), and no direct relationship has been observed between these granitic intrusions and the mineralized bodies. Therefore, the regionally present granitic magmas cannot explain the source and genesis of the Vangtat gold deposit.

Chang *et al*. (2008); Large *et al*. (2009, 2011) proposed gold within pyrite of orogenic gold deposits was sourced from sedimentary basins; such pyrite tends to be fine-grained, framboidal in shape and enriched in other trace elements including Co, Ni, Cu, As, Se, Mo, Ag, Sb, Te, Pb, Bi, and Au (Butler and Rickard, 2000; Large *et al*., 2009). Auriferous

pyrite in the Vangtat deposit is not similar to pyrite in the sedimentary pyrite formation (see discussion above). Furthermore, the timing of gold mineralization in the Vangtat gold belt is confined to a late-Triassic age (206 Ma or slightly younger; see Chapter 5). The sulfur isotope composition of pyrite in the Vangtat deposit does not appear to be related to seawater sulfate, as suggested by a comparison of the sulfur isotope composition of seawater through geological time (Figure 4.9; Chang *et al*., 2008). This suggests the source of sulfur and ore components is not related to the sedimentary sulfide in the host rock.

The majority of the sulfur isotope in the Vangtat deposit is restricted to a narrow range from +4 to +6 ‰, possibly indicative of a single phase of the sulfur source. This isotopic composition is compatible with the $\delta^{34}S$ composition range of the most igneous rocks (Ohtomo and Rye, 1979). Furthermore, the $\delta^{34}S$ composition of the Vangtat pyrite (+4 to +6 ‰) is comparable to the $\delta^{34}S$ composition (-4 to +4‰) of the Phouc Son deposits in central Vietnam (Chapter 2) which was interpreted to be magmatic in origin (Manaka, 2014, unpublished data). Combining the discussions on $\delta^{34}S$ composition and the geological and mineralogical features of the Vangtat gold deposit it appears that mafic igneous rocks situated in the footwall and forming the basement of the deposit (Chapter 2) could be a plausible source for gold in the Vangtat deposit. Thus gold would possibly be remobilized from deeper units and transported to the site of deposition during metamorphic dehydration and devolatilization.

4.4.2 Ore-forming fluid

The nature of hydrothermal fluid responsible for gold mineralization in the Vangtat deposit is better understood by the study of the fluid inclusions trapped in hydrothermal quartz crystals in the veins. This indicates that ore-forming fluid was aqueous-carbonic, low salinity (up to 10 wt% NaCl equivalent) and mainly composed of H_2O, CO_2, with minor CH_4, N_2, and H_2S. The low salinity fluid is consistent with the fact that gold in the Vangtat deposit was predominantly transported as sulfide complexes and base-metals sulfide assemblage were less significant.

FIAs from the Vangtat gold deposit revealed a wide range of T_h from 190 to 325 ºC. Fall and Bodnar (2018) proposed that the range in T_h for FIAs from orogenic gold deposits is generally greater than other hydrothermal mineral deposits, and likely reflects the fact that fluid inclusions from metamorphic environments are more likely to reequilibrate after trapping. Therefore, a relatively narrow range (240 to 250 ºC) for the majority of FIAs from the Vangtat deposit is preferably assigned to the T_h of ore-forming fluid.

Phillips and Evans (2004) proposed that CO_2 within the fluid is likely a critical factor in providing the near-neutral pH buffering required for elevated gold solubility as a gold-sulfide complex. CH_4 and N_2 gases within the fluid and the presence of hydrothermal graphite in the quartz-sulfide veins and alteration halo (Chapter 3) supporting the suggestion that reduced conditions were present in the ore-forming fluid at the Vangtat gold deposit (e.g. Bodnar *et al*., 2014).

The coexistence of H_2O-NaCl-CO_2 in the fluid composition at Vangtat suggests fluid immiscibility (Sterner and Bodnar, 1984; Bodnar *et al*., 2014), which is an important

mechanism associated with gold in many hydrothermal systems (Hagemann and Luders, 2003). Fluid immiscibility in the shear zone that hosted mineralized vein is interpreted to have been produced during the cyclic decompression of the hydrothermal fluid, associated with the seismic movement along the shear zones (Sterner and Bodnar, 1984; Hagemann *et al*., 1992), which could have led to the exsolution of the volatiles such as CO_2 and H_2S. The exsolution of volatiles from the ore fluids may be responsible for the destabilization of the gold-bearing sulfide complex, resulting in the precipitate of abundant gold (Phillips and Evans, 2004).

4.5. SUMMARY

- Gold at the Vangtat deposit occurs predominantly as particle grains inclusion in pyrite, relatively high Au to Ag ratio, with an average of 10:1. Main pyrite host gold is relatively consistent in composition, dominant of other sulfide inclusions, and less of other elements in solid solution.
- T_h of FIAs range from 190 to 325 ºC, a narrow range (240 to 250 ºC) is observed for the majority of fluid inclusions and assigned to be T_h for ore-forming fluid. T_t (336 to 384 ºC) was obtained from arsenopyrite geothermometry. The correlation of T_h and T_t estimated the entrapment depth of ore formation at the Vangtat deposit is 10 to 12 km, this depth range is comparable to the depth of orogenic gold deposits.
- The significant $\delta^{34}S$ composition of the Vangtat deposit ranges from +4 to +6‰, is overlapped with the $\delta^{34}S$ composition of orogenic gold deposits and consistent with $\delta^{34}S$ composition of the most igneous rocks, and is comparable to the other known sediment-hosted orogenic gold deposits in the region (e.g. Phouc Son deposits).

- The nature of hydrothermal fluid responsible for gold mineralization in the Vangtat deposit is characterized by an aqueous-carbonic fluid, low salinity, mainly composed of H_2O, CO_2, with minor CH_4, N_2, and H_2S, and appears to be reduced and near-neutral in pH.
- The plausible interpretation model of the Vangtat gold deposit identified that gold and ore-forming fluid were derived from mafic igneous rocks during the metamorphic dehydration and devolatilization, and gold was concentrated to the ore grades during the hydrothermal activities.

CHAPTER 5 MINERALIZATION GEOCHRONOLOGY

5.1. INTRODUCTION

Mainland SE Asia is composed of the Gondwana-derived tectonic terranes, including the Indochina, South China, and Sibumasu Terranes, which are assembled and amalgamated by subduction and collision orogenesis during late-Palaezoic-Mesozoic time (Bunopas, 1981; Charusiri *et al*., 2002; Metcalfe, 1999; 2011; Hutchison, 2014). The Indochina Terrane is a major tectonic unit and is made up of several tectonic domains, which are dominantly characterized by magmatic and metamorphic rocks, and associated with significant metallogenic belts in the region. Collision orogenesis between the eastern extension of Indochina Terrane with the Kontum Massif resulted in the formation of the Poko suture zone and associated structures (Lepvrier *et al*., 2004), including the Vangtat shear zone (Chapter 2), which is the main host of a recently discovered orogenic gold belt in southeastern Laos, the Vangat gold belt.

Magmatism, metamorphism, deformation, and hydrothermal alteration along the domain boundaries surrounding and within the Indochina Terrane resulted in the formation of a variety of precious- and base-metal deposits, notably porphyry-related skarn, epithermal, sediment-hosted and orogenic gold deposits (Zaw *et al*., 2014; Kirwin and Royle, 2019).

The age of porphyry-related skarn and epithermal mineralization in the Indochina Terrane is relatively well constrained (246 to 305 Ma; Cromie, 2010; Kamvong *et al*., 2014; Salam *et al*., 2014) and it is associated with early-Permian to middle-Triassic

magmatic arcs in the Loei and Truong Son fold belts (Zaw *et al*., 2014). However, the age of orogenic gold mineralization is poorly constrained. Tran *et al*. (2014) proposed that gold mineralization at the Bong Mieu deposit in the Tam Ky-Phuoc Son suture zone in central Vietnam occurred originally during an initial ductile shear event at ca. 430 Ma and, subsequently, gold was remobilized to form auriferous quartz veins with sulfides during a brittle-ductile deformation event at ca. 240 Ma (Middle Triassic) based on a Re-Os molybdenite age. Hydrothermal biotite for the Phuoc Son gold deposit was dated by Manaka (2014) at 212 and 204 Ma (Late Triassic).

Orogenic gold deposits are commonly hosted in mica-bearing schist and the interpretation of K-Ar and Ar-Ar age data on mica minerals may present challenges because authigenic hydrothermal mica may have been mixed with mica of metamorphic and/or detrital origin from the host rocks (e.g. Haines and van der Pluijm, 2008). An additional potential complication during the application of K-Ar and Ar-Ar dating methods on samples of orogenic gold mineralization is the presence of excess argon in associated minerals, because in fluid-rich environments, such as shear zones, excess argon may partition into the minerals or become incorporated in fluid inclusions (Kelley, 2002a, b).

This Chapter reports K-Ar ages of nine portions of white mica (one bulk sample and two samples separated into four size fractions each) in the mineralized vein from the Thongkai-Ok deposit, one of the deposit in the Vangtat gold belt.

5.2. WHITE MICA SAMPLES

For the K-Ar dating age of the gold mineralization in the Vangtat gold belt, three white mica-bearing quartz-pyrite samples were collected from the main open pit of the Thongkai-Ok mine, which is located approximately 7 km north of the main Vangtat mine (Figures 2.3; Chapter 2). Samples 20190404-5 and 20190404-6 were collected from a wide (>5 m) quartz-sulfide vein zone in the open-pit wall (Figure 5.1a), and sample TKO-1 is from a massive quartz-sulfide-white mica vein fragment from the main ore zone inside the open-pit. All samples were collected from primary hydrothermal mineralization below the supergene oxidation zone which is present in the upper part of the pit. The three samples are composed mainly of quartz, white mica, and pyrite (Figures 5.1b-d).

Quartz is characterized by a milky luster (Figure 5.1b-d) and composed of various grain sizes and textures, including randomly distributed fine-grained subhedral-anhedral crystals intimately intergrown with white mica and pyrite (Figure 5.1e,f). Locally, quartz is elongated within fine-grained crystallites along the large crystal boundaries. The quartz crystals in the vein contained abundant fluid inclusions (Chapter 4) in an isolated group of fluid inclusion assemblages.

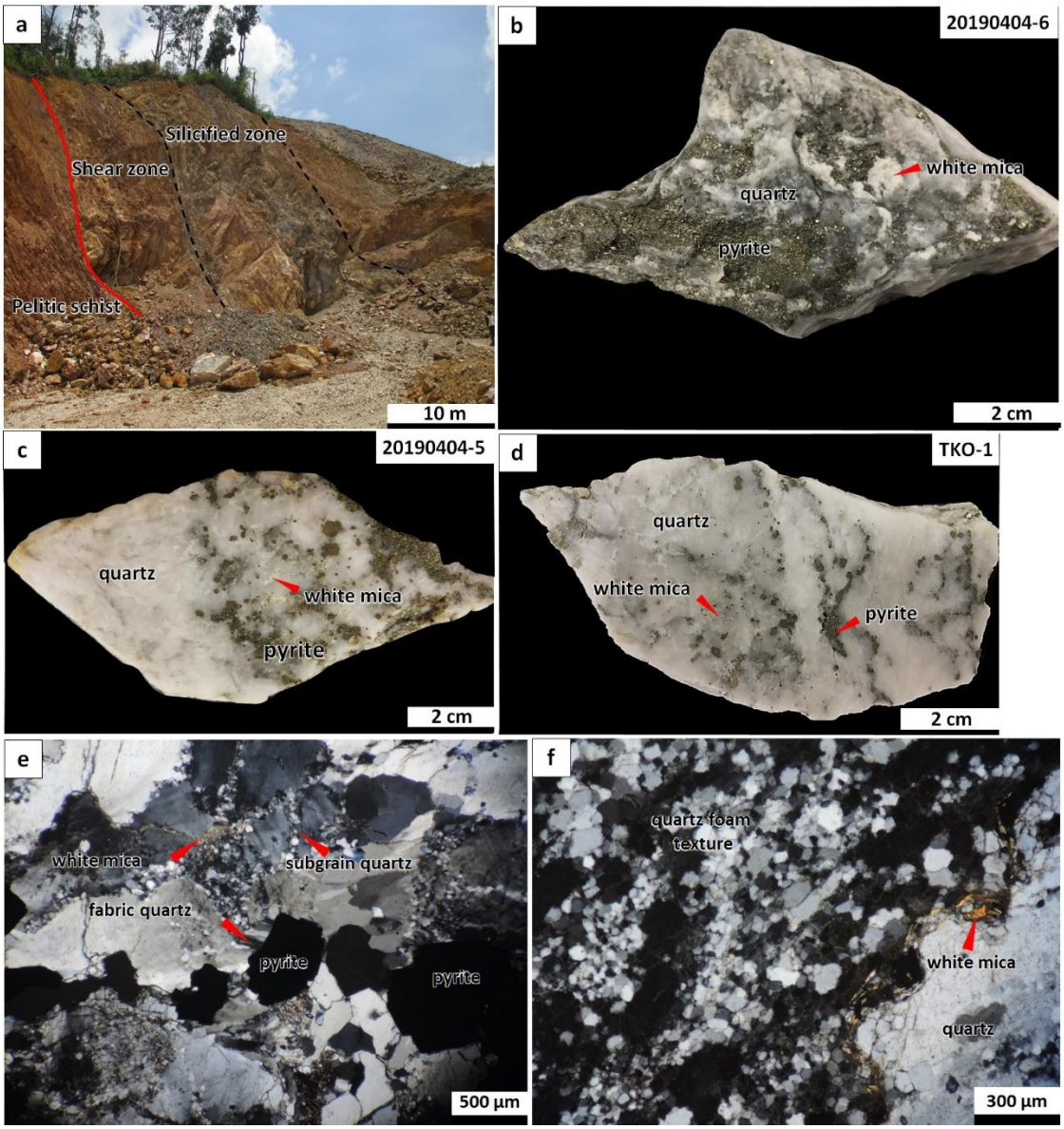

Figure 5.1: (a) The outcrop of sample location (20190404-5/6) at the Thongkai-Ok deposit, Vangtat gold belt, (b-d) Hand specimen samples of gold ore composed of quartz vein with abundant pyrite and white mica, and (e-f) Microphotographs of gold mineralized vein fragments showing main mineral constituents: quartz, pyrite, and white mica

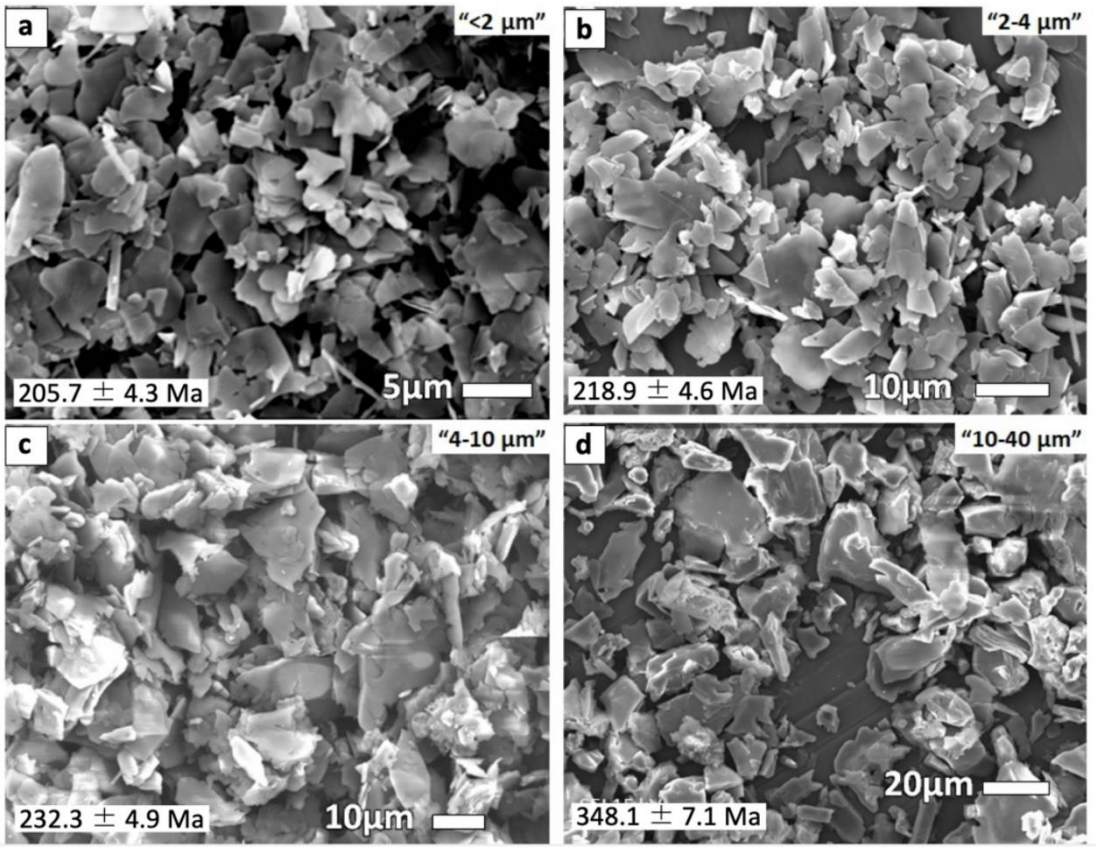

Figure 5.2: Representative SEM secondary electron images of white mica in sample TKO-1 separates from the Thongkai-Ok gold deposit, including a) <2 μm, b) 2-4 μm, c) 4-10 μm, and d) 10-40 μm.

5.2.1 Sample preparation

Two samples (TKO-1 and 20190404-5) were separated into four different size fractions (nominally < 2, 2-4, 4-10, and 10-40 μm) by standard gravitational settling techniques, using 1% sodium hexa-meta-phosphate as an anti-flocculant (Wasserman *et al*., 1992). A clean, bulk (<40 μm) sample was prepared from sample 20190404-6 after drilling out coarse white mica clusters (Figure 5.1b).

A Rigaku Multiflex X-ray diffractometer (Cu-Kα radiation) was used to characterize the random-oriented powder of the white mica separates. Observations under a scanning electron microscope (SEM) were conducted on the different size fraction separates from sample TKO-1 (Figure 5.2) to better understand the actual size range of the different separates collected by gravitational settling. For the finer-grained size fractions (<2, 2-4, and 4-10 μm), the actual size range was slightly larger than the planned size range: 1-4, ~3-8, and ~6-15 μm, respectively (Figure 5.2a-c; Table 5.2).

The major element chemical composition of the white mica was determined in polished thin sections of samples TKO-1 and 20190404-5 by quantitative wavelength dispersive X-ray analysis using a JEOL JXA-8800R electron microprobe (Table 5.1). All sample preparation and characterization were performed at the laboratories of the Graduate School of International Resource Sciences of Akita University.

The chemical composition of the white mica in bulk samples TKO-1 and 20190404-5 was calculated by quantitative wavelength dispersive X-ray analysis using a JEOL JXA-8800R electron microprobe (Table 5.1). Analytical conditions were: acceleration voltage: 15 kV, beam current: 20 nA, beam diameter: 2 μm. Standard materials used were quartz, (anorthite 65) plagioclase, hematite, periclase, rutile, rhodonite, V-metal,

jadeite, and orthoclase. Detection limits of Si, Al, Fe, Mg, Ti, Mn, V, Ca, Na, and K are 166, 120, 138, 130, 165, 125, 126, 35, 115, and 120 ppm, respectively. All sample preparation and characterization was performed at the laboratories of the Graduate School of International Resource Sciences of Akita University.

5.2.2 K-Ar analyses

Nine white mica ± quartz fractions were analyzed for K-Ar dating at Okayama University of Science. The measurement of potassium and argon of the separated fractions and the age calculations were carried out following the procedures described by Nagao *et al.* (1984) and Itaya *et al.* (1991). Total potassium content was measured in duplicate by flame photometry using a 2000 ppm Cs buffer. The analytical precision was better than 2 % at the 2-sigma confidence level (Itaya *et al*., 1991). Argon isotopes were analyzed with a 15 cm-radius sector-type mass spectrometer with a single collector system by the isotopic dilution method using a ^{38}Ar spike. The precision of the isotopic analyses was about l % at the 2-sigma confidence level (Yagi *et al*., 2015).

5.3 RESULTS

5.3.1 White mica identification

The mineral characterization using X-ray diffraction (XRD) of the different samples prepared from the veins in the Thongkai-Ok gold deposit indicates the dominance of white mica (Figure 5.3). In sample TKO-1, three main white mica peaks are present at 9.68Å, 4.90Å, and 3.29Å; however, the white mica peaks of the 4-10 μm and 10-40 μm fractions are slightly shifted to 9.90Å, 4.98Å, and 3.32Å, respectively, and the 3.32Å peak overlaps with a quartz peak. Quartz peaks are clearly detected in the 4-10 μm and 10-40 μm fractions of this sample, and the intensity of the quartz peaks increases, consistent with the larger size fraction and quartz abundance (Figure 5.3). The main white mica peaks of samples 20190404-5 and 20190404-6 also occur at 9.90 Å, 4.98 Å, and 3.32Å (Figure 5.3). Quartz peaks are observed in all fractions of sample 20190404-5; similar to sample TKO-1, the intensity of the quartz peaks is greater in the coarser size fractions (4-10 μm and 10-40 μm). Chlorite peaks are detected in all fractions of sample 20190404-5. No quartz or chlorite peaks are detected in sample 20190404-6.

The XRD patterns indicate subordinate peaks of white mica between 22° and 33° 2θ in all the fractions of sample 20190404-5, 20190404-6, and the coarser fractions (4-10 μm and 10-40 μm) of sample TKO-1. These peaks are not present in the fine fractions (<2 μm and 2-4 μm) of sample TKO-1 (Figure 5.3). These subordinate peaks occur at 3.72Å, 3.49Å, 3.20Å, 2.98Å, 2.86Å, and 2.79Å; they reflect the stacking sequence of the $2M_1$ white mica polytype (Moore and Reynolds, 1997).

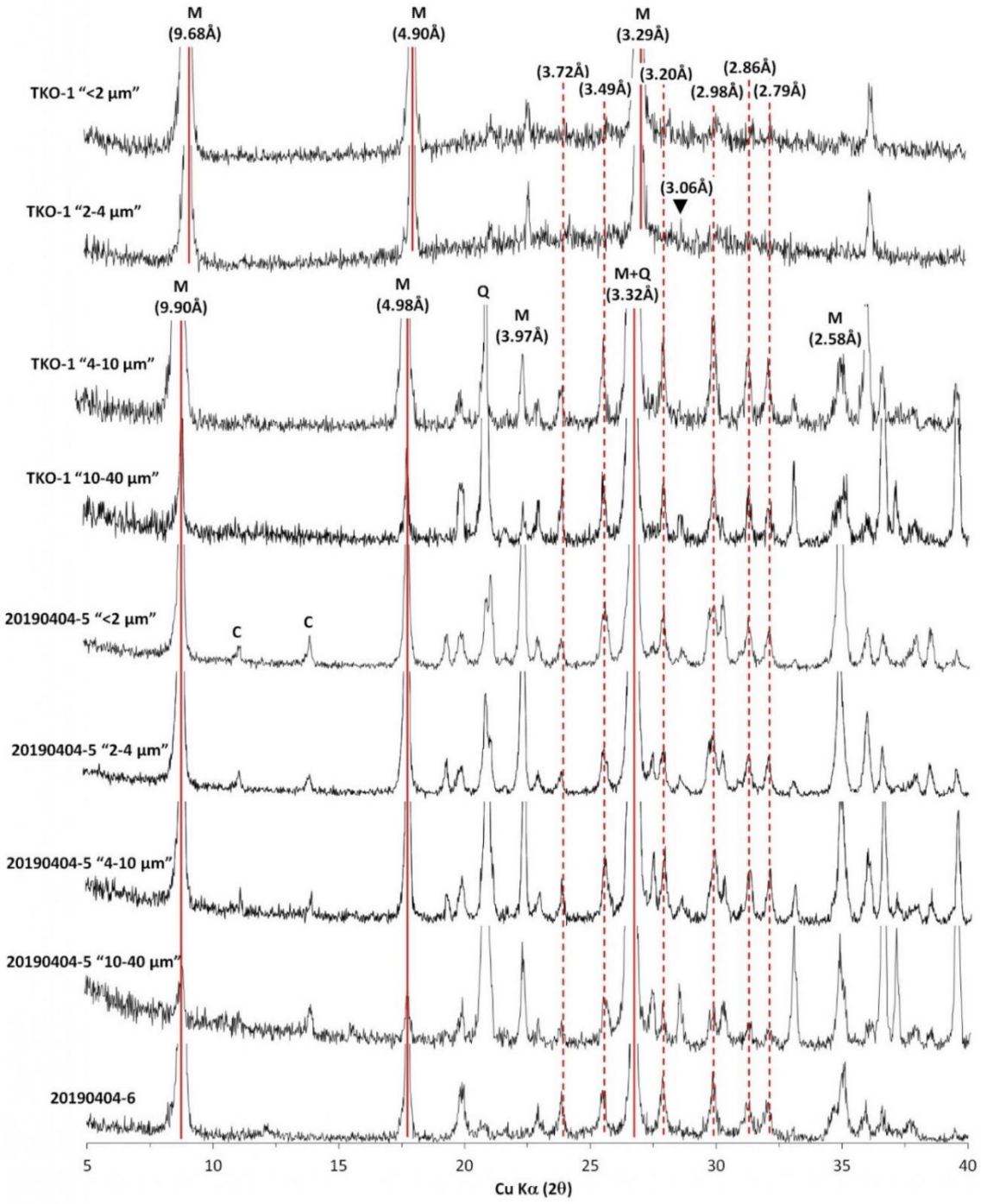

Figure 5.3: X-ray diffraction patterns of white mica sample separates from gold mineralized quartz-pyrite-white mica veins in the Thongkai-Ok gold deposit. The solid red lines represent the main white mica peak and the red dashed lines are the 2M1-specific peaks. C: chlorite peak; M: white mica peak and Q: quartz peak.

The identification of white mica polytypes is focused on a 2.98Å peak, which is representative of the (025) reflection of $2M_1$ white mica (Togashi, 1979). This peak is observed in all fractions, with lower intensity in the finer size fractions (<2 μm and 2-4 μm) of sample TKO-1. The XRD patterns indicate that the dominant white mica polytype in samples 20190404-5, 20190404-6, and the coarser size fractions (4-10 μm and 10-40 μm) of sample TKO-1, is $2M_1$. The (112) reflection of 1M polytype at 3.06Å (Togashi, 1979) is observed as a low-intensity peak in sample 20190404-5 and the coarsest fraction of TKO-1. Studies of K-Ar systematics of clay minerals from fault zones have interpreted 1M white mica as authigenic in origin vs $2M_1$ white mica polytype as detrital (e.g. Haines and van der Pluijm, 2008). However, $2M_1$ white mica is also commonly hydrothermal (e.g., the main white mica in the El Salvador porphyry Cu deposit; Watanabe and Hedenquist, 2001). Overall, we do not find evidence in the samples from the Thongkai-Ok quartz veins to propose two separate populations of white mica with widely different origins (authigenic vs detrital) and age of formation (see below).

5.3.2 Chemical composition of white mica

Polished thin sections of samples TKO-1 and 20190404-5 were analyzed to determine the chemical composition of white mica from Thongkai-Ok, in particular the K_2O content. White mica, with a grain size ranging between <10 μm and ~100 μm, is randomly distributed with quartz grains, most commonly along the boundaries of quartz crystals (Figure 5.1e,f). The chemical composition of these white mica crystals is shown in Table 5.1; the results show the chemical composition, with K_2O content that ranges from 8.61 to 9.79 wt%, consistent with muscovite values. The equivalent potassium

content from these white mica crystals ranges between 7.15 and 8.13 wt%, with an average of 7.62 wt% for sample 20190404-5 and 7.71 wt% for sample TKO-1 (Table 1).

5.3.3 K-Ar age dating

The results of K-Ar analyses of all fractions are shown in Table 5.2. The percentage of non-radiogenic ^{40}Ar is low (maximum 2.1%, with 7 of 9 fractions 0.2 to 0.7%), indicating little disturbance by air contamination. The potassium content in the fractions of sample TKO-1 increases from 2.14 ± 0.04 to 6.53 ± 0.13 wt%, together with decreasing sample fraction size (Table 5.2). The calculated K-Ar ages for sample TKO-1 range from 205.7 ± 4.3 to 348.1 ± 7.1 Ma; the older ages corresponding to the coarser fractions with lower potassium contents. The fractions of sample 20190404-5 show lower potassium concentrations than sample TKO-1, ranging from 2.94 ± 0.06 to 4.07 ± 0.08 wt%. The calculated K-Ar ages range from 281.6 ± 5.8 to 348.0 ± 7.1 Ma. Unlike sample TKO-1 there is no systematic change with fraction size; the finest fraction (<2 μm) yielded an older age (330 ± 6.7 Ma) than the 2-4 μm and 4-10 μm fractions (281± 6.7 Ma and 320 ± 6.7 Ma, respectively). Sample 20190404-6 showed the highest concentration of potassium among the analyzed samples (7.85 ± 0.16 wt%) and yielded an age of 235.4 ± 4.9 Ma.

Table 5.1: Representative major element chemical composition of white mica in the mineralized vein at the Thongkai-Ok deposit

Sample	20190404-5									
SiO_2 (wt%)	46.01	46.57	48.34	48.62	48.97	48.00	48.84	48.64	47.03	49.02
Al_2O_3	35.99	35.16	36.14	34.52	33.37	37.90	33.62	36.62	35.26	35.28
FeO*	0.05	0.18	0.12	0.12	0.14	0.07	0.45	0.21	0.52	0.32
TiO_2	0.00	0.20	0.12	0.19	0.12	0.03	0.16	0.03	0.04	0.02
MnO	0.01	0.01	0.03	0.00	0.00	0.00	0.00	0.01	0.00	0.00
MgO	0.41	1.24	0.89	1.50	1.53	0.37	1.58	0.69	0.58	0.97
V_2O_3	0.05	0.02	0.04	0.02	0.05	0.03	0.00	0.00	0.01	0.02
CaO	0.06	0.03	0.04	0.03	0.02	0.03	0.05	0.02	0.05	0.04
Na_2O	0.55	0.26	0.27	0.15	0.16	0.30	0.26	0.38	0.70	0.47
K_2O	8.89	9.42	8.98	9.49	9.73	8.95	9.34	9.37	8.80	8.84
Total	92.02	93.07	94.95	94.64	94.09	95.68	94.31	95.96	92.99	94.97
K content	7.38	7.82	7.45	7.88	8.08	7.43	7.75	7.78	7.31	7.34
Avg. of K content:		7.62	wt%							
APFU calculations based on 11 oxygen										
Si	3.11	3.13	3.16	3.20	3.25	3.11	3.23	3.15	3.15	3.20
Al(vi)	1.98	1.91	1.95	1.88	1.85	2.01	1.85	1.95	1.94	1.92
Al(iv)	0.89	0.87	0.84	0.80	0.75	0.89	0.77	0.85	0.85	0.80
Fe	0.00	0.01	0.01	0.01	0.01	0.00	0.02	0.01	0.03	0.02
Ti	0.00	0.01	0.01	0.01	0.01	0.00	0.01	0.00	0.00	0.00
Mn	0.00	0.00	0.00	0.00	0.00	0.00	0.00	0.00	0.00	0.00
Mg	0.04	0.12	0.09	0.15	0.15	0.04	0.16	0.07	0.06	0.09
V	0.00	0.00	0.00	0.00	0.00	0.00	0.00	0.00	0.00	0.00
Ca	0.00	0.00	0.00	0.00	0.00	0.00	0.00	0.00	0.00	0.00
Na	0.07	0.03	0.03	0.02	0.02	0.04	0.03	0.05	0.09	0.06
K	0.77	0.81	0.75	0.80	0.82	0.74	0.79	0.78	0.75	0.74

Table 5.1: (Continue)

Sample	TKO-1									
SiO_2 (wt%)	47.35	47.62	48.15	47.86	47.65	48.18	48.24	48.94	47.45	48.34
Al_2O_3	36.66	37.76	35.95	35.94	35.42	37.20	34.70	33.76	35.68	33.57
FeO*	0.08	0.16	0.67	0.18	0.14	0.09	0.32	0.16	0.24	0.19
TiO_2	0.06	0.06	0.05	0.04	0.09	0.04	0.21	0.13	0.05	0.11
MnO	0.00	0.02	0.00	0.00	0.02	0.00	0.00	0.00	0.01	0.00
MgO	0.51	0.29	0.56	0.38	0.99	0.47	1.28	1.65	0.47	1.42
V_2O_3	0.01	0.00	0.00	0.01	0.00	0.01	0.01	0.03	0.01	0.06
CaO	0.00	0.02	0.05	0.04	0.04	0.02	0.04	0.02	0.06	0.03
Na_2O	0.37	0.62	0.42	0.31	0.21	0.27	0.21	0.16	0.37	0.18
K_2O	9.65	9.00	9.40	8.61	9.31	9.08	9.17	9.65	9.16	9.79
Total	94.69	95.55	95.24	93.37	93.85	95.34	94.19	94.49	93.49	93.68
K content	8.01	7.47	7.80	7.15	7.73	7.54	7.61	8.01	7.60	8.13
Avg. of K content:		7.71	wt%							
APFU calculations based on 11 oxygen										
Si	3.13	3.11	3.16	3.18	3.16	3.14	3.19	3.23	3.16	3.23
Al(vi)	1.98	2.01	1.95	1.99	1.94	2.00	1.90	1.86	1.97	1.87
Al(iv)	0.87	0.89	0.84	0.82	0.84	0.86	0.81	0.77	0.84	0.77
Fe	0.00	0.01	0.04	0.01	0.01	0.00	0.02	0.01	0.01	0.01
Ti	0.00	0.00	0.00	0.00	0.00	0.00	0.00	0.00	0.00	0.00
Mn	0.00	0.00	0.00	0.00	0.00	0.00	0.00	0.00	0.00	0.00
Mg	0.05	0.03	0.05	0.04	0.10	0.05	0.13	0.16	0.05	0.14
V	0.00	0.00	0.00	0.00	0.00	0.00	0.00	0.00	0.00	0.00
Ca	0.00	0.00	0.00	0.00	0.00	0.00	0.00	0.00	0.00	0.00
Na	0.01	0.02	0.01	0.01	0.01	0.01	0.01	0.00	0.01	0.00
K	0.81	0.75	0.79	0.73	0.79	0.75	0.77	0.81	0.78	0.83

Note: FeO* : total iron as FeO

Table 5.2: The K-Ar age dating results of white mica samples from the Thongkai-Ok deposit

No.	Sample No.	Mineral	Grain size* (μm)	K content (wt.%)	Rad.^{40}Ar (10^{-7}cc STP/g)	K-Ar age (Ma)	Non-rad.^{40}Ar (%)
1	TKO-1	White mica	< 2	6.53 ± 0.13	552 ± 5	**205.7 ± 4.3**	0.4
2			2-4	5.93 ± 0.12	535 ± 5	**218.9 ± 4.6**	0.6
3			4-10	5.96 ± 0.12	573 ± 6	**232.3 ± 4.9**	0.3
4			10-40	2.14 ± 0.04	319 ± 3	**348.1 ± 7.1**	1.6
5	20190404-5	White mica	< 2	2.94 ± 0.06	414 ± 4	**330.6 ± 6.7**	0.4
6			2-4	4.07 ± 0.08	481 ± 5	**281.6 ± 5.8**	0.2
7			4-10	3.54 ± 0.07	482 ± 6	**320.1 ± 6.9**	0.4
8			10-40	3.01 ± 0.06	449 ± 4	**348.0 ± 7.1**	0.7
9	20190404-6	White mica	NO	7.85 ± 0.16	766 ± 8	**235.4 ± 4.9**	2.1

Note: *These were the targeted grain sizes, the real grain size measured by SEM are closer to 1-5, 4-10, 6-15, and 10-30 μm.

5.4. DISCUSSION

The white mica studied from the Vangtat gold belt was extracted from massive quartz-pyrite-white mica veins being mined in the main open pit of the Thongkai-Ok deposit. There is no evidence that the gold-bearing hydrothermal quartz veins sampled (Figure 5.1b-d) contained fragments of any significance from the surrounding host rocks. The composition of the mineralized vein in the Thongkai-Ok deposit, Vangtat gold belt, consisting of quartz, muscovite (white mica), and sulfides, mainly pyrite. This mineral association within the gold mineralization in the Vangtat gold belt is associated with the hydrothermal activity, which formed from hydrothermal fluids ascending upon entering an ore trap or site of deposition (Chapter 3). Therefore, the K-Ar age of hydrothermal white mica in the gold-bearing quartz-sulfide vein should constrain the timing of gold mineralization in the Vangtat gold belt.

The results of the K-Ar dating reveal a complex dataset, characterized by a large variation (~140 m.y) and age overlap among samples (Table 5.2). This wide range of age is insignificant to constrain the age of gold mineralization in the Vangtat gold belt. Although the interpretation of the results is not immediate or straightforward, there are two main alternative interpretations are carried out to discuss in order to define the age of gold mineralization in the Vangtat gold belt, such as (1) Mixture of older detrital white mica from the wall rocks with younger authigenic (hydrothermal) white mica, and (2) Excess argon in the sample impurities, mainly quartz.

5.4.1 Mixture of detrital and authigenic white mica

Numerous researchers have used K-Ar analyses to understand the age of faulting by analyzing white mica-bearing fault gouge (e.g. Takagi *et al*., 2005; van der Pluijm *et al*., 2001; Haines and van der Pluijm, 2008). The method is based on the separation of coarser-grained detrital white mica in the wall rocks from fine-grained (<2 μm) white mica of authigenic origin (commonly $2M_1$ and 1M, respectively; Lyons and Snellenburg, 1970; Kralik *et al*., 1987). A range of K-Ar ages is obtained that is characterized by younger ages that correspond consistently with a decreasing grain size in the sample (e.g. Takagi *et al*., 2005; Haines and van der Pluijm, 2008; Bui *et al*., 2017).

At Thongkai-Ok, the gravity settling preparation process to separate different size fractions showed a small amount of sample reporting to the finest grain size fraction. Upon SEM observation, the nominally <2 μm size fraction showed an actual grain size range of ~1-4 μm (Figure 5.2a). The overall lack of <1 μm material is consistent with the chemical composition of the Thongkai-Ok white mica that corresponds to muscovite, rather than finer-grained illite.

The K-Ar ages of sample TKO-1 range from 205.7 ± 4.3 Ma (<2 μm) to 348.1 ± 7.1 Ma (10-40 μm), with an older age obtained from the coarser and lower potassium content fractions (Figures 5.3 and 5.4a). This systematic change in age could potentially be interpreted as the mixture of different populations of white mica polytypes in the samples, i.e. fine-grained hydrothermal illite in the fine-grained size fraction and detrital and/or metamorphic coarser-grained muscovite in the coarser-grained fraction. However, the ages of sample 20190404-5 vary randomly without relation to size fraction, i.e., the finest fraction yields a relatively older age compared to the coarser fractions (Figure 5.4a). In

addition, the coarse-grained white mica sample 20190404-6 returns a relatively young age of 235.4 ± 4.9 Ma.

The XRD characterization of the analyzed samples indicates the dominance of $2M_1$ white mica regardless of the fraction size. This observation, combined with the lack of a consistent relationship between age and grain size, indicates that a mixture of white mica polytypes does not explain the K-Ar ages obtained.

5.4.2 Excess argon

With the exception of sample 20190404-6, a correlation is observed between the potassium content of the samples analyzed and their calculated age (Table 5.2, Figure 5.4b). The range in potassium content is interpreted to reflect the amount of quartz present in the sample as an impurity. This interpretation is consistent with the XRD patterns, where quartz peaks are lowest in the samples with the highest wt% potassium, i.e., TKO-1 (<2 μm), 6.53 wt%; TKO-1 (2-4 μm), 5.93 wt%; TKO-1 (4-10 μm), 5.96 wt%; and 20190404-6, 7.85 wt% K. These four fractions yield the youngest K-Ar ages: 205.7 ± 4.3, 218.9 ± 4.6, 232.3 ± 4.9, and 235.4 ± 4.9 Ma, respectively (Table 5.2). By contrast, fractions with the lowest potassium content show prominent quartz peaks in the X-ray diffractograms and yield the oldest K-Ar ages: TKO-1 (10-40 μm), 2.14 wt% K, 348.1 ± 7.1 Ma; 20190404-5 (<2 μm), 2.94 wt% K, 330.6 ± 6.7 Ma; and 20190404-5 (10-40 μm), 3.01 wt% K, 348.0 ± 7.1 Ma (Table 5.2).

A possible explanation for these results, which is consistent with previous studies (e.g. Kelley, 2002a; Itaya *et al.*, 2005, Itaya, 2020) is the presence of excess argon derived from various sources that produce an age older than the actual age. The excess argon at

Thongkai-Ok is likely to be present inside fluid inclusions in the hydrothermal quartz, as proposed in previous K-Ar and Ar-Ar studies of hydrothermal mineralization, including porphyry copper and MVT-type deposits (e.g. Rama *et al*., 1965; Kelley *et al*., 1986; Kraus *et al*., 1999; Kelley, 2002a). This phenomenon is potentially common in this type of shear zone-hosted hydrothermal system, where high fluid pressures and different sources of argon may be present.

A plot of potassium content vs K-Ar age (Figure 5.4b) for the Thongkai-Ok samples suggests a mixing trend between the two main end-member components, quartz and white mica, at about 440 Ma and 170 Ma, respectively. Other factors, such as the presence of some detrital or metamorphic white mica inherited from the host rocks, or repeated hydrothermal and faulting events, etc., cannot be excluded and they may be present. However, the two end-members above exert the main control on the distribution of the analytical results. As a result, and assuming the formation of white mica in veins was contemporaneous with gold mineralization, convincingly interpret the youngest age obtained from quartz-free white mica samples, 205.7 Ma, as closest to the age of mineralization in the Vangtat gold belt, it is possible that the mineralization age could potentially be as young as ~170 Ma, if the age vs potassium content relation is extrapolated to average 7.6 wt% potassium composition of white mica in the Thongkai-Ok samples (Table 1, Figure 5.4b).

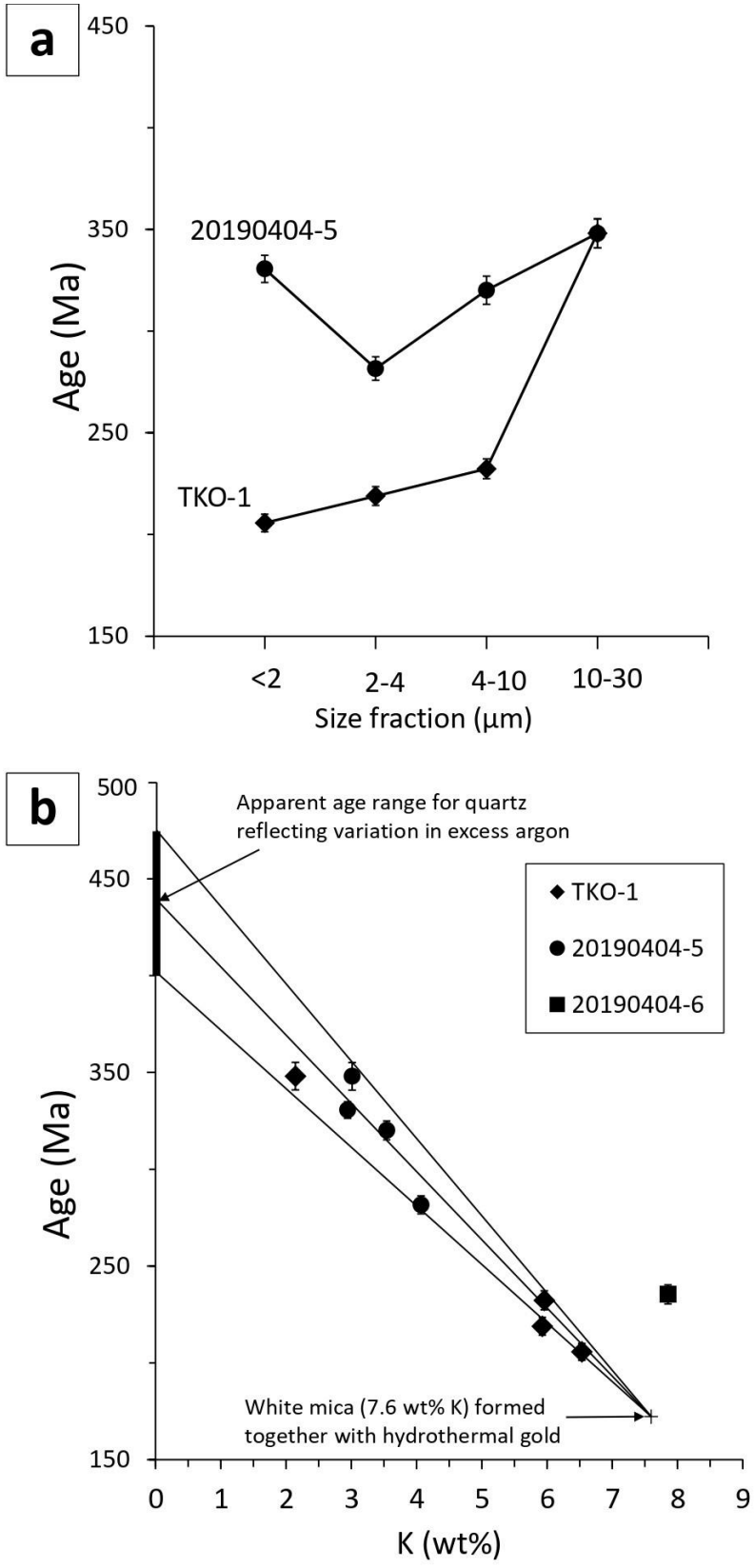

Figure 5.4: The variation of K-Ar ages versus the fraction size (a) and potassium content (b).

5.4.3 Estimation amount of excess argon

The quartz and white mica are intergrown, and most likely formed from the same hydrothermal fluid. Therefore, the white mica should also have some excess argon, and the potential effect of this excess argon can be estimated. The radiogenic argon accumulated in minerals by the decay of ^{40}K can be calculated back using the age equation if the age and potassium content are given. The radiogenic argon in quartz with 0.1 wt% potassium is 7 (10^{-7} cc STP/g) if the age is 170 Ma. The excess argon-bearing quartz, with an average apparent age of ~440 Ma (440 ± 30 Ma, Figure 5.4b), has a total argon content of 19 (10^{-7} cc STP/g). Thus, the excess argon amount is 12 (10^{-7} cc STP/g), obtained by subtraction (19 – 7). On the other hand, the total argon amount of the ~170 Ma white mica end-member component is 526 (10^{-7} cc STP/g). If the mica contains the equivalent amount of excess argon calculated for quartz above, the calculated age of the white mica is 166 Ma, i.e., 526 – 12 = 514 (10^{-7} cc STP/g). This examination indicates the age difference is within the error of age determination.

5.4.4 Conclusions and regional implications: relation of gold mineralization event and regional tectonic evolution

As discussed above, convincingly interpret the youngest age of quartz-free white mica samples from the Thongkai-Ok gold deposit (206 ± 4 Ma) as closest to the age of orogenic gold mineralization in the Vangtat gold belt of southeastern Laos. The mineralization age could be as young as ~170 Ma, if the measured K-Ar age vs.

potassium content relation is extrapolated to the average potassium content of the white mica fractions analyzed.

A 206 Ma age for the Thongkai-Ok orogenic gold deposit, Vangtat gold belt, southeastern Laos is consistent with regional geological and geochronological data and indicates a post-collisional, post-peak metamorphism hydrothermal gold event that is potentially younger than much of the orogenic gold mineralization in nearby Vietnam, as follows:

- Regional magmatism and metamorphism in the Kontum Massif associated with the collision between the South China and Indochina terranes has been dated at 270-230 Ma (zircon U-Pb data; Lepvrier *et al.* 2004; Owada *et al.*, 2016).
- Late-stage metamorphism in the Kontum Massif was dated by Osanai *et al*. (2008) as ca. 245-230 Ma. Argon-argon dating of metamorphic biotite from mica schist indicated an age of 237 to 229 Ma (Vu Van Tich *et al*., 2007).
- Undeformed plutonic rocks (i.e., related to post-collisional magmatism) were identified in the region (Lepvrier *et al*., 2008; Faure *et al*., 2014) and an undeformed granite in the Poko Suture Zone, dated at 204 Ma (Lepvrier *et al.*, 2004), was interpreted to represent the younger age limit of shearing and suturing in the region.
- Orogenic gold mineralization associated with the Tam Ky-Phuoc Son suture zone in central Vietnam, over 100 km east of Thongai-Ok was tentatively dated at 240 Ma by Tran *et al*. (2014) on molybdenite (Re-Os) from the Bong Mieu gold deposit. Manaka (2014) obtained 212 and 204 Ma ages from ^{40}Ar-^{39}Ar dating of hydrothermal biotite in an auriferous vein in the Phuoc Son deposit, the nearest deposit to Thongkai-Ok, and of similar age.

5.5 SUMMARY

- The objective of this study is to establish the age of mineralization in the Vangtat orogenic gold belt by K-Ar dating of hydrothermal white mica in the gold-bearing quartz-sulfide veins in order to better understand its spatial and temporal relation to other gold deposits in Southeast Asia and regional tectonic events
- Three-white mica bearing quartz-pyrite samples were collected from the open pit at Thongkai-Ok. The dominant white mica phase in the samples is $2M_1$ muscovite and the K_2O content measured by electron microprobe techniques in individual white mica crystals ranged between 8.61 and 9.79 wt%.
- Two of the three vein samples were separated by gravity settling into four size fractions, <2, 2-4, 4-10 and 10-40 μm, respectively. The results of potassium measurements by flame photometry in the K-Ar sample aliquots show a range in potassium content which reflects the amount of quartz present in each sample as an impurity.
- With one exception, a correlation was observed between potassium concentration in the samples, including the size fraction separates, and the calculated K-Ar age. The large range of calculated ages, from 348 to 206 Ma, is interpreted to reflect excess argon contained in fluid inclusions in the hydrothermal quartz present in the analyzed samples. Interpreting the youngest age of the quartz-free samples, 206 ± 4 Ma was the closest to the age of mineralization in the Vangtat gold belt. The age could be as young as ~170 Ma if the age vs. potassium content relation is extrapolated to the average potassium content of white mica in the samples analyzed

- The gold mineralization event in the Vangtat gold belt is comparable to the other gold deposits in the region (e.g. Phuoc Son deposit, Bong Mieu deposit). This mineralization event is younger than the regional metamorphic event and magmatic intrusion in the region, possibly relate to the waning stage of the tectonic event of the Indosinian orogeny.

CHAPTER 6 CONCLUSION

6.1. GEOLOGY, MINERALOGY, AND GEOCHRONOLOGY

6.1.1 Summary of geological setting

The Indochina Terrane is a major tectonic unit of mainland southeast Asia and is bound to the north by the South China Terrane and to the west by the Sibumasu Terrane, with the Truong Son fold belt and the Loei and Sukhothai fold belts marking broad collision zones with the two continental terranes (Lepvrier *et al*., 2004; Hutchison, 2014). Broadly coincident with these tectonic collisions, several internal domains were amalgamated to the Indochina Terrane during the Triassic with right-lateral shear movement (Lepvrier *et al*., 2008, Osanai *et al*., 2008). Collision with the Kontum Massif resulted in the formation of the Poko suture zone and associated structures (Lepvrier *et al*., 2004), including the Vangtat shear zone, which is the main host of a recently discovered Vangtat orogenic gold belt in southeastern Laos.

Magmatism, metamorphism, deformation, and hydrothermal alteration along the domain boundaries surrounding and within the Indochina Terrane resulted in the formation of a variety of precious- and base-metal deposits, notably porphyry-related skarn, epithermal, sediment-hosted and orogenic gold deposits (Zaw *et al*., 2014; Kirwin and Royle, 2019). The orogenic gold deposits occur along shear zones associated with the Poko and the Tam Ky-Phuoc Son suture zones in southeastern Laos and central Vietnam.

The N-S striking Poko suture zone marks the geological boundary between the eastern extension of the Indochina Terrane and the Kontum Massif (Lepvrier *et al*., 2008). The Kontum Massif is mainly composed of early- to mid-Palaeozoic (Cambrian to Devonian) metamorphic complexes of granulite to greenschist facies (United Nations, 1990; Osanai *et al*., 2008). These units were metamorphosed during the Late Permian to Triassic Indosinian tectonic event (ca. 270-230 Ma; Lepvrier *et al*., 2008; Osanai *et al*., 2008).

The western extension of the Kontum Massif in southeastern Laos is composed of low-grade metamorphic rocks similar to those of the Kham Duc complex (Osanai *et al*., 2008). Further to the west of the Kontum Massif, within the Indochina Terrane, lies the Khorat Basin, a Late Triassic to Cretaceous continental sedimentary basin (red beds) formed above Permian and Triassic sedimentary rocks (Smith and Stokes, 1997; Minezaki *et al*., 2019; Faure *et al*., 2018). The youngest major geologic unit in the region consists of Paleogene-Neogene basaltic lava flows (Vilayhack *et al*., 2008; Faure *et al*., 2018).

The Vangtat shear zone is one of the subsidiary shear zones associated with the regional Poko suture zone. The Vangtat shear zone strikes north-south and extends for more than 30 km, broadly marking the border between southern Laos and Vietnam. The western extension of the Kontum Massif is the main host to the Vangtat shear zone and is composed of early- to mid-Palaeozoic pelitic and psammitic schist, greenschist, and quartzite with subordinate mylonitic, gneissic, and undeformed intrusive rocks (Vilayhack *et al*., 2008). These metamorphic units host several recently discovered gold prospects, including the Gieng Dat, Vangtat, and Thongkai-Ok deposits that have been developed. These occurrences are aligned for ~10 km along the Vangtat shear zone; the Xekong gold prospect is located further to the northeast, along a subparallel north-south structure.

Two principal rock units occur in the Vangtat district: the lower unit consists of metagabbro of unknown age (possibly Precambrian; Vilayhack *et al*., 2008), and the upper unit is composed of metasedimentary lithologies, including pelitic schist, slate, metasandstone, and quartzite. Thongkai-Ok, one of the actively mined gold deposits associated with the Vangtat shear zone, is located approximately 7 km north northeast of the Vangtat gold mine. The lithological units around the Thongkai-Ok deposit, as well as other hard-rock (primary) gold deposits in the district, are covered by a thick (~ up to 50 m) blanket of weathering and supergene oxidation, which led to local gold remobilization and concentration of secondary gold in surficial detrital sediments. This young alluvial gold has been recovered by artisanal miners through the district for many years and marks the first recorded gold mining in the region. Current gold mining at Thongkai-Ok and Vangtat is entirely on hard-rock deposits and is the subject of this study.

The main host rocks in the Thongkai-Ok and Vangtat gold deposits are mica schist and pelitic schist of Ordovocian-Silurian age. Gold mineralization occurs mainly within the foliated pelitic schist, which consists of oriented muscovite and chlorite with finely interlayered quartz and plagioclase. Within the Vangtat shear zone, the host rocks are strongly deformed and sheared, and a quartz veining/silicification zone up to 10 m thick marks the most heavily deformed and gold-mineralized core. Discrete pyrite-bearing quartz veins occur within the silicified zone as well as in the heavily sheared pelitic schist host. Fragments of quartz veins are brecciated and cemented with pyrite in the silicified zone, and boudinaged within the shear zone. The mineralized sulfide-quartz veins may also contain abundant white mica.

High-grade gold mineralization (> 3g/t Au on average; reaching values >100 g/t Au in selected hand specimens and drill core intercepts) occurs only in the quartz-sulfide-white

mica veins. Lower-grade gold mineralization (avg. < 3g/t Au) occurs in a graphite-carbonate-quartz-sulfide hydrothermal alteration zone that forms an envelope around the veins and grades into a sub-economic to barren altered pelitic schist. Disseminated sulfides in the graphite-carbonate alteration envelope may attain up to 10 vol%, but are typically less than 1 vol% in the altered host pelitic schist in the outer alteration envelope. As a general rule, sulfide content decreases together with gold concentration from the quartz-sulfide veins at the center towards the host rocks on the margin of alteration.

6.1.2 Hydrothermal alteration and mineralogy

Quartz veins mark the core of hydrothermal activity and represent the fluid pathway, hence the hydrothermal alteration and fluid-rock interaction mainly occurred along and adjacent to the quartz veins. The hydrothermal fluid transected two different types of wall rock lithologies with contrasting lithologies (e.g. metagabbro in the lower portion and pelitic schist in the upper portion) that display a variety of alteration assemblages. The fluid-rock interaction reaction indicated the hydrothermal fluid responsible for gold mineralization in the Vangtat deposit, Vangtat gold belt is characterized as relatively high CO_2 content and near-neutral pH condition, and gold is carried as sulfide complex along with the ore-forming fluid.

The vein is defined as the main mineralization stage, composed of quartz, pyrite (with other sulfides such as chalcopyrite, arsenopyrite, sphalerite, galena, bismuthinite, pyrrhotite), graphite, carbonate, white mica, and chlorite. The early mineralization stage marked by graphite-carbonate alteration envelope is composed of graphite, calcite, dolomite, quartz, and pyrite (with minor chalcopyrite and arsenopyrite), most likely

dominate the foliated chlorite-muscovite of the host pelitic schist. The alteration assemblage within the mineralized host rock (i.e. pelitic schist) indicated the hydrothermal fluid is in equilibrium with the host rock, since the hydrothermal alteration occurred, the major silicates of alteration assemblage (e.g. quartz, plagioclase, white mica, and chlorite) had contained the same major silicates as those of the unaltered rock.

6.1.3 Age of mineralization and regional implication

The presence of hydrothermal white mica-bearing auriferous vein from the Thongkai-Ok deposit was subject for K-Ar dating in order to constrain the age of gold mineralization in the Vangtat gold belt. The results provided a wide range of ages from 348 to 206 Ma. Within the interpretation of excess argon derived from contaminated quartz as an associated mineral, convincingly defined the youngest age (206 ± 4 Ma) of quartz-free fraction was the closest age of orogenic gold mineralization in the Vangtat gold belt of southern Laos. The mineralization age could be as young as ~170 Ma, if the measured K-Ar age vs. potassium content relation is extrapolated to the average potassium content of the white mica fractions analyzed.

A 206 Ma age of gold mineralization in the Vangtat gold belt, southeast Laos is consistent with regional geological and geochronological data and indicates a post-collisional, post-peak metamorphism hydrothermal gold event that is potentially younger than much of the orogenic gold mineralization in nearby Vietnam, as follows:

- Regional magmatism and metamorphism in the Kontum Massif associated with the collision between the South China and Indochina terranes have been dated at 270-230 Ma (zircon U-Pb data; Lepvrier *et al.* 2004; Owada *et al.*, 2016).

- Late-stage metamorphism in the Kontum Massif was dated by Osanai *et al*. (2008) as ca. 245-230 Ma. Argon-argon dating of metamorphic biotite from mica schist indicated an age of 237 to 229 Ma (Vu Van Tich *et al*., 2007).
- Undeformed plutonic rocks (i.e., related to post-collisional magmatism) were identified in the region (Lepvrier *et al*., 2008; Faure *et al*., 2014) and an undeformed granite in the Poko Suture Zone, dated at 204 Ma (Lepvrier *et al.*, 2004), was interpreted to represent the younger age limit of shearing and suturing in the region.
- Orogenic gold mineralization associated with the Tam Ky-Phuoc Son suture zone in central Vietnam, over 100 km east of the Vangtat gold belt, was tentatively dated at 240 Ma by Tran *et al*. (2014) on molybdenite (Re-Os) from the Bong Mieu gold deposit. Manaka (2014) obtained 212 and 204 Ma ages from ^{40}Ar-^{39}Ar dating of hydrothermal biotite in an auriferous vein in the Phuoc Son deposit, the nearest deposit to the Vangtat gold belt, and of similar age.

6.2 NATURE AND GENESIS OF GOLD MINERALIZATION

6.2.1 Deposition of gold

Gold is carried in the soluble sulfide complex along with the ore fluid (see above). The precipitation of gold is related to both: (1) The destabilization of sulfide complex by a sulfidation reaction which involves the interaction of Fe-bearing mineral (e.g. chlorite) in the host rock and S-bearing fluid, and (2) Changing the physical-chemical of the ore-forming fluid, which relates to the reduction reaction of the hydrothermal fluid with the carbonaceous material or graphite dominant in the host rock and alteration envelope that facilitated gold extraction.

6.2.2 Physical-chemical condition of the ore forming fluid

Fluid inclusions trapped in quartz crystals from mineralized veins help understand the nature of the hydrothermal fluid responsible for gold mineralization in the Vangtat deposit, Vangtat gold belt, indicating that ore-forming fluid has the homogenization temperature range of 190 to 325 ºC (240 to 250 ºC is observed for the majority of fluid inclusions) and salinity range of 0.7 to 10.0 wt% NaCl equivalent (4 to 6 wt% NaCl equivalent is observed for the majority of fluid inclusions). The gas compositions are CO_2, CH_4, N_2, and H_2S. The composition of the ore-forming fluid is considered to have been generated via metamorphic dehydration and devolatilization. The presence of these gas compositions in the ore-forming fluid may indicate the reaction of fluid-wall rocks played an important role in gold precipitation.

6.2.3 Depth of ore formation

Depth of ore formation is approximated using the pressure range of the ore formation, which was estimated using the correlation temperature between (1) homogenization temperature (240 to 250 °C) deduced for microthermometric data, and (2) trapping temperature (336-384 °C) obtained from arsenopyrite geothermometry. Providing the pressure range of 330 to 400 Mpa and translated to the depth range of 10 to 12 km (based on a typical lithostatic pressure gradient of 100 MPa=3 km).

6.2.4 Source of gold

Gold is closely associated with sulfide minerals, predominantly pyrite, therefore the sulfur source may be critical in defining the source of gold and hydrothermal fluid. The sulfur isotope composition of auriferous pyrite from the Vangtat deposit ranges from +1.3 and +10.7 ‰ and a narrow range is confined from +4 to +6 ‰ for the most population data and corresponding to the high-grade gold assay. A narrow range (+4 to +6 ‰) of $\delta^{34}S$ composition possibly indicates the single phase of the sulfur source, and these compositions are compatible with the $\delta^{34}S$ composition range of the most igneous rocks (Ohtomo and Rye, 1979). In addition, an appreciable $\delta^{34}S$ composition in the Vangtat deposit is not related to the seawater sulfate curve through the geological time. Therefore, the metamorphic dehydration and devolatilization during the metamorphism of mafic igneous rocks could potentially be the source of ore-forming fluid and gold.

6.3 CONCLUSION

In conclusion, the Vangtat gold deposit together with the Vangtat gold belt has many similarities to the orogenic gold deposits globally. The main characteristics of the Vangtat gold belt, as part of the broad spectrum of orogenic deposits, are summarized in Table 6.1.

Table 6.1: Summary of characteristics of the Vangtat deposit together with Vangat gold belt, in the context of the key parameters that unite and distinguish orogenic gold deposits

Key features of orogenic gold deposits	**Vangtat deposit characteristic**
Tectonic setting/Host structure	Collision zone/Shear structure
Host rocks/Grade	Regional metamorphic/Greenschist facies
Age of host rock metamorphism	Late-Permian to early-Triassic (ca. 270 to 230 Ma)
Age of mineralization/Relationship to metamorphism	Late-Triassic (206 Ma)/ Late- to post-metamorphim
Mineralization temperature/Depth	335-385 °C/10 to 12 km (brittle to ductile transition)
Hydrothermal alteration	Greenschist facies, graphite, carbonate, silicification, sulfidation
Mineralizing fluid	Low salinity, weakly alkaline to near-neutral pH, H_2O, CO_2, CH_4, N_2, H_2S, H_2, O_2, Au, K
Mineralizing fluid source	Potentially igneous/Metamorphic dehydration and devolatilization
Structure continuity	~20 km strike, up to 300 m thick
Principle metal suite	Au (Low base metals content)
Mineralization style	High grade quartz veins and low grade disseminated in the alteration envelope
Principle sulfide minerals	Pyrite; minor chalcopyrite and arsenopyrite
Gold texture and paragenesis	Encapsulated in sulfides; rare free-gold

REFERENCES

Agangi, A., Hofmann, A. and Wohlgemuth-Ueberwasser, C.C. (2013). Pyrite zoning as a record of mineralization in the Ventersdorp Contact Reef, Witwatersrand Basin, South Africa. *Economic Geology*, *108*(6), 1243-1272.

Barley, M.E. and Groves, D.I. (1990). Deciphering the tectonic evolution of Archaean greenstone belts: the importance of contrasting histories to the distribution of mineralization in the Yilgarn Craton, Western Australia. *Precambrian Research*, *46*(1-2), 3-20.

Berner, R.A. (1970). Sedimentary pyrite formation. *American Journal of Science*, *268*(1), 1-23.

Beyssac, O., Goffe, B., Chopin, C. and Rouzaud. (2002). Raman spectra of carbonaceous material in metasediments: a new geothermometer. *Journal of Metamorphic Geology*, *20*(9), 859-871.

Bodnar, R.J. (1993). Revised equation and table for determining the freezing point depression of H_2O-NaCl solutions. *Geochimica et Cosmochimica Acta*, 57(3), 683-684.

Bodnar, R.J. (2003). Introduction to aqueous fluid systems. In: Simon, I., Anderson, A. and Marshall, D. (Eds.), *Fluid Inclusions: Analysis and Interpretation*. Mineralogical Association of Canada, Short Course 32, 81-99.

Bodnar, R.J. (2007). Fluid inclusions in magmatic and hydrothermal ore deposits, with applicants to exploration. In: *Ores and Orogenesis 2007 short course manual, 25, September, 2007, Tucson, Arizona*.

Bodnar, R. J., Lecumberri-Sanchez, P., Moncada, D. and Steele-MacInnis, M. (2014). 13.5-Fluid inclusions in hydrothermal ore deposits. *Treatise on Geochemistry, Second Edition end*. Elsevier, Oxford, 119-142.

Bui, H.B., Ngo, X.T., Khuong, T.H., Golonka, J., Nguyen, T.D., Song, Y., Itaya, T. and Yagi, K. (2017). Episodes of brittle deformation within the Dien Bien Phu Fault zone, Vietnam: Evidence from K-Ar age dating of authigenic illite. *Tectonophysics, 695*, 53-63.

Bunopas, S. (1981). Paleogeographic history of western Thailand and adjacent parts of South-East Asia: A plate tectonics interpretation. *Geological Survey Special Publication, 5*, 810p.

Burke, E.A. (2001). Raman microspectrometry of fluid inclusions. *Lithos*, *55*(1-4), 139-158.

Burrows, D.R., and Spooner, E.T.C. (1985). Generation of an Archaean H_2O-CO_2 fluid enriched in Au, W & Mo by fractional crystallization in the Mink Lake intrusion, NW Ontario: *Geological Society of America Abstracts with Programs, 17*, p536.

Butler, I.B. and Rickard, D. (2000). Framboidal pyrite formation via the oxidation of iron (II) monosulfide by hydrogen sulphide. *Geochimica et Cosmochimica Acta*, *64*(15), 2665-2672.

Cannell, J. and Smith, S. (2008). High-grade supergene enriched and exotic copper deposits in the Sepon Mineral District, Lao PDR. In *Proceedings of PACRIM Congress*, 355-361.

Carter, A., Roques, D., Bristow, C. and Kinny, P. (2001). Understanding Mesozoic accretion in Southeast Asia: significance of Triassic thermotectonism (Indosinian orogeny) in Vietnam. *Geology*, *29*(3), 211-214.

Chang, Z., Large, R.R. and Maslennikov, V. (2008). Sulfur isotope in sediment-hosted orogenic gold deposits: Evidence for an early timing and a seawater sulfur source. *Geology*, 36, 971-974.

Charusiri, P., Daorek, V., Archibald, D., Hisada, K. and Ampaiwan, T. (2002). Geotectonic Evolution of Thailand; A new synthesis. *Journal of the Geological Society of Thailand, 1*, 1-20.

Clark, L. A. (1960). The Fe-As-S system: phase relations and applications. *Economic Geology, 55*(7), 1345-1381.

Colvine, A.C. (1989). An empirical model for the formation of Archean gold deposits: Products of final cratonization of the Superior province, Canada. *Economic Geology Monograph, 6*, 37-53

Cox, S. F., Wall, V.J., Etheridge, M.A. and Potter, T.F. (1991).. Deformational and metamorphic processes in the formation of mesothermal vein-hosted gold deposits: Examples from the Lachlan fold belt in central Victoria, Australia. *Ore Geology Reviews, 6*(5), 391-423.

Craw, D. (2002). Geochemistry of late metamorphic hydrothermal alteration and graphitization of host rock, Marcraes gold mine, Otago Schist, New Zealand. *Chemical Geology, 191*(4), 257-275.

Cromie, P.W. (2010). *Geological setting, geochemistry and genesis of the Sepon gold and copper deposits, Laos*. Unpublished PhD thesis, ARC Centre of Excellence in Ore Deposits (CODES), University of Tasmania, Hobart, Austalia, 395p.

Deditius, A.P., Reich, M., Kesler, S.E., Utsunomiya, S., Chryssoulis, S.L., Walshe, J. and Ewing, R.C. (2014). The coupled geochemistry of Au and As in pyrite from hydrothermal ore deposits. *Geochimica et Cosmochimica Acta*, *140*, pp.644-670.

Diamond, L.W. (1990). Fluid inclusion evidence for P-V-T-X evolution of hydrothermal solutions in late-Alpine gold-quartz veins at Brusson, Val d'Ayas, Northwest Italian Alps. *American Journal of Science*, *290*(8), 912-958.

Diamond, L.W. (2001). Review of the systematics of CO_2-H_2O fluid inclusions. *Lithos*, *55*(1-4), 69-99.

Diamond, L.W. and Tarantola, A. (2015). Interpretation of fluid inclusions in quartz deformed by weak ductile shearing: Reconstruction of differential stress magnitudes and pre-deformation fluid properties. *Earth and Planetary Science Letter*, 417, 107-119.

Fall, A. and Bodnar, R.J. (2018). How precisely can the temperature of a fluid event be constrained using fluid inclusions?. *Economic Geology*, *113*(8), 1817-1843.

Faure, M., Lepvrier, C., Van Nguyen, V., Van Vu, T., Lin, W. and Chen, Z. (2014). The South China block-Indochina collision: Where, when, and how?. *Journal of Asian Earth Sciences*, *79*, 260-274.

Faure, M., Nguyen, V.V., Hoai, L.T.T. and Lepvrier, C. (2018). Early Paleozoic or Early-Middle Triassic collision between the South China and Indochina blocks: The controversy resolved? Structural insights from the Kon Tum massif (central Vietnam). *Journal of Asian Earth Sciences*, *166*, 162-180.

Gardner, C.J., Graham, I.T., Belousova, E., Booth, G.W. and Greig, A. (2017). Evidence for Ordovician subduction-related magmatism in the Truong Son terrane, SE Laos: Implications for Gondwana evolution and porphyry Cu exploration potential in SE Asia. *Gondwana Research*, *44*, 139-156.

Goldfarb, R.J. and Groves, D.I. (2015). Orogenic gold: Common or evolving fluid and metal sources through time. *Lithos*, *233*, 2-26.

Goldfarb, R.J., Baker, T., Dube, B., Groves, D.I., Hart, C.J., Gosselin, P. (2005). Distribution, character and genesis of gold deposits in metamorphic terranes. In: Hedenquist, J., Thompson, J., Goldfarb, R., Richards, J. (Eds.), *Economic Geology One Hundredth Anniversary Volume*, 407-450.

Goldfarb, R. J., Groves, D. I. and Gardoll, S. (2001). Orogenic gold and geologic time: a global synthesis. *Ore Geology Reviews, 18*(1-2), 1-75.

Goldstein, H.R. and Renolds, T. (1994). *Systematics of fluid inclusions in diagenetic minerals*. *SEPM short course, 31*, 199p.

Groves, D.I. (1993). The crustal continuum model for late-Archaean lode-gold deposits of the Yilgarn Block, Western Australia. *Mineralium Deposita, 28*(6), 366-374.

Groves, D.I ., Goldfarb, R.J., Gebre-Mariam, M., Hagemann, S.G. and Robert, F. (1998). Orogenic gold deposits: A proposed classification in the context of their crustal distribution and relationship to other gold deposit types. Ore Geology Reviews, 13(1-5), 7-27.

Groves, D.I., Goldfarb, R. ., Robert, F., Hart, C.J.R. (2003). Gold deposits in metamorphic belts: overview of current understanding, outstanding problems, future research, and exploration significance. *Economic Geology*, *98*(1), 1-29.

Hagemann, S.G. and Lüders, V. (2003). P-T-X conditions of hydrothermal fluids and precipitation mechanism of stibnite-gold mineralization at the Wiluna lode-gold deposits, Western Australia: conventional and infrared microthermometric constraints. *Mineralium Deposita*, *38*(8), 936-952.

Hagemann, S.G., Groves, D.I., Ridley, J.R. and Vearncombe, J.R. (1992). The Archean lode gold deposits at Wiluna, Western Australia; high-level brittle-style mineralization in a strike-slip regime. *Economic Geology*, *87*(4), 1022-1053.

Haines, S. H. and van der Pluijm, B.A. (2008). Clay quantification and Ar-Ar dating of synthetic and natural gouge: application to the Miocene Sierra Mazatán detachment fault, Sonora, Mexico. *Journal of Structural Geology*, *30*, 525-538.

Hayashi, K.I. and Ohmoto, H. (1991). Solubility of gold in NaCl- and H_2S-bearing aqueous solutions at 250-350 ºC. *Geochimica et Cosmochimica Acta*, *55*(8), 2111-2126.

Holloway, J.R. (1984). Graphite-CH_4-H_2O-CO_2 equilibria at lowgrade metamorphic conditions. *Geology, 12*(8), 455-458.

Hronsky, J.M., Groves, D.I., Loucks, R.R. and Begg, G.C. (2012). A unified model for gold mineralisation in accretionary orogens and implications for regional-scale exploration targeting methods. *Mineralium Deposita*, *47*(4), 339-358.

Hutchison, C.S. (1989). *Geological evolution of South-east Asia*. Vol 13, 368p. Oxford: Clarendon Press.

Hutchison, C.S. (2014). Tectonic evolution of Southeast Asia. *Bulletin of the Geological Society of Malaysia*, *60*, 1-18.

Intasopa, S. (1993). *Petrology and geochronology of the volcanic rocks of the Central Thailand Volcanic Belt*. Unpubished PhD Thesis, University of New Brunswick, Fredericton, 242p.

Intasopa, S.B. and Dunn, T. (1994). Petrology and Sr-Nd isotopic systems of the basalts and rhyolites, Loei, Thailand. *Journal of Southeast Asian Earth Sciences, 9*, 167-180.

Itaya, T. (2020). K-Ar phengite geochronology of HP-UHP metamorphic rocks-An in-depth review. *Journal of Mineralogical and Petrological Sciences*, *115*, 44-58.

Itaya, T., Hyodo, H., Uruno, K. and Mikoshiba, M.U. (2005). Ultra-high excess argon in kyanites: implications for ultra-high pressure metamorphism in Northeast Japan. *Gondwana Research, 8*, 617-621.

Itaya, T., Nagao, K., Inoue, K., Honjou, Y., Okada, T. and Ogata, A. (1991). Argon isotopic analysis by newly developed mass spectrometric system for K-Ar dating. *Mineralogical Journal, 15*, 203-221.

Jehlicka, J. and Benny, C. (1992). Application of Raman microspectroscopy in the study of structural change in Precambrian kerogens during regional metamorphism. *Organic Geochemistry, 18*(2), 211-213.

Kamvong, T., Zaw, K., Meffre, S., Maas, R., Stein, H. and Lai, C.K. (2014). Adakites in the Truong Son and Loei fold belts, Thailand and Laos: Genesis and implications for geodynamics and metallogeny. *Gondwana Research, 26*(1), 165-184.

Keith, M., Smith, D.J., Jenkin, G.R., Holwell, D.A. and Dye, M.D. (2018). A review of Te and Se systematics in hydrothermal pyrite from precious metal deposits: Insights into ore-forming processes. *Ore Geology Reviews, 96*, 269-282.

Kelley, S. (2002a). Excess argon in K-Ar and Ar-Ar geochronology. *Chemical Geology, 188*, 1-22.

Kelley, S. (2002b). K-Ar and Ar-Ar dating. *Reviews in Mineralogy and Geochemistry, 47*, 785-818.

Kelley, S., Turner, G., Butterfield, A. and Shepherd, T.J. (1986). The source and significance of argon isotopes in fluid inclusions from areas of mineralization. *Earth and Planetary Science Letters, 79*, 303-318.

Kerrich, R., Goldfarb, R., Groves, D., Garwin, S. and Jia, Y. (2000). The characteristics, origins, and geodynamic settings of supergiant gold metallogenic provinces. *Science in China Series D: Earth Sciences*, *43*(1), 1-68.

Khositanont, S., Panjasawatwong, Y., Ounchanum, P., Thanasuthipitak, T., Khin Zaw. and Meffre, S. (2008). Petrochemistry and zircon age determination of Loei–Phetchabun volcanic rocks. In: Chutakositkanon, V., Sutthirat, C., Charoentitirat, T. (Eds.), *International Symposia on Geoscience Resources and Environments of Asian Terranes (GREAT 2008), 4th IGCP 516 and 5th APSEG*. Bangkok, 272-278.

Kirwin, D.J. and Royle, D.Z. (2019). Sediment-hosted gold deposits in Southeast Asia. *Resource Geology*, *69*, 125-147.

Kralik, M., Klima, K. and Riedmüller, G. (1987). Dating fault gouges. *Nature*, *327*, 315-317.

Kraus, I., Chernyshev, I.V., Šucha, V., Kovalenker, V.A., Lebedev, V.A. and Šamajová, E. (1999). Use of illite for K/Ar dating of hydrothermal precious and base metal mineralization in Central Slovak Neogene volcanic rocks. *Geologica Carpathica*, *50*, 353-364.

Kretschmar, U. and Scott, S.D. (1976). Phase relations involving arsenopyrite in the system Fe-As-S and their application. *Canadian Mineralogist*, *14*(3), 364-386.

Large, D.J., Christy, A.G. and Fallick, A.E. (1994). Poorly crystalline carbonaceous matter in high grade metasediments: implications for graphitisation and metamorphic fluid compositions. *Contribution to Mineralogy and Petrology*, *116*(1-2), 108-116.

Large, R.R., Maslennikov, V., Robert, F., Danyushevsky, L.V. and Chang, Z. (2007). Multistage sedimentary and metamorphic origin of pyrite and gold in the Sukhoi Log deposit, Lena gold province, Russia. *Economic Geology, 102*(7), 1232-1267.

Large, R.R., Bull, S.W. and Maslennikov, V.V. (2011). A carbonaceous sedimentary source-rock model for Carlin-type and orogenic gold deposits. *Economic Geology*, *106*(3), 331-358.

Large, R.R., Danyushevsky, L.V., Hollit, C., Maslennikov, V., Meffre, S., Gilbert, S., Bull, S., Scott, R., Emsbo, P., Thomas, H., Singh, B. and Foster, J. (2009). Gold and trace element zonation in pyrite using laser imaging technique: Implication for the timing of gold in orogenic and carlin-style sediment-hosted deposit. *Economic Geology, 104*(5), 635-668.

Lepvrier, C., Maluski, H., Van Tich, V., Leyreloup, A., Thi, P.T. and Van Vuong, N. (2004). The Early Triassic Indosinian orogeny in Vietnam (Truong Son Belt and Kontum Massif); implications for the geodynamic evolution of Indochina. *Tectonophysics*, *93*, 87-118.

Lepvrier, C., Van Vuong, N., Maluski, H., Thi, P.T. and Van Vu, T. (2008). Indosinian tectonics in Vietnam. *Comptes Rendus Geoscience*, *340*(2-3), 94-111.

Liu, J., Tran, M.D., Tang, Y., Nguyen, Q.L., Tran, T.H., Wu, W., Chen, J., Zhang, Z. and Zhao, Z. (2012). Permo-Triassic granitoids in the northern part of the Truong Son belt, NW Vietnam: geochronology, geochemistry and tectonic implications. *Gondwana Research, 22*(2), 628-644.

Lyons, J. and Snellenburg, J. (1970). Dating faults. *Geological Society of America Bulletin*, *82,* 1749-1752.

MacNamara, J. and Thode, H.G. (1950). Comparison of the isotopic constitution of terrestrial and meteoric sulphur. *The Physical Review*, 78, 307-308.

Manaka, T. (2014). *A study of mineralogical, geochemical and geochronological characteristics and ore genesis in Phuoc Son Gold Deposit Area, Central Vietnam.* Unpublished PhD thesis, ARC Centre of Excellence in Ore Deposits (CODES), University of Tasmania, Hobart, Austalia, 285p.

Manaka, T., Dinh, S.Q., Zaw, K., Meffre, S., Halpin, J., Hai, T.T., Hai, L.V. and Hung, N.B. (2010). Geology and mineralization of the Phuoc Son gold deposits, central Vietnam. Giant Ore Deposits Down-Under. In *13th Quadrennial IAGOD Symposium Proceedings*, Adelaide, 141-142.

Metcalfe, I. (1996). Gondwanaland dispersion, Asian accretion and evolution of eastern Tethys. *Australian Journal of Earth Sciences, 43*(6), 605-623.

Metcalfe, I. (1999). Gondwana dispersion and Asian accretion: an overview. *Gondwana dispersion and Asian accretion*, 9-28.

Metcalfe, I. (2011). Palaeozoic–Mesozoic history of SE Asia. *Geological Society, London, Special Publications, 355*(1), 7-35.

Minezaki, T., Hisada, K.I., Hara, H. and Kamata, Y. (2019). Tectono-stratigraphy of Late Carboniferous to Triassic successions of the Khorat Plateau Basin, Indochina Block, northeastern Thailand: Initiation of the Indosinian Orogeny by collision of the Indochina and South China blocks. *Journal of Asian Earth Sciences, 170*, 208-224.

Moore, D.M. and Reynolds Jr, R.C. (1997). X-ray Diffraction and the Identification and Analysis of Clay Minerals. Oxford University Press, New York.

Muntean, J.L., Cline, J.S., Simon, A.C. and Longo, A.A. (2011). Magmatic-hydrothermal origin of Nevada's Carlin-type gold deposits. *Nature Geoscience, 4*, 122-127.

Naden, J. and Shepherd, T.J. (1989). Role of methane and carbon dioxide in gold deposition. *Nature, 342*(6251), 793-795.

Nagao, K., Nishido, H., Itaya, T. and Ogata, K. (1984). K-Ar age determination method. *Bulletin of Hiruzen Research Institute, 9,* 19-38.

Nagy, E.A., Maluski, H., Lepvrier, C., Schrer, U., Phan, T.T., Leyreloup, A., Vu,V.T. (2001). Geodynamic significance of the Kon Tum massif in Central Vietnam: composite 40Ar/39Ar and U/Pb ages from Paleozoic to Triassic. The Journal of Geology, 109(6), 755-770.

Nakano, N., Osanai, Y., Owada, M., Nam, T.N., Toyoshima, T., Binh, P., Tsunogae, T. and Kagami, H. (2007). Geologic and metamorphic evolution of the basement complexes in the Kontum Massif, central Vietnam. *Gondwana Research. 12*, 438-453.

Nemanich, R. J. and Solin, S. A. (1979). First- and second-order Raman scattering from finite-size crystals of graphite. *Physical Review B, 20*(2), 392-401.

Nguyen Van Trang. (1986). *Geological Map of Vietnam 1:200000 scale, Thua Thien Hue-Quang Ngai sheets: E-48-XXXV (Huong Hoa), E-48-XXXVI (Thua Thien Hue), D-48-XII (Dac To), E-49-XXXI (Da Nang), D-48-VI (Ba Na), D-49-I (Hoi An), D-48-VII (Quang Ngai)*. Geological Survey of Vietnam, Hanoi.

Ohmoto, H. and Rye, R.O. (1979). Isotopes of sulfur and carbon. In: Barnes, H.L (Ed.) *Geochemistry of hydrothermal ore deposits*, 509-567.

Osanai, Y., Nakano, N., Owada, M., Miyamoto, T., Nam, T.N., Minh, N.T., Nam, N.V. and Tri, T.V. (2008). Collision zone metamorphism in Vietnam and adjacent South-eastern Asia: proposition for trans-Vietnam orogenic belt. *Journal of Mineralogical and Petrological Sciences, 103*, 226-241.

Owada, M., Osanai, Y., Nakano, N., Adachi, T., Kitano, I., Van Tri, T. and Kagami, H. (2016). Late Permian plume-related magmatism and tectonothermal events in the Kontum Massif, central Vietnam. *Journal of Mineralogical and Petrological Sciences, 111*, 181-195.

Perring, C.S., Groves, D.I. and Ho, S.E. (1987). Constraints on the source of auriferous fluids for Archaean gold deposits. In: Ho, S.E. and Groves, D.I. (Eds). *Advances in understanding Precambrian gold deposits*. Geology Department and University Extension, University of Western Australia, Publication 11, 287-306.

Phillips, G.N. and Evans, K.A. (2004). Role of CO_2 in the formation of gold deposits. *Nature, 429*(6994), 860-863.

Phillips, G.N. and Groves, D.I. (1984). Fluid access and fluid-wall rock interaction in the genesis of the Archaean gold-quartz vein deposit at Hunt mine, Kambalda, Western Australia. *In Gold'82: the geology, geochemistry and genesis of gold deposits. Symposium*, 389-416.

Phillips, G. N. and Powell, R. (2010). Formation of gold deposits: a metamorphic devolatilization model. *Journal of Metamorphic Geology, 28*(6), 689-718.

Pitcairn, I.K., Teagle, D.A., Craw, D., Olivo, G.R., Kerrich, R. and Brewer, T.S. (2006). Sources of metals and fluids in orogenic gold deposits: insights from the Otago and Alpine Schists, New Zealand. *Economic Geology*, *101*(8), 1525-1546.

Poulsen, K.H., Ames, D.E., Lau, S., and Brisbin, W.C. (1986). *Preliminary report on the structural setting of gold in the Rice Lake area, Uchi subprovince, southeastern Manitoba:* Geological Survey of Canada Paper 86-1B, 213–221.

Qian, X., Feng, Q.L., Yang, W.Q., Wang, Y.J., Chonglakmani, C., Monjai, D. (2015). Arc-like volcanic rocks in NW Laos: geochronological and geochemical constraints and their tectonic implications. *Journal of Asian Earth Sciences, 98*, 342–357.

Quynh, N.N., Murfitt, R.H., Sirinawin, T. and Shywoluo, W. (2004). The Bong Mieu gold project, Phuoc Son-Tam Ky Suture, central Vietnam. *Proceedings of PacRim Congress 2004*, Adelaide, 347-358.

Rama, S.N.I, Hart, S.R. and Roedder, E. (1965). Excess radiogenic argon in fluid inclusions. *Journal of Geophysical Research, 70*, 509-511.

Ridley, J.R. (1993). The relationship between mean rock stress and fluid flow in the crust: with reference to vein and lode-style deposits. *Ore Geology Reviews, 8*(1-2), 23-37.

Ridley, J.R. and Diamond, L.W. (2000). Fluid chemistry of orogenic lode gold deposits and implications for genetic models: *Review in Economic Geology, 13*, 141-162.

Roedder, E. (1984). Fluid inclusions. *Review in Mineralogy*, *12*, 11-46.

Roedder, E and Bodnar, R.J. (1997). Fluid inclusion studies of hydrothermal ore deposits (Chapter 13). In: Barnes, H.L., (Ed.), *Geochemistry of hydrothermal ore deposits*. John Wiley and Sons, INC, 657-697.

Rollinson, H.R. (1993). *Using Geochemical Data: Evaluation, Presentation, Interpretation*: New York, Longman Group, p352.

Salam, A., Zaw, K., Meffre, S., McPhie, J. and Lai, C.K. (2014). Geochemistry and geochronology of the Chatree epithermal gold-silver deposit: Implications for the tectonic setting of the Loei Fold Belt, central Thailand. *Gondwana Research, 26*(1), 198-217.

Sanematsu, K., Murakami, H., Duangsurigna, S., Vilayhack, S., Duncan, R. and Watanabe, Y. (2011). 40Ar/39Ar ages of granitoids from the Truong Son fold belt

and Kontum massif in Laos. *Journal of Mineralogical and Petrological Sciences, 106*, 13-25.

Sanematsu, K., Murakami, H., Watanabe, Y., Duangsurigna, S. and Siphandone, V. (2009). Enrichment of rare earth elements (REE) in granitic rocks and their weathered crusts in central and southern Laos. *Bulletin of the Geological Survey of Japan*, *60*(11-12), 527-558.

Sangster, D.F. (1979). Sulphur and lead isotopes in stratabound deposits. In Wolf, K.H., (Ed.) *Handbook of strata-bound and stratiform ore deposits*, Elservier, (Amsterdam), 261p.

Seward, T.M. (1973). Thio complexes of gold and the transport of gold in hydrothermal ore solutions. *Geochimica et Cosmochimica Acta*, *37*(3), 379-399.

Sharp, Z.D., Essene, E. J. and Kelly, W.C. (1985). A re-examination of the arsenopyrite geothermometer: Pressure considerations and applications to natural assemblages. *Canadian Mineralogist*, *23*(4), 517-534.

Shepherd, T.J., Rankin, A.H. and Alderton, D.H.M. (1985). *A practical guide to fluid inclusion studies*. Blackie

Shi, M.F., Lin, F.C., Fan, W.Y., Deng, Q., Cong, F., Tran, M.D., Zhu, H.P. and Wang, H. (2015). Zircon U-Pb ages and geochemistry of granitoids in the Truong Son terrane, Vietnam: Tectonic and metallogenic implications. *Journal of Asian Earth Sciences*, *101*, 101-120.

Smith, P.F.L. and Stokes, R.B. (1997). Geology and petroleum potential of the Khorat plateau basin in the Vientiane area of Lao P.D.R. *Journal of Petroleum Geology*, *20*, 27-50.

Smith, S., Olberg, D. and Manini, T. (2005). The Sepon gold deposits, Laos: exploration, geology, and comparison to Carlin-type gold deposits in the Great Basin. In *Geological Society of Nevada Symposium, Reno, Nevada*, 899-915.

Sterner, S.M. and Bodnar, R.J. (1984). Synthetic fluid inclusions in natural quartz I. Compositional types synthesized and applications to experimental geochemistry. *Geochimica et Cosmochimica Acta*, *48*(12), 2659-2668.

Takagi, H., Iwamura, A., Awaji, D., Itaya, T. and Okada, T. (2005). Dating of fault gouges from the major active faults in southwest Japan: Constraints from integrated K-Ar and XRD analyses. In: Sorkhabt, R. and Tsuji, K (Ed.) *Faults, Fluid Flow, and Petroleum Traps, American Association of Petroleum Geologists Memoir*, *85*, 287-301.

Togashi, Y. (1979). Polytypes and expandability of sericite from the Itaya kaolin clay deposit, Northeast Japan. *The Journal of the Japanese Association of Mineralogists, Petrologists and Economic Geologists*, *74*, 100-113.

Tomkins, A.G. (2013). A biogeochemical influence on the secular distribution of orogenic gold. *Economic Geology 108*(2), 193-197.

Tran, H.T., Zaw, K., Halpin, J.A., Manaka, T., Meffre, S., Lai, C.K., Lee, Y., Van Le, H. and Dinh, S. (2014). The Tam Ky-Phuoc Son shear zone in Central Vietnam: tectonic and metallogenic implications. *Gondwana Research*, *26*, 144-164.

Tuinistra, F. and Koenig, J. L. (1970). Raman spectrum of graphite. *Journal of Chemical Physics*, *53*(3), 1126-1130.

United Nations (1990). *Social Commission for Asia and the Pacific (ESCAP), Atlas of Mineral Resources of the ESCAP Region*. UN, New York. Report Number: 6 (Vietnam).

van der Pluijm, B., Hall, C., Vrolijk, P., Pevear, D., and Covey, M. (2001). The dating of shallow faults in the Earth's crust. *Nature*, *412*, 172-175.

Vilayhack, S., Duangsurigna, S., Voravong, A., Vilaysan, P., Khounchanthida, T., Phommakaysone, K., Goto, M., Negishi, Y., Tsuda, K., Watanabe, Y. and Shibata, Y. (2008). *1:200,000 Geological map of B. Dakyoy with report on geology of B. Dakyoy district*, 44p, Japan International Cooperation Agency and Department of Geology, Ministry of Energy and Mines, Lao P. D. R, Vientiane.

Vu Van Tich., Maluski, H. and Nguyen Van Vuong (2007). Ar-Ar age of metamorphic and mylonitic rocks in northern part of the Kon Tum Massif: evidence for the Indosinian movement along shear zones between Kon Tum Massif and Truong Son Belt. *VNU Journal of Science, Earth Sciences*, *23*, 253-264.

Wada, H., Tomita, T., Matsuura, K., Tuchi, K., Ito, M. and Morikiyo, T. (1994). Graphitization of carbonaceous matter during metamorphism with references to carbonate and pelitic rocks of contact and regional metamorphisms, Japan. *Contribution to Mineralogy and Petrology*, *118*(3), 217-228.

Wang, S., Mo, Y., Wang, C. and Ye, P. (2016). Paleotethyan evolution of the Indochina Block as deduced from granites in northern Laos. *Gondwana Research*, *38*, 183-196.

Wang, Y., Wang, Y., Qian, X., Zhang, Y., Gan, C., Senebouttalath, V. and Wang, Y. (2020). Early Paleozoic subduction in the Indochina interior: Revealed by Ordo-Silurian mafic-intermediate igneous rocks in South Laos. *Lithos*, 105488.

Wasserman, M.D., Rye, R.O., Bethke, P.M. and Arribas, A.Jr. (1992). Methods for separation and total stable isotope analysis of alunite: *U.S. Geological Survey Open-File Report*, *92-9*, 20p.

Watanabe, Y. and Hedenquist, J.W. (2001). Mineralogic and stable isotope zonation at the surface over the El Salvador porphyry copper deposit, Chile. *Economic Geology*, *96*(8), 1775-1797.

Wopenka, B. and Pasteris, J.D. (1993). Structural characterization of kerogens to granulite-facies graphite: Applicability of Raman microprobe spectroscopy. *American Mineralogist*, *78*(5-6), 533-557.

Yagi, K., Okada, T., Honjou, Y. and Itaya, T. (2015). Argon analyses by isotopic dilution method using argon 38 spike with HIRU: Reproducibility and reliability in 25 years K-Ar dating. *Bulletin of the Research Institute of Technology*, *33*, 43-54.

Zaw, K., Meffre, S. and higher degree students. (2007). *Metallogenic relations and deposit-scale studies*, Final Report, Geochronology, metallogenesis and deposit styles of Loei Fold Belt in Thailand and Laos PDR, ARC Linkage Project.

Zaw, K., Meffre, S. and the team. (2010). Final report on "Ore Deposits of SE Asia" Project.

Zaw, K., Meffre, S., Lai, C.K., Burrett, C., Santosh, M., Graham, I., Manaka, T., Salam, A., Kamvong, T. and Cromie, P. (2014). Tectonics and metallogeny of mainland Southeast Asia-A review and contribution. *Gondwana Research*, *26*, 5-30.

Appendix I

Results of microthermometric data

Sample No	Inclusion No	Inclusion type	Inclusion size (μm)	Melting Temp (ice; ºC)	Homogenization temperature (°C)	Salinity (Wt% NaCl. Eq)
20190424-3	1	L>V	15	-6.6	216.36	9.98
	2	L>V	10	-0.4	208.97	0.71
	3	L>V	10	-0.5	205.19	0.88
	4	L>V	5	-2.7	213.90	4.49
	5	L>V	10	–	201.60	–
	6	L>V	5	–	199.33	–
	7	L>V	5	-1.8	241.91	3.06
	8	L>V	5	-1.8	240.96	3.06
	9	L>V	5	-1.8	242.86	3.06
	10	L>V	5	-1.8	241.91	3.06
	11	L>V	5	-3.3	239.06	5.41
	12	L>V	5	-3.3	237.15	5.41
	13	L>V	10	-1.8	244.77	3.06
	14	L>V	10	-4.0	241.91	6.45
	15	L>V	10	-3.8	242.86	6.16
	16	L>V	5	-2.9	244.77	4.8
	17	L>V	5	-3.5	240.96	5.71
	18	L>V	5	-3.3	243.81	5.41
	19	L>V	10	-4.1	245.72	6.59
	20	L>V	5	-3.3	241.91	5.41
	21	L>V	5	-3.4	241.91	5.56
	22	L>V	5	-3.1	242.86	5.11
	23	L>V	5	-1.9	241.91	3.23
	24	L>V	15	-2.4	243.81	4.03
	25	L>V	5	-3.9	243.81	6.3
	26	L>V	5	-4.8	244.77	7.59
	27	L>V	5	-4.5	241.91	7.17
	28	L>V	5	-3.6	245.72	5.86
	29	L>V	5	-3.4	205.85	5.56
	30	L>V	5	-3.4	243.81	5.56
	31	L>V	10	-0.9	–	1.57
	32	L>V	10	-0.7	235.16	1.23
	33	L>V	5	–	290.00	–
	34	L>V	5	–	284.91	–
	35	L>V	10	-2.5	201.22	4.18
	36	L>V	5	-2.8	194.42	4.65
	37	L>V	10	-2.9	191.96	4.8
	38	L>V	5	-2.9	191.77	4.8
	39	L>V	5	-2.8	–	4.65

Sample No	Inclusion No	Inclusion type	Inclusion size (μm)	Melting Temp (ice; ºC)	Homogenization temperature (°C)	Salinity (Wt% NaCl. Eq)
VADH018-134.6	1	L>V	5	-0.5	273.03	0.88
	2	L>V	5	-1.2	213.04	2.07
	3	L>V	5	-2.5	–	4.18
	4	L>V	5	-3.2	272.55	5.26
VADH017-98.00	1	L>V	10		285.10	
	2	L>V	15		224.33	
	3	L>V	10		234.87	
	4	L>V	10		197.72	
	5	L>V	8		183.38	
	6	L>V	8		203.20	
	7	L>V	8		300.76	
	8	L>V	10		322.44	
	9	L>V	5		325.34	
	10	L>V	5		277.91	
	11	L>V	10		254.78	
	12	L>V	5		253.35	

Appendix II

Measurement condition for fluid inclusion study

1. Sample preparation

Quartz-bearing sulfide samples from mineralized quartz-sulfide veins were selected and prepared fluid inclusion chips and made double-polished sections (150 to 300 μm thick).

2. Microthermometric measurement condition

Double polished sections samples were applied to microthermometry using a Linkam 10035 freezing-heating stage attached to a Nikon polarizing microscope, to determine the homogenization temperature and salinity of fluid inclusions at the Vangtat deposit. The general method and procedure for heating and freezing experiments are reported elsewhere (e.g. Roedder, 1984). The measurement was calibrated using the melting temperatures of the following components: CO_2 liquid (-56.6°C), n-dodecane (-9.6°C), n-tridecane (-5.5°C), pure water (0°C), n-tetradecane (+5.5°C), benzanilid (+163°C), sodium nitrate (+308°C), potassium dichromate (+398°C), and cupric chloride (+498°C). NaCl equivalent salinities of fluid inclusions were calculated using the equation of Bodnar (1993). The experiment was conducted at Akita University.

3. Laser Raman Spectroscopy

The Laser Raman Spectroscopy study was attempted to estimate the gas composition of fluid inclusions such as CO, CO_2, CH_4, H_2, H_2S, N_2, NH_3, and SO_2 using a Renishaw inVia Reflex Raman microscope with the 532 nm laser line Raman scattered light was

used as the exciting source, and a single 30-second accumulation. The focused laser spot on the samples was ~1 μm in diameter. Wavenumbers are accurate to ±1 cm^{-1} as determined by plasma and neon emission lines. For the analysis of CO, CO_2, CH_4, O_2, H_2S, and N_2 gas composition, spectra were recorded from 1000 to 3800 Raman shift cm^{-1} using a single 20 seconds integration time per spectrum. The operations were performed at Akita University.

Appendix III

Conventional technique for sulfur isotope analysis

1. Sample preparation

Fifteen pyrite samples from the Vangtat deposit were collected and analyzed. Coarse-grained pyrite-bearing samples from a quartz-sulfide vein and graphite-carbonate alteration envelope were separated by a portable driller. While the pyrite-bearing altered host pelitic schist samples, containing finer-grained and randomly distribute, then they were crushed and separated under binocular microscopic. These separated pyrite samples were powdered, obtaining >20 mg, and subjected to chemical treatment. The chemical treatment for the powdered sample is as follows:

1. The powdered pyrites were mixed with the chemical solution such as 20 ml acid nitric (HNO_3) and about 2 ml liquid bromine (Br_2) at 90 ºC and under a ventilator system for dissolving the pyrite samples and exchange the sulfide into sulfate.

2. The iron sulfate bearing acidified solution samples were diluted with 10 ml HCl 1:1 (50% dilution) and 90 ml distilled was also added. Then the solution was subjected to filtration for removing the undissolved materials (e.g. carbonic materials).

3. After filtration, the solution was applied for ion exchange using the Rasin column for avoiding coprecipitation with other cations.

4. 10 ml of 10% $BaCl_2 \cdot H_2O$ solution was added to the eluent to precipitated $BaSO_4$. Then using 0.25 μm filter paper to filtering and collecting $BaSO_4$. Then pure $BaSO_4$ Samples were subjected for sulfur isotope analysis, using the conventional technique.

2. Analytical condition

The $BaSO_4$ obtained from pyrites was packed with V_2O_5 in tin foil. The packed samples were load into the automatic sampler attached to the Thermo Fisher 2000 Elemental Analyzer, where the samples were combust in a quartz tube at 1,020 ºC. SO_2 gas was separated by gas chromatography, and isotopic ratios were measured using a Thermo Fisher Scientific Delta V Advantage isotope ratio monitoring mass spectrometer at Akita University. Standards used in the analysis included IAEA NBS-127 ($\delta^{34}S_{CDT}$=20.30‰), IAEA SO-6 (-34.10‰), and IAEA SO-5 (0.50‰). The sulfur isotope ratio is presented as $\delta^{34}S_{CDT}$ relatively to the 32S/34S value of Canon Diablo Troilite with an analytical uncertainty of ±0.2‰.